Micromachined Isolators for Shock and Vibration Reliability of MEMS Sensors: Fabrication, Damping, and Integration

by

Brent Bottenfield

A dissertation submitted to the Graduate Faculty of
Auburn University
in partial fulfillment of the
requirements for the Degree of
Doctor of Philosophy

Auburn, Alabama
December 12, 2020

Keywords: MEMS, Vibration Isolation, Sensor Reliability

Approved by

Mark Adams, Chair, Associate Professor of Electrical and Computer Engineering
Robert Dean, Professor of Electrical and Computer Engineering
Stuart Wentworth, Associate Professor of Electrical and Computer Engineering
Masoud Mahjouri-Samani, Assistant Professor of Electrical and Computer Engineering
George Flowers, Professor of Mechanical Engineering and Dean of the Graduate School

Abstract

This dissertation details the design, FEA simulation, fabrication, and testing of three variations of micromachined vibration isolators (MVIs). The vibration isolators serve as low pass filters to attenuate high frequency mechanical excitation in order to improve both MEMS sensor fidelity and lifespan. Isolators are designed for integration of a small (∼3mm x ∼3mm) MEMS sensor package and boast a sub-1 cm^2 footprint. For all isolator variations, the fundamental geometry consists of an outer frame to be fixed to the substrate of interest, a central platform to accommodate the isolated sensor, and springs for attachment of the frame and platform. Devices are fabricated via a double-sided lithography process using < 100> silicon-on-insulator (SOI) wafers. Laser Doppler vibrometry is performed to investigate the frequency response of each isolator variation across a 6.2 kHz bandwidth. Alternative methods of MVI fabrication including fused deposition molding (FDM), stereolithography (SLA), and two-photon polymerization (TPP) are discussed.

Additionally, this dissertation introduces the use of nickel (Ni) and copper (Cu) microfibrous meshes (MFMs) and Sorbothane® and polydimethysiloxane (PDMS) viscoelastic polymers to damp the dynamic response of MVIs for shock and vibration reliability in mechanically harsh environments. The MFMs are attached to the microisolators post-fabrication via solder attachment. We then investigate the transmissibility of the undamped and damped vibration microisolators using laser Doppler vibrometry. The peak transmissibility of the microisolator is significantly reduced for all four cases of polymer or MFM damping. Experimental results are compared to the FEA simulated transmissibility and to the analytically calculated transmissibility.

Lastly, MVI performance is validated by the integration of a wide bandwidth piezoelectric acclerometer. The accelerometer output for the isolated and unisolated cases are

compared. The experimental results confirm successful isolation of the accelerometer from high frequency excitation.

Acknowledgments

It would be nearly impossible to properly acknowledge all of the people who have been a positive influence on me over the course of my undergraduate and graduate career at Auburn. To those people who have shared their wisdom and guidance with me during my academic career but are not specifically mentioned below, I offer a sincere "Thank You".

First, I would like to thank all of the members of my PhD committee. I would like to express my deep appreciation for the time and attention given to the work presented in this dissertation. It is an honor to have each of you on my committee.

Next, I would like to thank everyone at the AMNSTC. In particular, thanks to William Baugh, Drew Sellers, and Dr. Michael Hamilton. Your diligent work in equipping and maintaining the microfabrication labs at Auburn, as well as the advice given regarding various fabrication techniques and processes, made the microfabrication discussed in this dissertation possible.

I'd also like to thank the folks at EngeniusMicro in Huntsville, Alabama who sponsored this project. Particularly, thanks to Dr. Mike Kranz and Dr. Brian English for your support and guidance of this project.

I would also like to offer my gratitude to all of my friends who supported me throughout my graduate career. In particular, I'd like to thank George Hughes and Vaibhav Gupta for the countless times you offered your assistance and advice in matters of microfabrication. I'd also like to offer a special thank you to Artie Bond who worked with me on much of the work presented in the dissertation. I could not have completed most of the work in this dissertation without your assistance.

Lastly, I'd like to thank Dr. Mark Adams for taking me on as a graduate student and for guiding me throughout my graduate career. I am forever grateful for the wisdom and expertise you have shared with me during my time at Auburn. War Eagle!

This dissertation is dedicated to my father, Tim, and my mother, Gigi. Thanks for all your love and support.

Table of Contents

List of Figures

List of Tables

Chapter 1

Introduction

Since the introduction of the resonant-gate silicon transistor by Nathanson and Wickstrom in 1965, the diverse set of engineering devices utilizing microscale mechanical sensing and/or actuation, often fabricated using similar methods as integrated circuits (ICs), has come to be known as microelectromechanical systems (MEMS) [1], [2]. The excellent mechanical properties of single crystal silicon and other materials used in IC fabrication allowed for the rapid development and implementation of MEMS sensors and actuators [3]. The prevalence of MEMS in current daily life is vast with applications ranging from but not limited to motion, pressure, and gas sensors in automobiles, microphone transducers in smartphones and laptops, resonant mechanical filters for RF communications, disposable sensors in medicine, and high-throughput microsystems for drug screening in biotechnology [4], [5]. This widespread success of MEMS technology has generated significant interest in the integration of MEMS sensors into harsh environments.

Integration of MEMS sensors and actuators into harsh mechanical environments requires careful consideration in order to mitigate both structural damage and inaccurate sensing or actuating of the integrated sensor. This dissertation details the use of vibration isolation via a micromachined isolator to allow MEMS sensor integration into mechanically harsh environments. Additionally, this dissertation discusses novel methods of damping the transmissibility of the fabricated isolator. Chapter Two provides a literature review of both reliability concerns in harsh environments for mechanical sensors (Section 2.1) and a summary of previously designed and fabricated micromachined isolation systems (Section 2.2). Chapter Three details the theory of vibration isolation for lightly damped (Section 3.1) and heavily damped (Section 3.2) vibration isolators. The vibration isolation damping theory

for Kelvin-Voigt solid and Maxwell fluid damped isolators is detailed. Chapter Four details the design (Section 4.1), fabrication (Section 4.2), and dynamic performance testing (Section 4.3) of three micromachined isolator variations using a silicon-on-insulator wafer as a fabrication substrate. Additionally, Section 4.4 discusses a few alternative technologies that may be applied to the fabrication of micromachined vibration isolators using additive manufacturing. Chapter Five introduces the use of four different damping materials (two polymers and two microfibrous meshes) as a means of reducing the peak dynamic response of a fabricated isolator. The simulated and experimental performance of each damping material is compared. Section 5.5 investigates the use of alternate damper geometries to tune micromachined vibration isolator frequency response. Lastly, Chapter Six presents the integration of a wide bandwidth piezoelectric accelerometer to validate the isolation performance of the fabricated isolators.

Chapter 2

Motivation and Background

2.1 Mechanical Sensor Reliability Concerns in Harsh Environments: A Motivation

The success of MEMS devices in sensing and actuating applications has lead to interest in their introduction into mechanically harsh environments. Examples of mechanically harsh environments include aircraft [6], spacecraft [7, 8, 9], industrial machinery [10, 11, 12], and ballistics [13, 14]. These environments possess mechanical excitation well into the kHz regime and transient shock accelerations as high as thousands of g's. In the case of ballistics, bandwidths can exceed 20 kHz with average accelerations approaching 20,000 g's and transient accelerations in the hundreds of thousands of g's [13, 14, 15].

The wide bandwidths and high sensitivities exhibited by many MEMS devices, such as accelerometers, gyroscopes, and micromirrors, along with their decreasing cost per sensing axis enabled by wafer-scale batch fabrication make them natural candidates for sensing and actuation applications in harsh environments [16, 17]. However, the wide-bandwidth and high acceleration excitations present in harsh environments can lead to a number of failure mechanisms in commercial grade MEMS devices.

MEMS device failure mechanisms can be categorized as either *destructive* or *operational* [18]. Destructive device failure results from damaged sensing or actuating structures. Operational device failure results from inaccurate sensing of desired measurands due to changes in device sensitivity.

Destructive device failure mechanisms in MEMS are numerous and have been studied extensively. The destructive failure mechanisms due to high acceleration shock impulses include fracture, delamination, and stiction [19]. Mechanical fracture is the separation of

Table 2.1: Specific Examples of Harsh Environments

Environment	**Specific Example**	**Peak Bandwidth (kHz)**	**Peak Accel. (G's)**	**Reference**
Aircraft	PCBs on airplane	2	A few	[6]
Spacecraft	Mars Microprobe	10	100,000	[9]
Industrial Machinery	Combustion Ignition Engine Block	16	100	[10]
Ballistics	Rockets, Artillery	20	>100,000	[13, 14]

a single structure into multiple structures due to the application of stress. Fracture failure results from stresses exceeding the yield strength of the accelerated MEMS structure. Fracture failure has been widely studied for a number of MEMS devices including accelerometers [20, 21] and microengines [22]. Srikar and Senturia suggest that for large duration shock impulses ($> 50\mu s$) many MEMS structures and their corresponding substrates act as rigid bodies which render the MEMS structures immune to shock-induced stress waves [19].

Delamination refers to the debonding and reduction in adhesion between two or more material layers. This is one of the most common failure mechanisms in MEMS and microelectronic devices [23]. In [22] Tanner reports that delamination of device packaging under high g shock loads is responsible for more device failures than device fracture. Delamination can often occur via the complete detachment of the MEMS device from its packaging substrate which can cause secondary failure mechanisms such as fracture of wire bonds. Meng *et al* report packaging failures account for about 75% of total failures in free-fall board-level drop tests. In contrast, device failures only account for 25% of failures [24].

Stiction can also occur in MEMS devices under considerable shock loads. Due to the high surface area to volume ratios of MEMS structures, surface forces are considerable [25]. If structures are displaced beyond their intended range and make contact with adjacent surfaces, these surface forces can result in permanent adhesion. The physical mechanisms resulting in stiction are broad. They include Van der Waal's force, capillary force, chemical

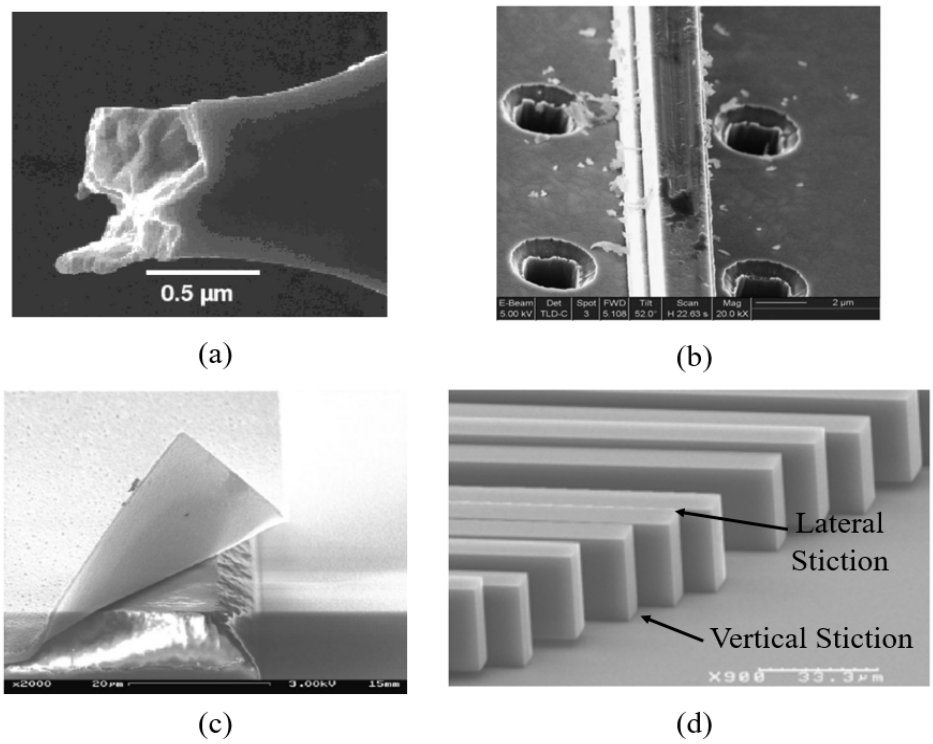

Figure 2.1: Examples of destructive failure mechanisms in MEMS. (a) Fracture of a cantilever beam [28]. (b) Debris caused by vibration-induced wear between two surfaces [29].(c) Delamination of an Al layer on polyimide substrate [30]. (d) Examples of lateral and vertical stiction in an array of cantilever beams. Vertical stiction is the adhesion of the beams to the substrate and the lateral sticition is the adhesion of the beams to one another [31]

bonding, electrostatic charging, and residual stress [26]. The probability of device failure due to stiction in micromachined accelerometers has been experimentally demonstrated to be proportional to the magnitude of the shock acceleration [27].

Vibration-induced failure modes in MEMS sensors include wear and fatigue. Wear is the removal of material from a surface as a result of mechanical action [32]. Abrasive wear occurs when a hard surface contacts a softer surface during harmonic excitation and gradually removes material from the softer surface. Additional types of wear include corrosive wear, in which the removal of material is the result of a chemical reaction, and surface fatigue wear, which is common in rolling interfaces where cracks can propagate parallel to a surface under cyclic loading [25]. Previous work by Tanner *et al* demonstrate widespread failure of micromechanical components due to wear and mechanical resonance when subjected to stress

frequencies from 860 to 3000 Hz [33]. Polysilicon layers have been shown to be particularly susceptible to wear compared to harder MEMS materials such as diamond-like carbon, single crystal silicon, silicon nitride, and silicon dioxide [34]. In addition to the loss of material in critical structures, the debris generated from wear is problematic. Debris can wedge into cavities or channels and impair appropriate structure displacement for sensing or actuation.

Fatigue refers to the progressive, localized structural damage that occurs when cyclic loading does not exceed a structure's yield strength. Fatigue begins with a small fracture occurring at a point of high stress and the fracture slowly propagates throughout the material [25]. Cyclic fatigue is the most common failure mechanism in structural materials [35]. Fatigue of MEMS devices under prolonged harmonic excitation is well studied. As with wear, polysilicon is particularly susceptible to fatigue. Bagdahn and Sharpe report significant reduction in tensile strength of polysilicon actuators due to cyclic fatigue where tensile strength loss is proportional to number of cycles and independent of excitation frequency across at 50 to 6000 Hz bandwidth [36]. Additionally, fatigue has been demonstrated to reduce the resonant frequencies of polysilicon and single crystal silicon resonators after cyclic loading [37, 38]. Single crystal silicon resonators in ambient air and under cyclic loading can fail at cyclic loads just 50% the single cycle failure load [38]. Recent work by Alter *et al* demonstrate failure of thick (≥ 20 μm) epitaxially grown polysilicon beams due to fatigue in vacuum-packaged environments. The polysilicon samples typically fail at stresses above 1.5 GPa at temperatures from 25 °C to 250 °C independent of contributions from natively grown oxide or environmental conditions [39].

The most common operational failure mode of MEMS sensors in harsh environments is increased sensitivity due to ambient acceleration. Acceleration sensitivity refers to the frequency instability of a resonator caused by mechanical vibration in the environment. Applied acceleration due to vibration acts on the effective mass of the resonator resulting in stress and strain in the resonating structure. The acceleration sensitivity arises from both geometric nonlinearity and material nonlinearity. Geometric nonlinearity occurs when the

dimensions of the resonant structure are altered due to sufficiently high strain and material nonlinearity occurs when the strain-dependent material properties of the resonant structure are altered via strain introduced by the ambient vibration. Each of these mechanisms results in a shift in the mechanical structure's resonant frequency [40]. Acceleration sensitivity is mathematically modeled as and experimentally demonstrated to be a vector quantity. The total acceleration sensitivity of a device can be considered the vector sum of the acceleration sensitivities along the principal reference axes.The resonator frequency shift is proportional to the scalar product of the acceleration sensitivity vector and the acceleration of the resonator [41]. This results in many devices composed of materials with anisotropic elastic parameters, such as single crystal silicon (SCS), exhibiting acceleration sensitivities that differ along their principal reference axes. For example, SCS exhibits greater acceleration sensitivity in the direction normal to the <100> plane than in the direction normal to the <110> plane. This is likely a result of a lower Young's modulus and higher Poisson's ratio in the <100> plane relative to the <110> plane [40].

Filler first reviewed the acceleration sensitivity in bulkwave quartz crystal oscillators (QCOs) for both steady-state acceleration and harmonic vibration [41]. Vibration induces a frequency modulation effect on the oscillator output which results in the presence of sidebands. Filler's initial study was motivated by the increasing use of QCOs as precise timing devices in a number of fields such as navigation, communication, and radar where the ambient conditions are characterized by harsh, external vibration.

Acceleration sensitivity in surface acoustic wave (SAW) resonators and surface transverse wave (STW) resonators in discussed by Kosinski and Gualtieri in [42]. They note that neither SAWs nor STWs confer any reduction in acceleration sensitivity advantage relative to each other. Instead, the acceleration sensitivity of acoustic resonators is predominately a function of substrate dimensions and dimensional tolerances. Tiersten *et al* demonstrate analytically that the in-plane sensitivity of a SAW is increased by thickening the device

substrate and that the out-of-plane sensitivity is correspondingly decreased [43]. Micromachined vibration isolators are first introduced in order to reduce the acceleration sensitivities in SAWs and STWs [44, 45, 46]. The emergence and development of this technology will be discussed in Section 2.2.

The vibration sensitivity of micromachined vibratory gyroscopes (MVGs) has also been well investigated. MVGs can be considered one of two types. Type I MVGs measure absolute angle of rotation while Type II MVGs measure angular rate of rotation. Typically, Type I MVGs exhibit a geometry that is rotationally symmetric about the sensing axis. Examples include ring MVGs, disk MVGs, and wine glass mode MVGs [47]. High frequency vibration can induce flexural modes in ring MVGs which lead to responses that are indistinguishable from the desired gyro ouput. Additionally, undesired coupling effects can be amplified due to fabrication imperfections in Type I MVGs. Fabrication imperfections can result in a loss of symmetry in the MVG. This asymmetry results in the undesired coupling of translation and flexural modes. Translation motion can then be coupled into the flexural sense mode resulting in compromised rotation sensing [48].

The most common Type II MVG architecture is the tuning fork gyroscope (TFG). TFGs operate via the Coriolis principle where a proof mass is suspended above a substrate with anchor flexures that connect the proof mass and substrate. This configuration allows the proof mass to oscillate in two orthogonal modes: a drive and a sense mode. A drive mode is generated via electrostatic force at a constant amplitude and the measured sense mode is induced under rotation about the anchor flexure axis [47]. As in Type I MVGs, fabrication imperfections result in vibration-induced errors in TFGs. In particular, mass and stiffness imbalances can result in critical sensing error [49]. While fabrication imperfections can result in vibration-induced error in TFGs, even ideal TFGs are not immune to error due to vibration. Three major sources of error under vibration for ideal TFGs are (1) capacitive nonlinearity at the sense electrodes, (2) capacitive nonlinearity at the drive electrodes which

results in asymmetric electrostatic force along the sense direction, and (3) capacitive nonlinearity at drive electrodes resulting in asymmetric change of drive capacitance. Yoon *et al* suggest that external vibration in the sense axis may result in the most pronounced error as this failure mechanism is implicated in each of the three sources of error. Additionally, induced error is proportional to TFG quality factor (Q) [50].

Vibration sensitivity has been studied for a number of additional oscillating MEMS devices. The vibration sensitivities of square-shaped, Lamè mode oscillators and double-ended tuning fork oscillators have been demonstrated to be comparable to those of QCOs [51, 52].

2.2 Micromachined Vibration Isolators: A Background

A common technique for the reduction of unwanted excitation in a system is vibration isolation. Vibration isolation is the technique of controlling vibration by interposing compact, resilient connections between the vibration source and its surrounding structure (source isolation) or between the surrounding structure and the vibration receiver (receiver isolation) [53]. A simple macro-scale example of source isolation is the insertion of vibration isolators between industrial equipment and their support structures. The isolators reduce the transmission of vibration from the equipment to the support structures and surrounding environment. A simple macro-scale receiver isolation example is the decoupling of electronics on an aircraft from the harsh vibration environment during flight using an isolation mount [54].

Vibration isolation can be either active or passive. Passive vibration isolation typically utilizes springs, masses, and dampers to ensure a desired frequency response given environmental conditions and isolation requirements. The theory of passive vibration isolation will be treated in Chapter 3. Active vibration isolation utilizes feedback control in which motion is measured and compared and force is applied to the system to achieve desired isolation results [55].

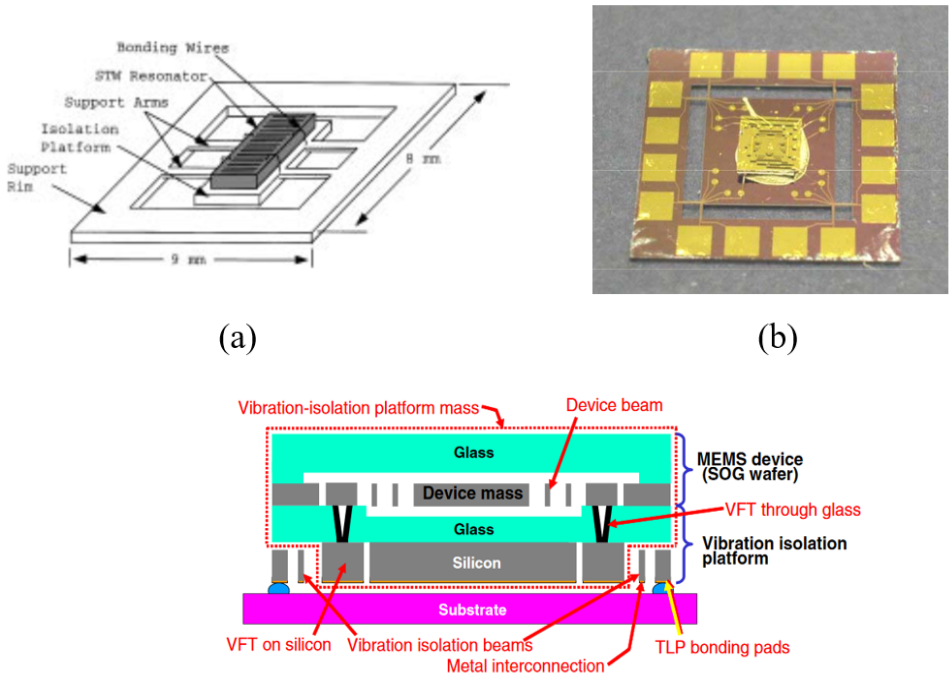

Figure 2.2: Previously fabricated micromachined vibration isolators. (a) First conception of MVI from Reid for isolation of surface acoustic wave resonators [44]. (b) MVI from Dean for isolation of MEMS gyroscopes [57]. (c) Conceptual drawing of high-order vibration isolator from Yoon [58].

Given the performance concerns discussed in Section 2.1, vibration isolation is critical to improve the lifespan and reliability of MEMS sensors in harsh environments. However, integrating a large-scale isolation system is difficult and it introduces components that may be cumbersome and even destructive to the operation of the device being measured. Thus, the need for a non-invasive isolation system on the scale of the MEMS sensor of interest is paramount.

One such technology that meets the aforementioned criteria is micromachined vibration isolators (MVIs). MVIs are passive filters that are fabricated using standard IC fabrication processes such as photolithography, Si etching, and thin-film deposition. They typically possess features on the scale of tens of microns to a few millimeters. MVIs are first introduced by Reid in order to reduce the vibration sensitivity of acoustic wave resonators [56]. The

designed MVI consisted of a central isolation platform which housed the STW resonator and four support arms connecting the platform to a support rim [44]. Mechanical resonance occurred at 1.1 kHz and the isolator exhibited a 40 dB/decade rolloff at frequencies greater than 1.2 kHz.

Dean *et al* applied MVIs to the isolation of MEMS gyroscopes [57]. The constructed MVI consisted of a 2 cm x 2 cm outer frame with eight springs attached to a 1 cm x 1 cm central proof mass pad. The isolated MEMS gyro was attached in die form to the central proof mass pad. The gyroscope electrodes were wirebonded to pads on the isolator central proof mass pad which connected to electrical readout traces along the springs for data probing along the outer frame. The MVI exhibited a resonant frequency of 885 Hz.

Yoon *et al* further developed MVIs for gyroscope isolation through the design and fabrication of a high-order MVI [58]. This MVI provided both lateral and vertical isolation by bonding multiple isolators (platforms) with the assistance of a guide wafer. The stopband attenuation of an MVI can be improved with additional isolation platforms. For N platforms, the MVI acts as a 2-Nth order low pass filter (LPF). Thus, the inclusion of additional isolation stages further reduces the acceleration sensitivity of the isolated device in the isolator's isolation region. However, the fabrication complexity is significantly increased with additional isolation stages. The MVIs fabricated in [57] and [44] require just a single SCS wafer while the MVI fabricated in [58] required four wafers: a double-side polished SCS wafer, a Pyrex 7740 glass wafer, a single-side polished substrate SCS wafer, and a guide SCS wafer. The fabricated MVI exhibited a lateral resonance at 1.3 kHz with a Q of $\approx$2.2 and achieved attenuation beyond 2.1 kHz.

Silicon is not the only material to be proposed as a micromachining substrate for MVI fabrication. In [59], a vibration isolator is proposed with spring flexures composed of a silicon-based polymer, polydimethylsiloxane (PDMS). The use of polymers as both a vibration isolator substrate and as a damping material is discussed in Sections 4.5 and 5.2, respectively.

Chapter 3

Vibration Isolation: Theory and Performance

3.1 Single Degree-of-Freedom Vibration Isolator

A single degree-of-freedom MVI can be modeled as a spring-mass-damper system with an excited base as shown in Figure 3.1 [60]. The mass of the system, M, corresponds to the combination of the masses of the isolated device and the MVI's central platform. The excited base models the outer frame of the MVI as rigidly connected to the substrate of interest and the system stiffness, k, is contributed primarily by the MVI's support arms. System losses, b, are contributed by a number of mechanisms including viscous damping, mechanical energy loss at the spring-outer frame and spring-central platform interfaces (anchor losses), and material losses in the resonant structure due to conversion of elastic energy to heat [62].

The time-domain displacement of the substrate under excitation is given by $x_s(t)$ and the displacement of the isolated mass is $x_m(t)$. The governing equilibrium time-domain equation is:

$$M(\frac{\partial^2 x_m}{\partial t^2}) + b(\frac{\partial x_m}{\partial t} - \frac{\partial x_s}{\partial t}) + k(x_m - x_s) = 0 \tag{3.1}$$

3.1.1 MVI Displacement Transmissibility

The single stage MVI is a second order low-pass filter. After converting to the Laplace domain and solving for $X_m(s)$ divided by $X_s(s)$, the Laplace domain transfer function of the system is given:

$$H(s) = \frac{X_m(s)}{Xs(s)} = \frac{\frac{b}{M}s + \frac{k}{M}}{s^2 + \frac{b}{M}s + \frac{k}{M}} \tag{3.2}$$

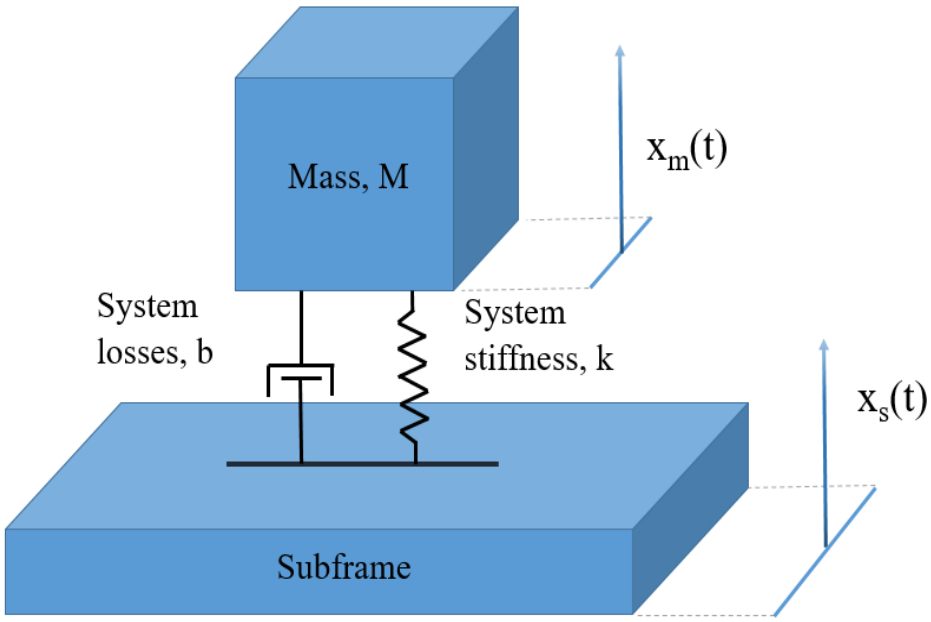

Figure 3.1: Vibration isolation system model with excited base or subframe.

Substituting in the damping ratio, ζ, and the system natural frequency, ω_n, into Eq. 3.2 the transfer function, $H(s)$, can also be considered:

$$H(s) = \frac{2\zeta\omega_n s + \omega_n^2}{s^2 + 2\zeta\omega_n s + \omega_n^2} \tag{3.3}$$

Where the damping ratio is defined:

$$\zeta = \frac{b}{2M\omega_n} \tag{3.4}$$

The system transmissibility is defined as the normalized displacement of the mass divided by the excited base displacement as a function of excitation frequency, ω. Taking the magnitude of $H(s)$ yields the system transmissibility:

$$T = \frac{X_m(\omega)}{X_s(\omega)} = \sqrt{\frac{1 + (2\zeta\frac{\omega}{\omega_n})^2}{(1 - \frac{\omega^2}{\omega_n^2})^2 + (2\zeta\frac{\omega}{\omega_n})^2}} \tag{3.5}$$

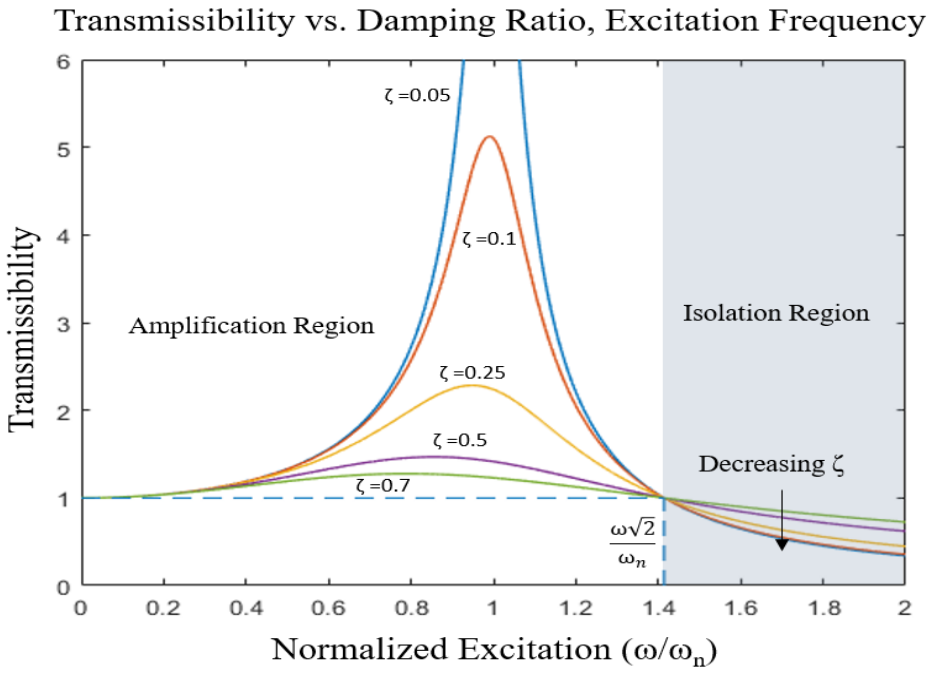

Figure 3.2: Microisolator transmissibilities for varying damping ratios, ζ, as function of normalized excitation frequency.

3.1.2 MVI Frequency Response

Two critical parameters, when designing MVIs, are the quality factor, Q, and the natural frequency, ω_n, of the device [63]. Generally, Q refers to the ratio of average stored energy divided by the energy lost per cycle [61]. Because MVIs can be considered resonators, the Q is inversely proportional to damping. For lightly damped resonators [62]:

$$Q = \frac{1}{2\zeta} \tag{3.6}$$

The undamped natural frequency, ω_n, in radians per second is given by:

$$\omega_n = \sqrt{\frac{k}{M}} \tag{3.7}$$

Figure 3.2 displays the transmissibility profiles for MVIs of varying damping ratios and quality factors as a function of excitation frequency divided by natural frequency. Note that lower damping results in a higher maximum transmissibility and higher attenuation, and

greater damping results in lower transmissibility with reduced attenuation. The transmissibility profile of an MVI can be divided into two regions: the amplification region, in which the transmissibility of the isolator is above unity, and the isolation region, in which the transmissibility drops below unity. The frequency at which this transition occurs is considered the isolation frequency. For all second-order excited base systems, the isolation frequency can be defined:

$$\omega_{iso} = \sqrt{2}(\omega_n) \tag{3.8}$$

3.1.3 Transmissibility and Acceleration Sensitivity

Ambient acceleration acting on a resonant device results in a shift of the device's resonant frequency that is proportional to the device's acceleration sensitivity. This frequency shift can be described mathematically [41]:

$$f(\overrightarrow{a}) = f_0(1 + \overrightarrow{\Gamma} \cdot \overrightarrow{a}) \tag{3.9}$$

Where f_0 is the unperturbed resonant frequency of the device, $\overrightarrow{\Gamma}$ is the device's acceleration sensitivity, $\overrightarrow{a}$ is the acceleration vector of the ambient environment acting on the device, and $f(\overrightarrow{a})$ is the resulting, shifted resonant frequency. The introduction of a vibration isolation device amends Equation 3.9 such that the resulting frequency shift is also a function of the transmissibility of the isolation device. The resulting expression is:

$$f(\overrightarrow{a}) = f_0(1 + \overrightarrow{\Gamma} \cdot (\overrightarrow{T}(f) \cdot \overrightarrow{a})) \tag{3.10}$$

Where the vector $\overrightarrow{T}(f)$ is the isolation device's transmissibility at the excitation frequency f such that:

$$\overrightarrow{T}(f) = T_x(f)\hat{x} + T_y(f)\hat{y} + T_z(f)\hat{z} \tag{3.11}$$

Note in Equation 3.10 that the frequency shift is amplified when $T(f)$ is greater than unity along a particular axis ($f < f_{iso}$) and the frequency shift is attenuated when $T(f)$ is less than unity ($f > f_{iso}$).

3.2 Damping Phenomena in Vibration Isolators

MVIs can exhibit considerable transmissibility magnitudes when subject to spectral energy near the MVIs resonant frequency. Silicon has low mechanical losses which results in low internal damping [64],[65]. Thus, MVIs need to be further damped in order to mitigate resonance-induced acceleration sensitivity in isolated devices and to prevent potential damage to the MVI itself. Wide bandwidth shock excitation is a particular concern. The follow sections detail the theory, performance, and notable phenomena of heavily damped MVIs.

3.2.1 Transmissibility and Resonant Frequency Shift

For lightly damped vibration isolation systems ($\zeta < 0.1$), the maximum transmissibility, T_{peak}, exhibited by the system and the quality factor as defined in Equation 3.6 are approximately equal [66]. Additionally, the resonant frequency at which T_{peak} occurs, ω_r, is approximately equal to the system natural frequency, ω_n.

However, when damping becomes considerable ($\zeta > 0.1$), the actual values for T_{peak} and ω_r deviate considerably from the previous approximations. Solving for the frequency ratio which yields T_{peak} using Equation 3.5 gives the expression for ω_r under heavy damping:

$$\omega_r = \frac{\omega_n}{2}\sqrt{\frac{\sqrt{1+8\zeta^2}-1}{\zeta^2}} \tag{3.12}$$

Substituting Equation 3.12 back into Equation 3.5 yields T_{peak} as a function of the damping ratio:

$$T_{peak} = \frac{2\sqrt{2}(\zeta^2)}{\sqrt{8\zeta^4+\sqrt{1+8\zeta^2}-4\zeta^2-1}} \tag{3.13}$$

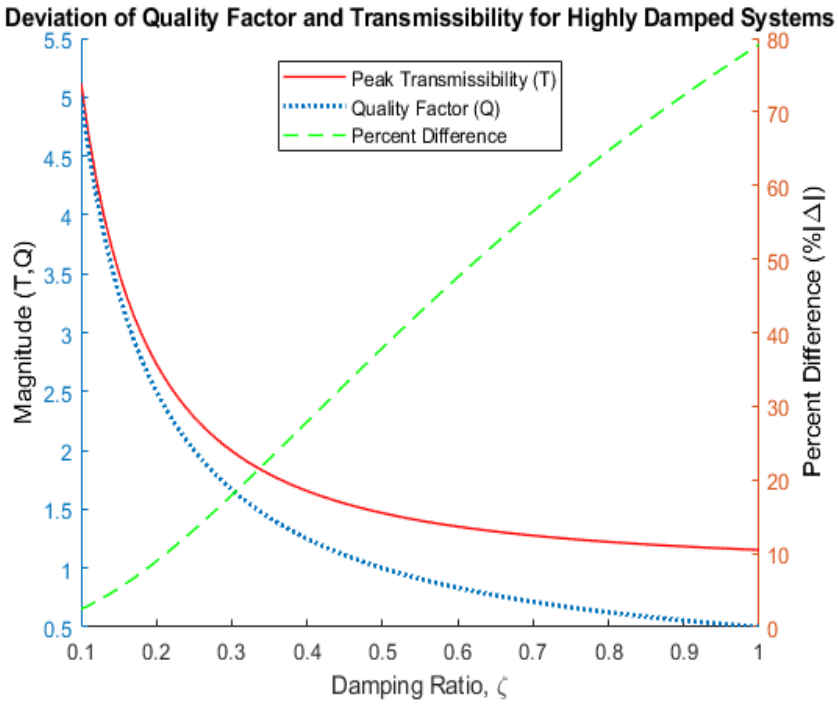

Figure 3.3: Quality factor and maximum transmissibility deviation for vibration isolation systems with $\zeta > 0.1$. These differences become considerable for systems with Q < 5.

A detailed derivation of Equations 3.12 and 3.13 is provided in Appendix A.

Figure 3.3 graphically depicts the deviation between the quality factor and the maximum transmissibility for highly damped systems. Note that the percent difference between Q and T_{peak} is just 2.4% for $\zeta = 0.1$ and almost 80% for $\zeta = 1$.

3.2.2 Viscoelastic Damping in Vibration Isolation

The damping treatment in the previous sections assumes that the damping mechanism and the stiffness mechanism of the isolation system are independent of one another. However, often materials such as rubber, viscoelastic polymers, and viscous fluids are used for damping which contribute both damping and added stiffness to the system. Such a configuration can be modeled as an elastically connected viscous damper [66]. Viscoelastic solids are often approximated by the Kelvin-Voigt model and viscoelastic fluids are often approximated by the Maxwell fluid model [67]. Figure 3.4 depicts the elastically connected viscous damper

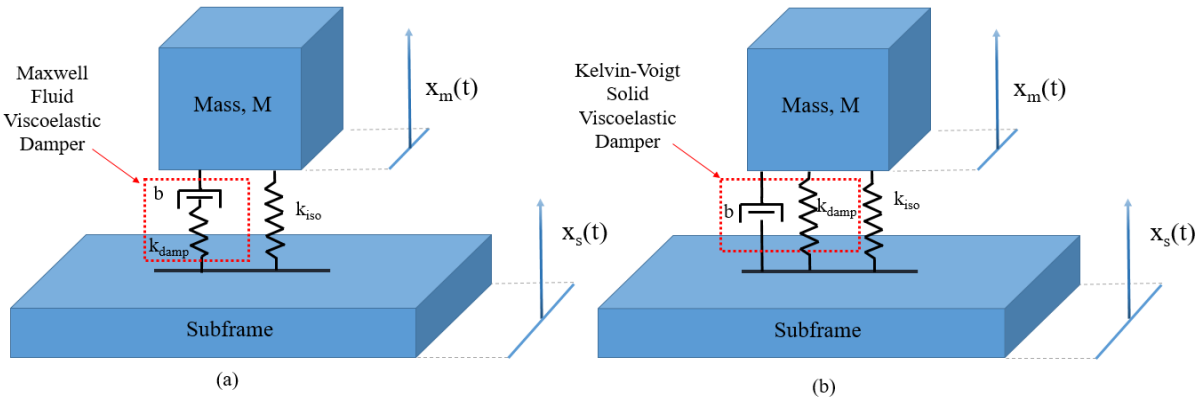

Figure 3.4: Vibration isolation system model with an elastically connected damper contributing additional stiffness, k_{damp}, to the stiffness.(a) Maxwell fluid damping model. Damping is added in series with the added stiffness. (b) Kelvin-Voigt damping model. Damping is added parallel to the damper stiffness.

configuration for both the Kelvin-Voigt and Maxwell models. Note the added stiffness and damping are in parallel for the Kelvin-Voigt model and in series in the Maxwell model. For simplicity, it is assumed the damping contribution, b, is dominated by the viscoelastic damper. The damper's stiffness contribution is given by k_{damp}. Note that k_{damp} can be expressed as a ratio of the isolator's stiffness, k_{iso}:

$$k_{damp} = N(k_{iso}) \tag{3.14}$$

Where N is considered the stiffness ratio. The transmissibility of the Maxwell fluid damped isolator can be given as a function of N such that [66]:

$$T_{Maxwell} = \sqrt{\frac{1 + 4(\frac{N+1}{N})^2\zeta^2\frac{\omega^2}{\omega_n^2}}{(1 - \frac{\omega^2}{\omega_n^2})^2 + \frac{4}{N^2}\zeta^2\frac{\omega^2}{\omega_n^2}(N + 1 - \frac{\omega^2}{\omega_n^2})^2}} \tag{3.15}$$

Figure 3.5(a) presents the transmissibility curves for a Maxwell fluid damped vibration isolator with constant N = 3 and variable damping ratios for $0.01 \leq \zeta \leq 10$. Because of the series coupling of the fluid's damping and stiffness, the system does not exhibit an increase

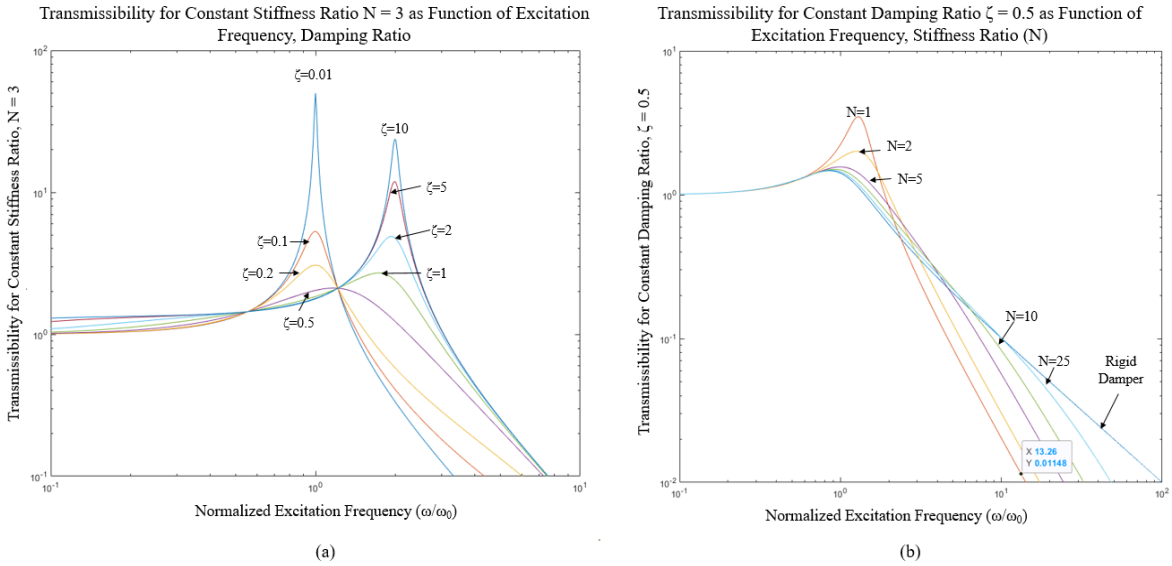

Figure 3.5: Transmissibility curves for an elastically connected Maxwell fluid damper. (a)Transmissibility for range of damping ratios and constant stiffness ratio. Note that for very high damping ratios ($\zeta \geq 1$) the resonant frequency shifts upward. (b)Transmissibility for range of stiffness ratios and constant damping ratio. As N approaches infinity the system begins to approximate a rigidly connected damper configuration.

in resonant frequency until very high damping. As ζ approaches ∞ the resonant frequency of the system becomes a function of the added stiffness such that:

$$\omega_{r,\zeta=\infty} = \sqrt{\frac{k_{iso} + k_{damp}}{M}} = \sqrt{N+1}(\omega_n) \tag{3.16}$$

Figure 3.5(b) presents the curves for constant ζ and variable stiffness ratios in the Maxwell fluid damped isolator. Note that low values of stiffness result in increased transmissibility and attenuation. For increased values of N the system begins to approximate the rigidly connected damper. The resonant frequency approaches the undamped resonant frequency for N = ∞:

$$\omega_{r,N=\infty} = \sqrt{\frac{k_{iso}}{M}} = \omega_n \tag{3.17}$$

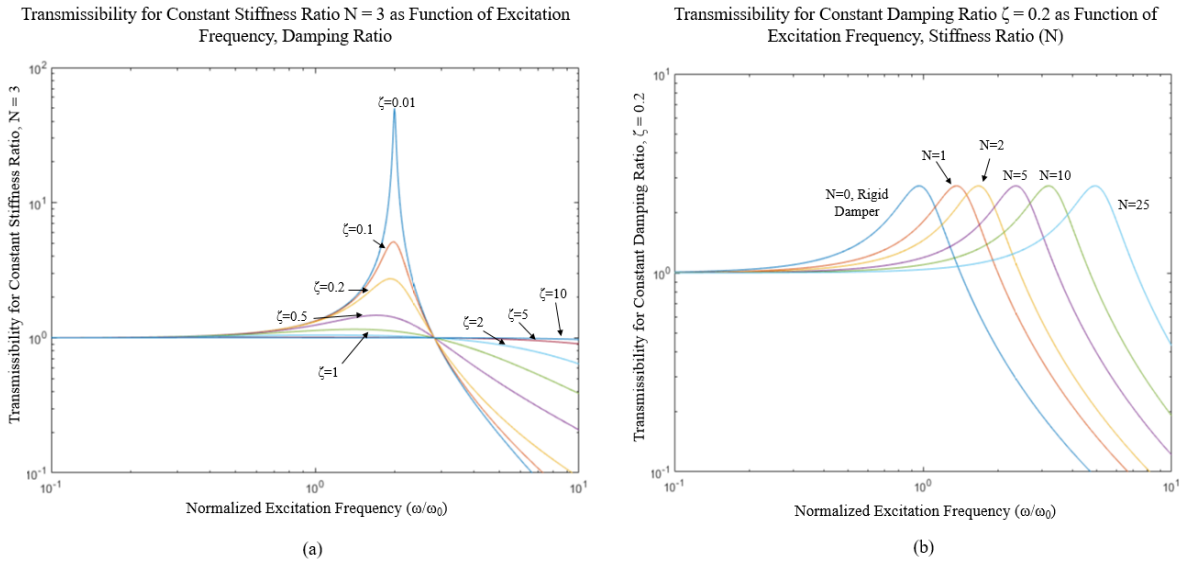

Figure 3.6: Transmissibility curves for a Kelvin-Voigt solid damped vibration isolator. (a)Transmissibility for range of damping ratios and constant stiffness ratio. In contrast to the Maxwell model, the resonance shifts downward for high damping. Resonant frequency at both low and high damping is a function of stiffness. (b)Transmissibility for range of stiffness ratios and constant damping ratio. As N approaches zero the system approximates a rigidly connected damper configuration.

The transmissibility of a Kelvin-Voigt solid damped vibration isolator closely resembles the transmissibility given by Equation 3.5. Because the spring elements are in parallel they can simply be added such that the natural frequency is a function of the sum of k_{iso} and k_{damp}:

$$\omega_n = \sqrt{\frac{k_{iso} + k_{damp}}{M}} \tag{3.18}$$

Then the transmissibility is precisely that given in Equation 3.5 and need not incorporate the stiffness ratio, N. Alternatively, the transmissibility can be expressed in terms of N. In that case:

$$T_{Kelvin-Voigt} = \sqrt{\frac{N + 1 + 4\zeta^2(\frac{\omega}{\omega_n})^2}{N + 1 - 2(\frac{\omega}{\omega_n})^2 + \frac{(\frac{\omega}{\omega_n})^4}{N+1} + 4\zeta^2(\frac{\omega}{\omega_n})^2}} \tag{3.19}$$

Figure 3.6(a) presents the transmissibility curves for a Kelvin-Voigt damped vibration isolator at a constant stiffness ratio. Note the shift down in resonant frequency as the damping ratio increases. In this model the resonant frequency approaches Equation 3.18 as damping approaches zero. Contrast this with Equation 3.16 for the Maxwell fluid damped system which approaches the same resonant frequency as damping approaches infinity. An additional point of contrast is that the peak transmissibility of the Maxwell fluid damped system approaches infinity as the damping ratio approaches infinity while the Kelvin-Voigt damped system approaches the minimum possible transmissibility: unity.

Figure 3.6(b) presents the transmissibility of a Kelvin-Voigt solid damped vibration isolator for a constant damping ratio. Note that the variation of N has no effect on the transmissibility magnitudes of the system. Only the resonant frequency is shifted via the added stiffness. Again, the Kelvin-Voigt model contrasts the Maxwell model as the expression for resonant frequency given in Equation 3.17 is achieved at N=0 in the Kelvin-Voigt damped isolator.

A significant portion of this dissertation discusses the novel implementation of viscoelastic materials to damp the dynamic response of an MVI. These materials include microfibrous meshes and polymers that are best modeled using the Kelvin-Voigt formulation.

3.2.3 Loss Factor Damping

The energy loss due to viscoelastic damping under steady-state vibration is often characterized by the loss factor. The loss factor, unlike the damping ratio, is considered a material parameter and is included in the consitutive equations for the Maxwell and Kelvin-Voigt viscoelastic models [68]. Kelvin-Voigt viscoelastic materials can be considered to have a complex modulus of elasticity, E^*, such that [60]:

$$E^* = E(1 + j\eta) = E' + jE'' \tag{3.20}$$

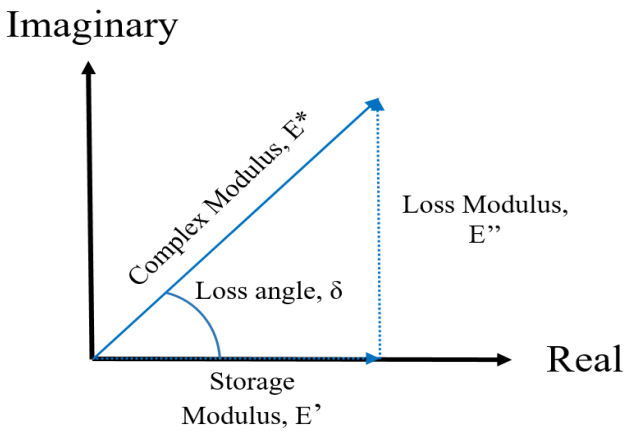

Figure 3.7: Complex modulus of elasticity for viscoelastic materials.

Where E' is the storage modulus and E'' is the loss modulus as shown in Figure 3.7. Recall the modulus of elasticity or Young's modulus is given as the ratio of stress (σ) over strain (ϵ) in a linearly elastic material [69]:

$$E = \frac{\sigma}{\epsilon} \tag{3.21}$$

The complex modulus in viscoelastic materials results in a complex stiffness:

$$k^* = k(1 + j\eta) = k' + jk'' \tag{3.22}$$

Where η is the loss factor defined as [70], [71]:

$$\eta = (\frac{b}{k})\omega = \frac{k''}{k'} = \frac{E''}{E'} \tag{3.23}$$

Note the frequency dependence of the loss factor. This contrasts with the damping ratio expression given in Equation 5. At $\omega = \omega_n$ the relation between η and ζ is:

$$\eta \approx 2\zeta \tag{3.24}$$

A critical distinction is that the loss factor is *frequency* specific (among other parameters such as temperature) to a particular material and the damping ratio is *mode* specific to a particular system. Often, the loss factor of a material is given as the loss factor at resonance, but the loss factor of a material cannot be considered under non-steady-state conditions, such as transients [72]. However, the damping ratio is still applicable.

Chapter 4

Micromachined Vibration Isolator Design, Fabrication, and Dynamic Performance

The fundamental geometry of an MVI consists of three constituent structures: (1) a central platform which accommodates the isolated device or sensor, (2) an outer frame which is affixed to the substrate under study, and (3) spring flexures which couple the outer frame to the central platform. Figure 4.1 demonstrates the MVI fundamental geometry with an added sensor package. The MVIs discussed in this dissertation are intended to accommodate small, commercially-available, pre-packaged surface-mount devices (SMDs). A few previous MVI designs have incorporated unpackaged devices, yet the fundamental geometry remains the same.

The isolator geometry ultimately defines the performance of the isolator. Appropriate design of the spring flexures and central platform mass is critical to ensure the isolator exhibits the dynamic response necessary for desired sensor isolation. In addition to the primary resonant mode, additional resonant modes of the MVI must be considered during design.

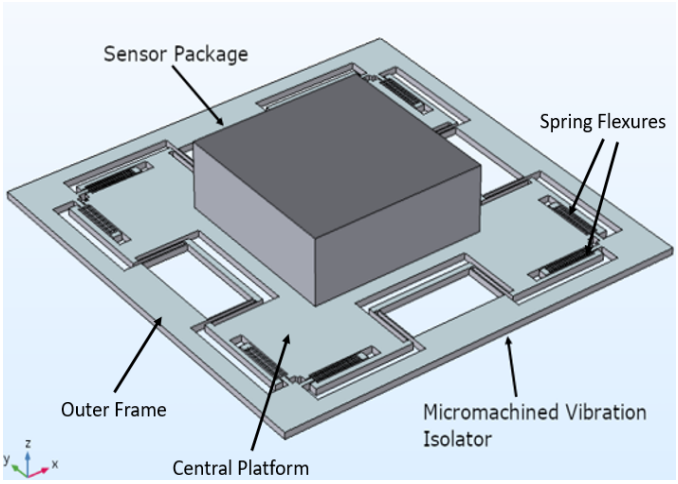

Figure 4.1: Fundamental micromachined vibration isolator geometry and constituent structures.

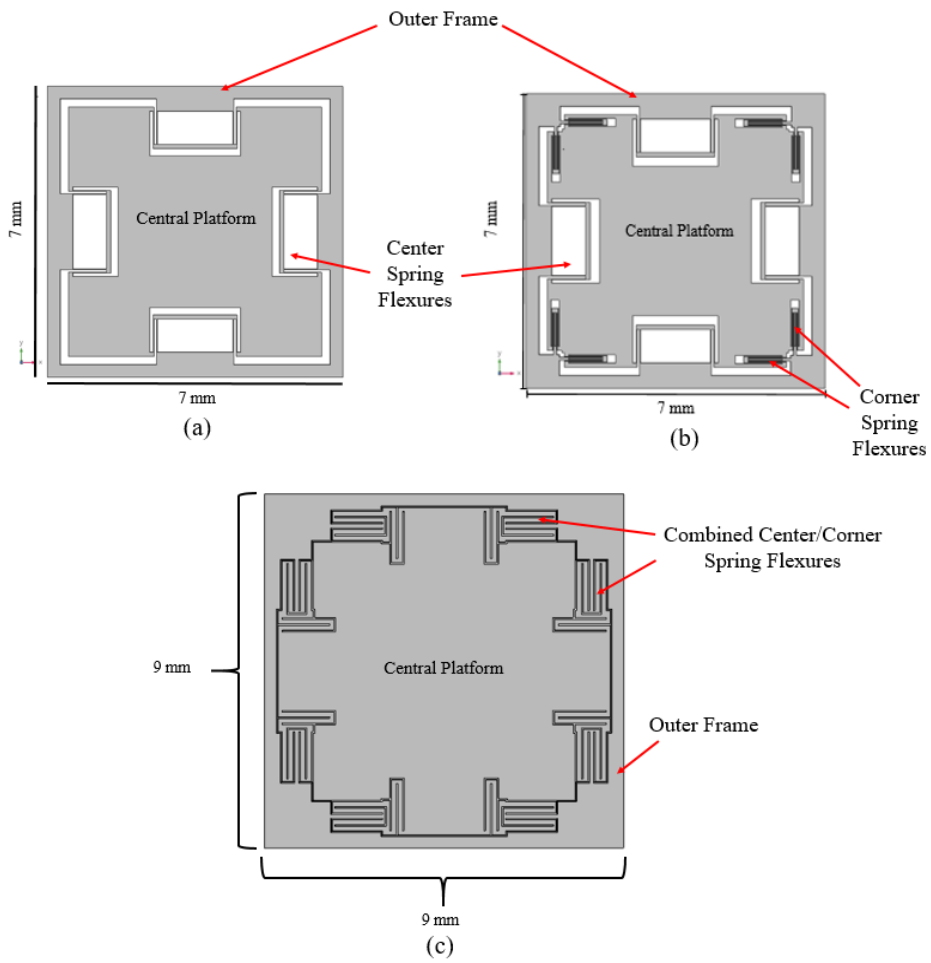

Figure 4.2: Three MVI designs. (a) MVI Variation 1, I1, with centered spring flexures. (b) MVI Variation 2, I2, with added corner spring flexures. (c) MVI Variation 3, I3, with combined center and corner flexures.

The following sections will detail design principles for MVIs and a fabrication methodology for MVIs. Three MVI designs will be compared and contrasted. A detailed description of the design, fabrication, and testing of the first two MVI designs is published in [73].

4.1 Micromachined Vibration Isolator Design

MVI design often requires the consideration of many tradeoffs. Notably, a reduced Q results in reduced attenuation in the isolation region (Figure 3.2) and often improved damping results in a shifted ω_r (Figures 3.5, 3.6) that differs dependent upon the damping mechanism and severity. Additionally, the MVI designer must be aware of the ambient

bandwidth and respective acceleration magnitudes of the environment for which the isolator is designed.

Two parameters of utmost consequence to the isolator's performance are the isolation frequency, f_{iso}, and the peak transmissibility, T_{peak}. While often the isolator's Q and ω_r are considered the most important parameters in MVI design [63], T_{peak} and f_{iso} characterize the filtering performance of the isolator more generally in cases of both low and high damping. For example, the Q of a Maxwell fluid damped vibration isolator may be extremely low due to high damping, but T_{peak} *increases* as the system becomes more damped. Thus, the quality factor of the system is not representative of the increased acceleration sensitivity in the MVI's amplification region. Additionally, ω_r shifts downward from ω_n in a solid damped MVI for increased damping. However, f_{iso} remains the *same*.

Figure 4.2 displays the three MVI variations designed, simulated, fabricated, and tested in this work. The MVIs are abbreviated the I1, I2, and I3 variations in the order they were chronologically developed.

4.1.1 Design of Spring Flexures

The spring flexures are the most important structures in defining the frequency response of the MVI. The spring flexures are the only coupling mechanism between the isolated sensor and the substrate of interest. The mass and dimensions of the isolated sensor cannot be controlled and the sensor mass may dominate the total effective mass of the system. Thus, there is minimal control over the effective mass of the isolation system without the addition of a countermass. However, considerable control over the effective stiffness of the system is available in the number, geometry, and distribution of the spring flexures. Additionally, micromachining techniques such as photolithography and Si etching allow for precise control over flexure dimensions. A design procedure for spring flexures for a viscoelastic solid damped MVI is presented in Appendix B.

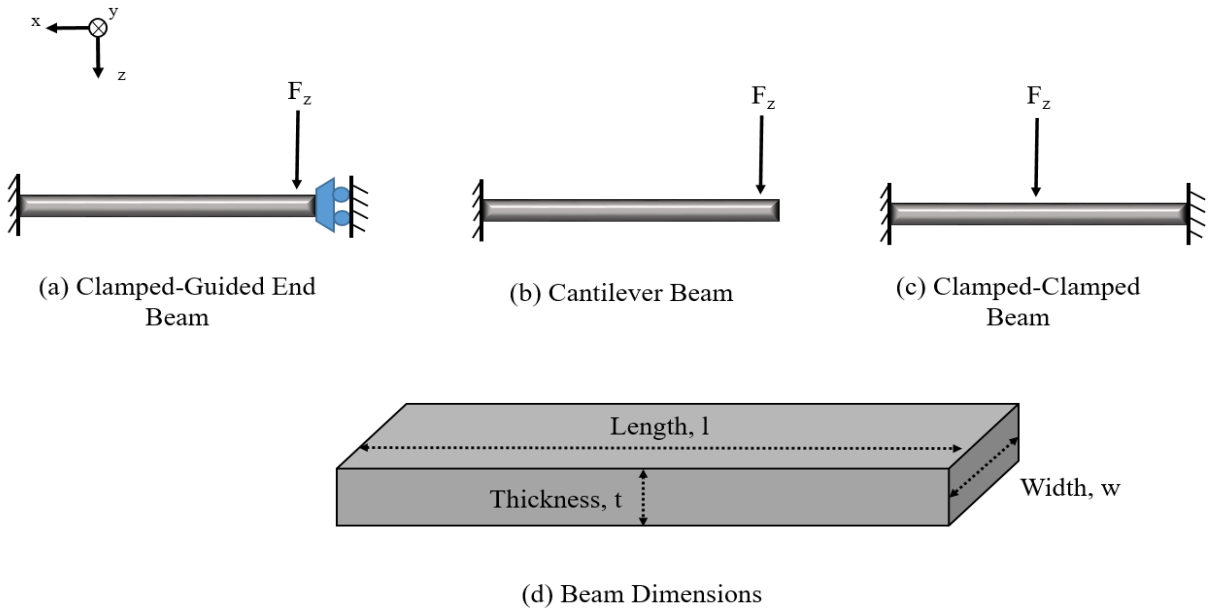

Figure 4.3: Beam models for spring constant estimation under concentrated load. (a) Clamped-Guided end beam. (b) Cantilever beam. (c) Clamped-clamped beam. (d) Critical dimensions for beam design and spring constant determination.

4.1.2 MVI Spring Flexure Model

The clamped-guided end beam model with a concentrated load is the appropriate model for determining the spring constant of the MVI's spring flexures for the MVI's primary out-of-plane resonant mode [74]. The model is presented in Figure 4.3(a) and is contrasted with the cantilever beam and clamped-clamped beam models. The model assumes that the beam face attached to the central platform (y,z plane in Figure 4.3) moves parallel to the plane of the rigid attachment at the other end of the beam: the outer frame in the case of an MVI. The out-of-plane (z-axis) spring constant for a spring element of this type under concentrated load is given:

$$k_{SE} = \frac{Ewt^3}{l^3} \tag{4.1}$$

Where E is the Young's modulus, w is the width of the beam, t is the beam's thickness, and l is the length of the beam as defined in Figure 4.3(d). Silicon is an anisotropic material

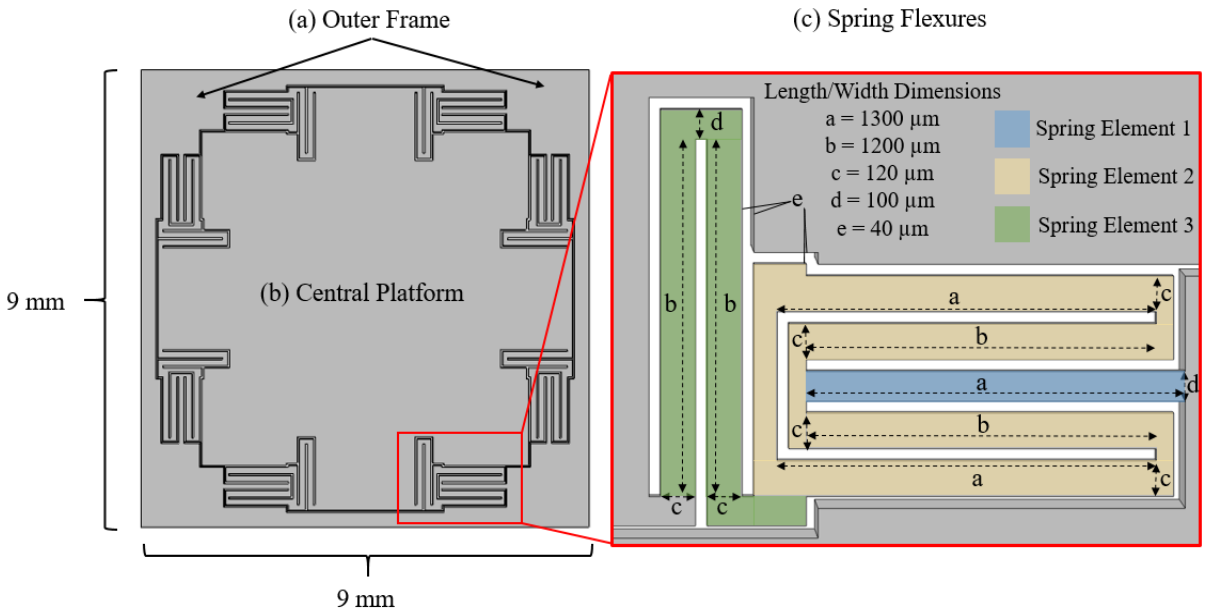

Figure 4.4: I3 vibration isolator with critical spring dimensions. (a)Outer frame. (b)Central platform. (c)Spring flexure dimensions and folded spring divided into constituent spring elements for stiffness approximation. Thickness of all spring elements is 100 μm.

in which E varies from 130 GPa along the <100> direction to 188 GPa along the <111> depending on the crystal orientation. For <100> Si wafers, the out-of-plane E is 130 GPa [75].

The orthogonal spring constants for the guided end beam are [74]:

$$k_x = \frac{Ewt}{l} \tag{4.2}$$

$$k_y = \frac{Etw^3}{l^3} \tag{4.3}$$

In these expressions E is along the <110> direction and is equal to 169 GPa [75].

4.1.3 Folded Spring Flexures

Often the stiffness provided by a spring composed of a single, straight beam is too great to achieve the desired ω_r and f_{iso} of the system. While beam dimensions can be

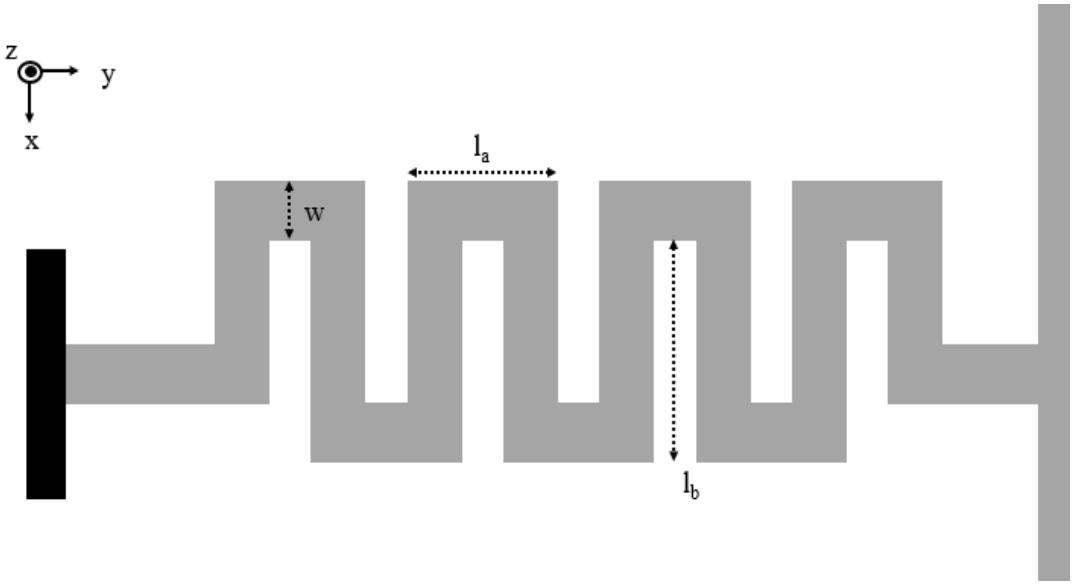

Figure 4.5: Serpentine spring schematic: An example of a folded spring structure

modified, fabrication tolerances often limit achievable feature sizes. Notably, the thickness of the isolator springs is often defined by the device layer thickness of a silicon-on-insulator (SOI) wafer. Additionally, the footprint of the isolator cannot be exceeded and spring widths must be large enough to accommodate electrical readout traces. The addition of folds to the spring flexures allows an alternative method to reduce the system stiffness. Figure 4.4 displays the spring dimensions for the I3 MVI. An approximation of the overall stiffness of the folded flexure can be made by considering the flexure a series combination of the three spring elements:

$$\frac{1}{k_{flex}} = \frac{1}{k_{SE_1}} + \frac{1}{k_{SE_2}} + \frac{1}{k_{SE_3}} \tag{4.4}$$

Note that the definition of the spring elements is arbitrary and is made to simplify approximation of k_{flex}. A similar analysis can be applied to the corner flexures on the I2 MVI. Strict derivation of spring constants for folded springs is complex and a number of examples are presented in [74]. An approximation of the out-of-plane stiffness for serpentine folds shown in Figure 4.5 is given in [76]:

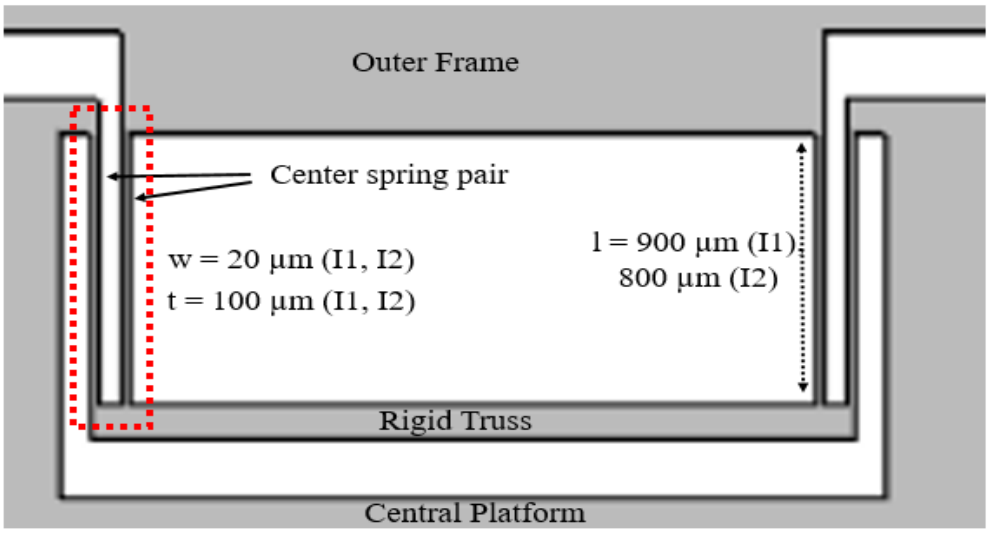

Figure 4.6: Center spring schematic for I1, I2 MVIs. Springs connected via rigid truss. Spring pairs can be considered series combination of clamped-guided end beams.

$$k_z \approx Ew(\frac{t}{nl_a})^3 \tag{4.5}$$

Where n is the number of meanders or folds. The approximation holds for $l_a >> l_b$.

Another example of folded spring structures in the MVIs explored is the truss-connected spring flexure in the I1 and I2 center springs. Figure 4.6 shows the truss-connected spring flexures with the flexure dimensions. For simplicity of analysis the truss is assumed to be rigid such that the effective spring constant can be considered a series combination of clamped-guided end beams [77]. Equations 4.1 and 4.4 can then be applied to determine the effective stiffness of the center spring pair.

The total spring constant for an MVI can be considered the parallel combination of the spring flexure stiffnesses. For N flexures the total spring constant is:

$$k_{iso} = N(k_{flex}) \tag{4.6}$$

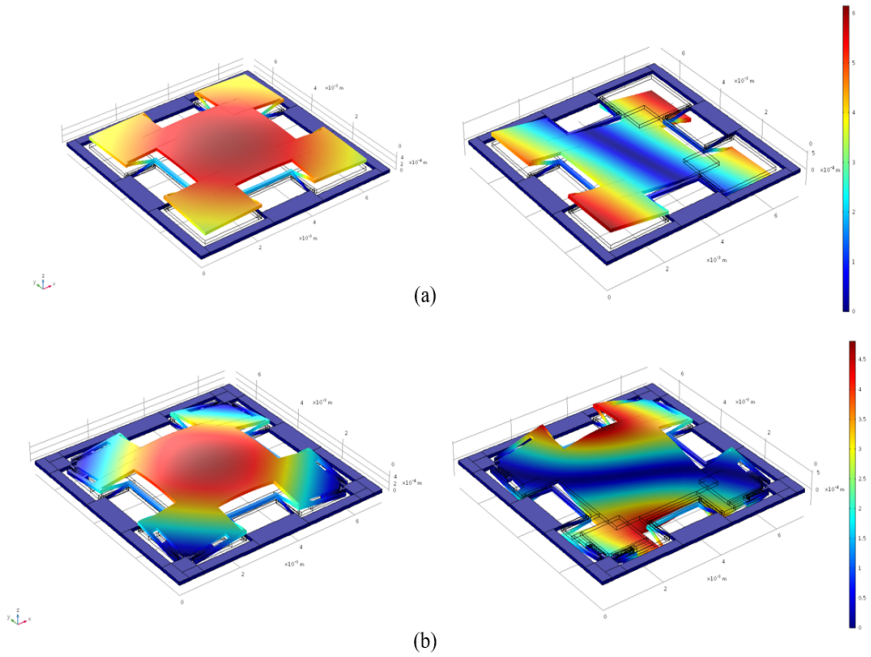

Figure 4.7: First and second eigenmodes for isolator I1 (a) and isolator I2 (b) with normalized displacement.

4.1.4 Corner Spring Inclusion in I2

The I2 design closely resembles the I1 design with the notable addition of flexures in the corners. The addition of the corner flexures serves two major purposes: (1) it provides added stiffness to the rotational modes that occur after the primary resonant mode, resulting in higher resonant frequencies for these modes and (2) it reduces the stress induced on the center springs under acceleration. Figure 4.7 displays the first and second eigenmodes for the I1 and I2 isolators. COMSOL Multiphysics was used for all finite element analysis (FEA) simulations in this dissertation. The primary resonant mode is suppressed in I2 relative to I1 due to the corner spring flexures. Also, the second rotational mode present in I1 no longer occurs along y-axis, but at approximately 45 degrees between the y and x axes.

Figure 4.8 presents the simulated first and second eigenfrequencies (Figure 4.8 (a)) for the I1 and I2 isolators (V1 and V2 in the image) as a function of center spring length. A 110 mg mass is applied to the central platform to emulate the mass of a sensor. The inclusion

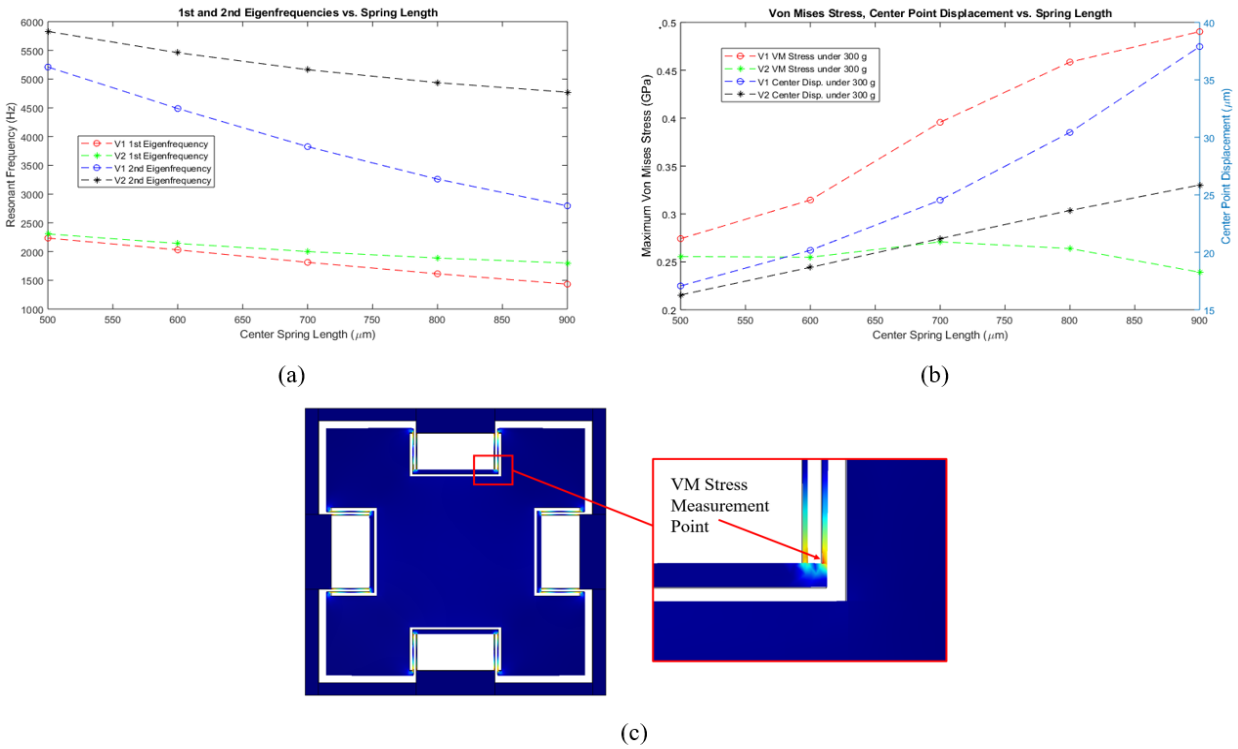

Figure 4.8: Critical design parameters as function of center spring lengths from 500 to 900 μm for I1 (V1) and I2 (V2). (a) First and second eigenfrequencies. (b) Center point displacement and Von Mises stress measurement at center spring/truss juncture shown in (c) under 300 g load.

of corner flexures drives the second resonance mode to a significantly higher frequency as compared to the I1 for longer center springs.

Figure 4.8 (b) presents a comparison of the center point displacement and the Von Mises (VM) stress at a point defined in Figure 4.8 (c) under a static 300 g load applied to the central platform along the z-axis. The 300 g load condition applied to the central platform emulates a typical low bandwidth, far field pyroshock load present in many harsh environments [78]. Both the center point displacement and VM stress at the center spring flexure/truss juncture are notably reduced with the addition of corner flexures to the isolator. For longer center spring lengths the Von Mises stress is actually reduced in the I2 as more stress is transferred to the corner springs. Ultimately, 800 μm and 900 μm center springs are selected for the I1 and I2 isolators, respectively, for fabrication and testing.

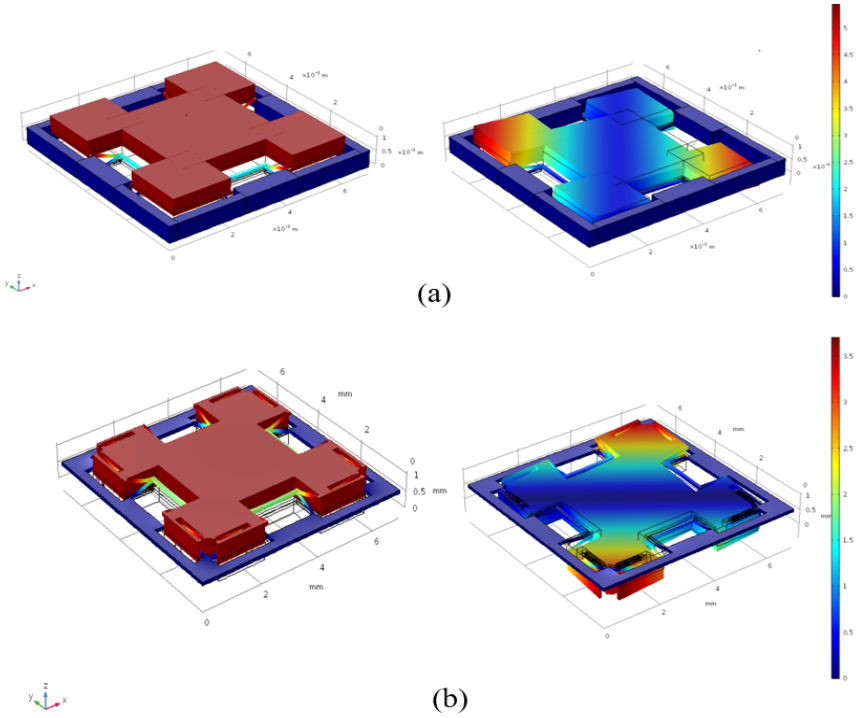

Figure 4.9: First and second eigenmodes for isolator I1 (a) and isolator I2 (b) with handle layer of central platform included.

4.1.5 Central Platform Design

The area of the central platform must be large enough to house the isolated sensor and the electrical readout traces. An additional design decision must be made whether to keep the SOI handle layer on the device's central platform. The removal/inclusion of the SOI handle layer results in fundamentally different resonant modes when the isolator is unloaded with a sensor or test mass. The FEA results of Section 4.1.4 displayed in Figure 4.7 and 4.8 are for an isolator whose central platform has only a 100 μm thickness due to Si etch removal of the handle layer beneath the central platform. Inclusion of the SOI handle layer adds an additional 500 μm to the central platform thickness.

Figure 4.9 displays the first and second eigenmodes for the I1 and I2 with handle layer included in the central platform. The resonant modes in Figure 4.7 are flexural modes which exhibit bending across the central platform. This is due to the uniform thickness of the

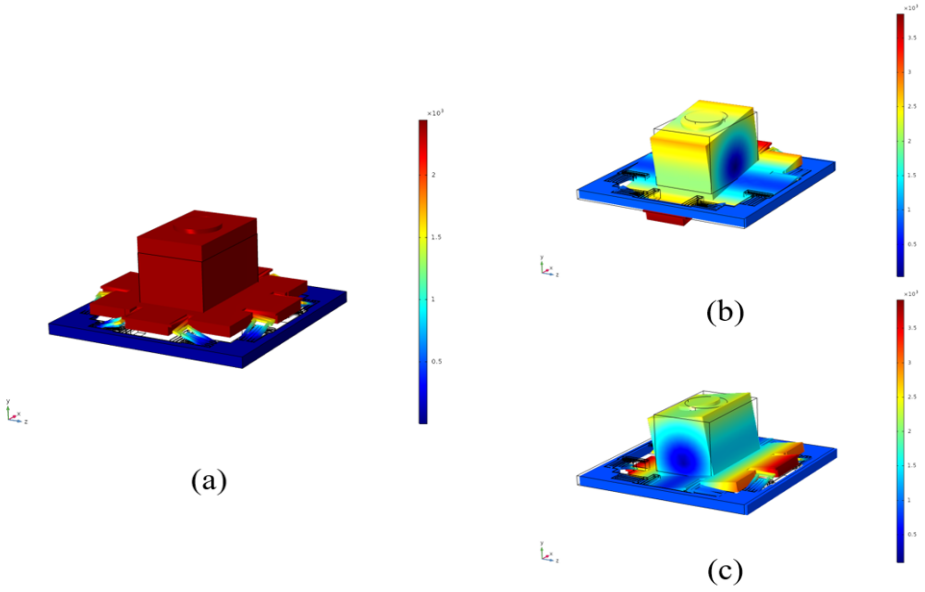

Figure 4.10: FEA Simulated Resonant Modes for I3 MVI with added proof mass. (a) First eigenmode at 844 Hz. (b) Second eigenmode at 1245 Hz. (c) Third eigenmode at 1371 Hz. Frequency split between second and third modes is due to different in-plane dimensions of the proof mass (3 mm vs. 4.5 mm).

spring flexures and the central platform. This configuration results in a reduced k_{iso} as the central platform can be considered a spring element in series with the flexures.

In contrast, the resonant modes in Figure 4.9 show the central platform oscillating as a uniform mass with flexing confined to the isolator's springs. The inclusion of the SOI handle layer provides a more equal center of mass and center of elasticity by serving as a counter mass to the isolated sensor's mass. Despite a five-fold increase in central platform mass, the resonant frequencies in I2 increase and remain the same in I1 due to drastic increase in k_{iso}.

Table 4.1: FEA Simulated Eigenfrequencies for I1, I2 Variations

Variation	**1st Eigenfrequency (kHz)**	**2nd Eigenfrequency (kHz)**	**Ratio (2nd/1st)**
I1 w/o substrate	1.432	3.5	2.44
I2 w/o substrate	1.800	4.772	2.65
I1 w/ substrate	1.410	2.146	1.52
I2 w/substrate	2.582	3.58	1.39

Table 4.1 presents the first and second eigenfrequencies for the I1 and I2 MVIs both with and without the central platform substrate.

The I3 MVI was only fabricated and tested with the central platform substrate included. Figure 4.10 displays the first, second, and third simulated resonant modes for the I3 design. A 110 mg aluminum (Al) test mass is added to the isolator to emulate the mass and boundary conditions of an isolated sensor. The 110 mg mass is added to the I1, I2 simulation but as a distributed mass across the central platform. The I3 emulation more closely approximates the boundary conditions of an isolated sensor. Note the frequency split between the second and third modes. This is due to unequal lengths of the proof mass in the respective in-plane axes. Ideally, the two modes would be degenerate for a square proof mass. The simulated proof mass is intended to model the Al proof masses available for experimental testing.

Table 4.2 gives the system parameters for the I1, I2, and I3 MVI variations with handle layer substrate remaining. Note that the system mass consists of the central platform mass plus the mass of an Al proof mass (110 mg). The spring flexure stiffnesses for each MVI variation, k_{flex}, are estimated using the spring constant approximations in Sections 4.1.2 and 4.1.3. Note the I2 variation has both center (8 total) and corner springs (8 total). Thus, k_{iso}

Table 4.2: System Parameters for I1, I2, and I3 MVI variations with handle layer substrate

MVI Variation	**Central Platform Mass (mg)**	**System Mass (mg)**	**Spring flexure stiffness, k_{flex} (kN/m)**	**Total isolator stiffness, k_{iso} (kN/m)**	**Calc. Natural Freq.,f_n (kHz)**	**FEA Sim. Natural Freq., f_n (kHz)**
I1	30	140	1.78	14.26	1.61	1.41
I2	27.5	137.5	2.54 (center) 2.54 (corner)	40.63	2.74	2.5
I3	70	180	0.643	5.142	0.850	0.844

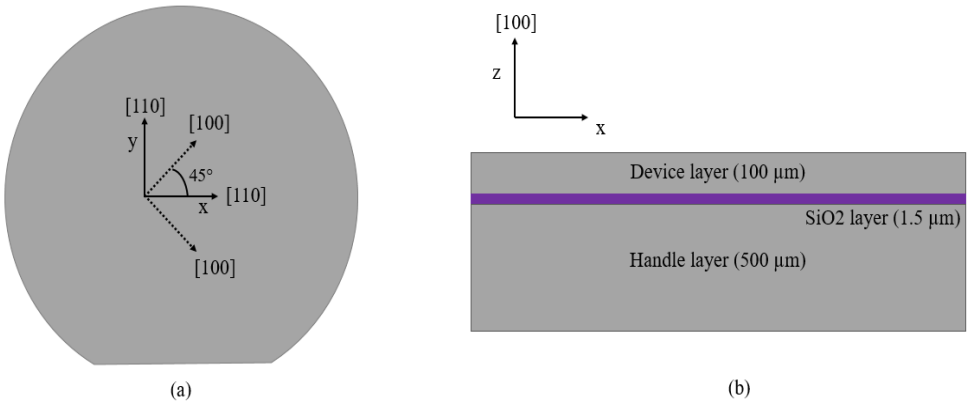

Figure 4.11: Silicon-on-insulator wafer schematic with Si crystal orientations. (a) Top-down view along z-axis. <100> planes are 45° from x,y axes of wafer. (b) Cross-sectional view along y-axis. The <100> direction is normal (along the z-axis) to the surface of the wafer.

for I2 is approximated as the sum of the contributed stiffnesses from both the 8 center and 8 corner springs. Natural frequencies calculated using the estimated stiffnesses match well to primary resonant frequencies observed in FEA simulation.

4.2 MicroIsolator Fabrication

MVIs are batch fabricated from 100 mm diameter silicon-on-insulator (SOI) wafers composed of a 100 μm thick device layer, 500 μm thick handle layer, and a 1.5 μm buried oxide layer. The out-of-plane Si crystal orientation is the <100> plane as shown in Figure 4.11. Standard microfabrication techniques including UV lithography and deep reactive ion etching (DRIE) of Si are used to define the MVI geometry and constituent structures.

One of the primary advantages of using an SOI substrate is the ability to define the spring flexure thicknesses with the SOI device layer. Note the out-of-plane spring constant scales with t^3 as in Equation 4.1. Any process variation (inconsistent etch depths during DRIE) yielding non-uniform spring flexure thicknesses can result in widely varied spring constants and resonant frequencies. Photolithography allows excellent control over the spring widths and lengths but vertical features such as the spring thickness must be defined using

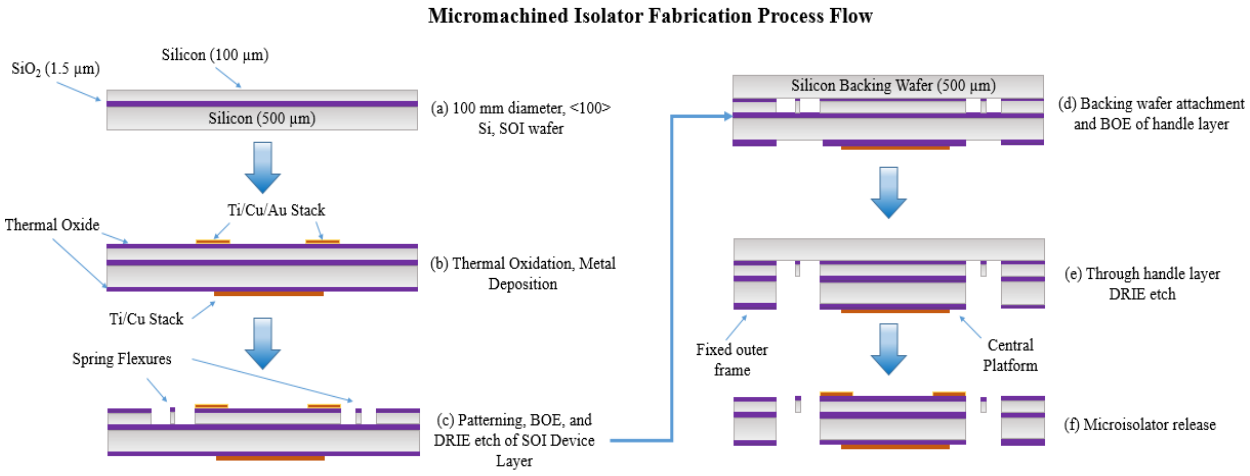

Figure 4.12: Process flow summary for fabrication of silicon micromachined vibration isolators using SOI wafers. Critical material deposition and etch processes are shown in steps (a) through (f).

Si etching. The adoption of SOI wafers as a fabrication substrate mitigates the process variation by utilizing a predefined thickness for the spring flexures.

Figure 4.12 displays the process flow for fabrication of MVIs. A detailed microfabrication process flow is included in Appendix C. Firstly, a one hour wet thermal oxidation is performed to serve as a hard etch mask during DRIE. Next, a Ti/Cu/Au (50/250/20 nm) stack is deposited onto the device layer via electron beam evaporation. This metallization layer defines the electrical readout traces and pads from which output data from an isolated sensor can be probed. An additional electron beam evaporation step can be performed to deposit Ti/Cu (50/250 nm) onto the device handle layer. This additional layer can be used to solder attach microfibrous damping meshes discussed in Chapter 5 as well as metal countermasses.

Next, device layer features are defined via DRIE as shown in Figure 4.12(c). AZ® 9245 positive photoresist by MicroChemicals is spun to 7 μm and exposed to define the spring flexures of the microisolator. This is followed by a timed buffered oxide etch (BOE) to remove the thermally grown oxide layer and allow Si etching. An STS silicon etcher is used for DRIE. Etch and passivation cycles consist of a 13 second etch step using SF_6 at a flow rate of 130 sccm and a 5 second passivation step using C_4F_8 at a volumetric flow rate

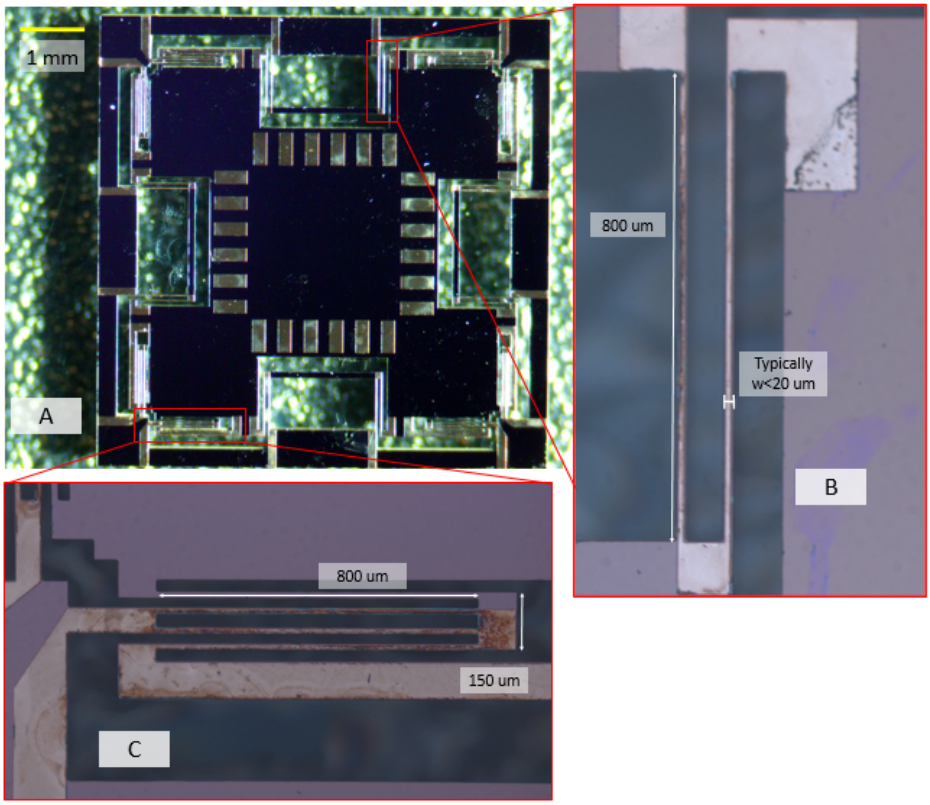

Figure 4.13: Fully Fabricated I2 MVI with metallization traces. (a) Device layer view. (b) Center spring flexure. (c) Corner spring flexures.

of 85 sccm. The power of the 13.56 MHz RF coil is set to 600 W. Typical etch rates are approximately one μm per cycle.

After processing the device layer, the handle layer is patterned and etched. To accommodate a through handle layer etch, a Si backing wafer is attached to the processed wafer's device layer [Figure 4.12(e)]. This prevents wafer cracking during the 500 μm through handle layer etch. During the handle layer etch, the Si beneath the spring flexures is removed to allow displacement under actuation. In I1 and I2 MVI variations without the central platform substrate, the handle layer of the central platform is etched away during this step. All features defined during the device layer processing are etched completely through the wafer during the handle layer etch. Finally, the fully etched microisolators are placed in an acetone bath to allow release from the backing wafer [Fig.4.12(f)].

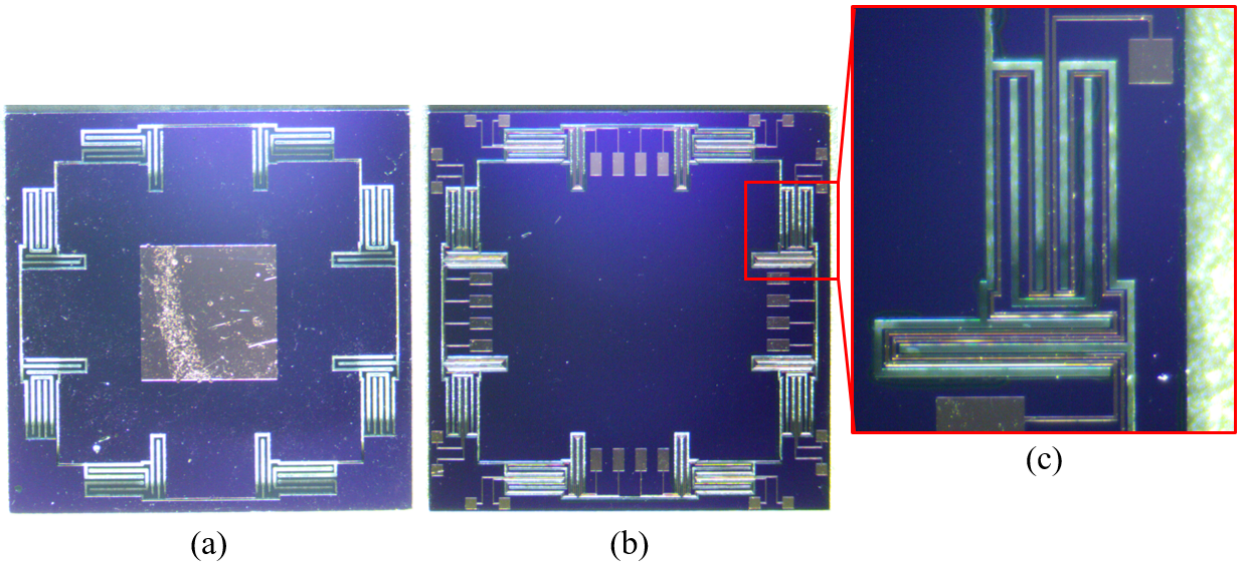

Figure 4.14: Fully Fabricated I3 MVI with metallization traces. (a) Handle layer view showing attachment pad for damper and/or counter mass. (b) Device layer view. (c) Corner spring flexures.

Figure 4.13 displays a fully fabricated I2 MVI. The device layer is shown in Figure 4.13(a). The metallization traces on the device layer central platform and along the spring flexures allow electrical readout of isolated sensor data. Magnified images of the fully released central and corner spring flexures are presented in Figure 4.13(b) and Figure 4.13(c), respectively. Center springs often exhibited widths less than 20 μm due to photolithography and etching tolerances. Note the oxidation present on the metal traces on springs in 4.13(b) and 4.13(c) is eliminated with the addition of a gold layer over the copper. Images in Figure 4.13 were taken prior to adding the 20 nm gold flash to the metal stack.

A fully fabricated I3 MVI is presented in Figure 4.14. The handle layer with added metal trace for solder attachment of microfibrous damper and/or counter mass is displayed in Figure 4.14(a). The MVI device layer is shown in Figure 4.14(b) and corner spring flexures are shown in Figure 4.14(c). Oxidation of metal traces has been mitigated due to inclusion of 20 nm gold flash atop the metal stack.

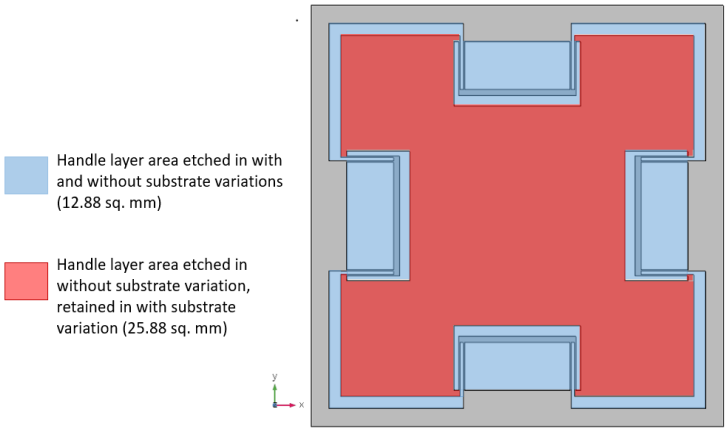

Figure 4.15: I1 handle layer etch areas. Area etched in all substrate variations (blue) and area etched in without substrate variation (red). These large etch areas result in the plasma loading effect in I1, I2 MVIs.

4.2.1 Deep Reactive Ion Etch Considerations

The deep reactive ion etch (DRIE) of silicon is the critical fabrication step which physically defines the microisolator structure. The quality of the DRIE directly affects the quality of the fabricated device. Properly executed DRIE can yield high aspect ratio structures that deviate little from the intended device design, while poorly executed DRIE can result in issues ranging from slightly compromised device dimensions to devices which are unable to be fabricated. Two DRIE issues encountered during the fabrication of MVIs are (1) the plasma loading effect and (2) the emergence of "black" silicon.

The plasma loading effect occurs when areas where Si is to be etched are large enough to deplete the etch gas, SF_6 in this case, such that the etch rate is significantly reduced. The plasma loading effect was first reported by Mogab [79] and experimentally demonstrated by Kartunnen *et al* [80]. The loading effect is considerable in the fabrication of the I1 and I2 MVIs, particularly in variations where the handle layer is etched. The observed etch rate in I1, I2 variations with handle layer substrate was 0.87 μm/cycle while the etch rate dropped to 0.70 μm/cycle when the handle layer was etched away. The Si etch areas on the handle layers for these variations are 12.88 mm^2 per device with handle layer and 38.76 mm^2 per

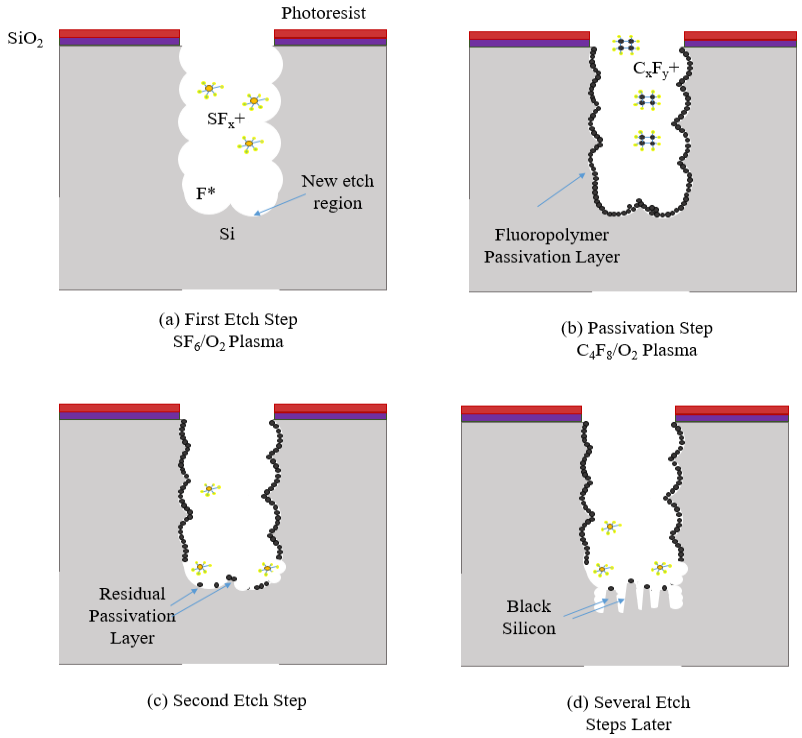

Figure 4.16: Formation of black silicon during DRIE. (a) Silicon etching by fluorine radicals produced by SF_6/O_2 plasma. (b) Fluoropolymer passivation layer formed via radicals produced from C_4F_8/O_2 plasma. (c) Micromasking formation due to residual passivation layer. Oxygen radicals typically bond to the fluoropolymer, removing it allowing for silicon etching. (d) Formation of black silicon results from inability to etch silicon due to residual fluoropolymer layer.

device with handle layer etched. Figure 4.15 demonstrates the difference in etch area in the two variations. I1, I2 devices are fabricated in a 7x7 grid on the SOI substrate such that the total Si etch area on a wafer is 631.12 mm^2 for variations with substrate and 1899.24 mm^2 for variations without substrate. The device layer etch rate was closer to one μm/cycle due to the smaller Si etch area. The plasma loading effect is not observed in the I3 MVI. Significantly less etch area is present in the I3 because only variations with substrates were fabricated and because etch areas were significantly reduced. Etch rates remained consistent during DRIE.

Black silicon, often referred to as "grass", arises when fluoropolymer formed as a passivation layer during the DRIE passivation step is not properly removed during the DRIE

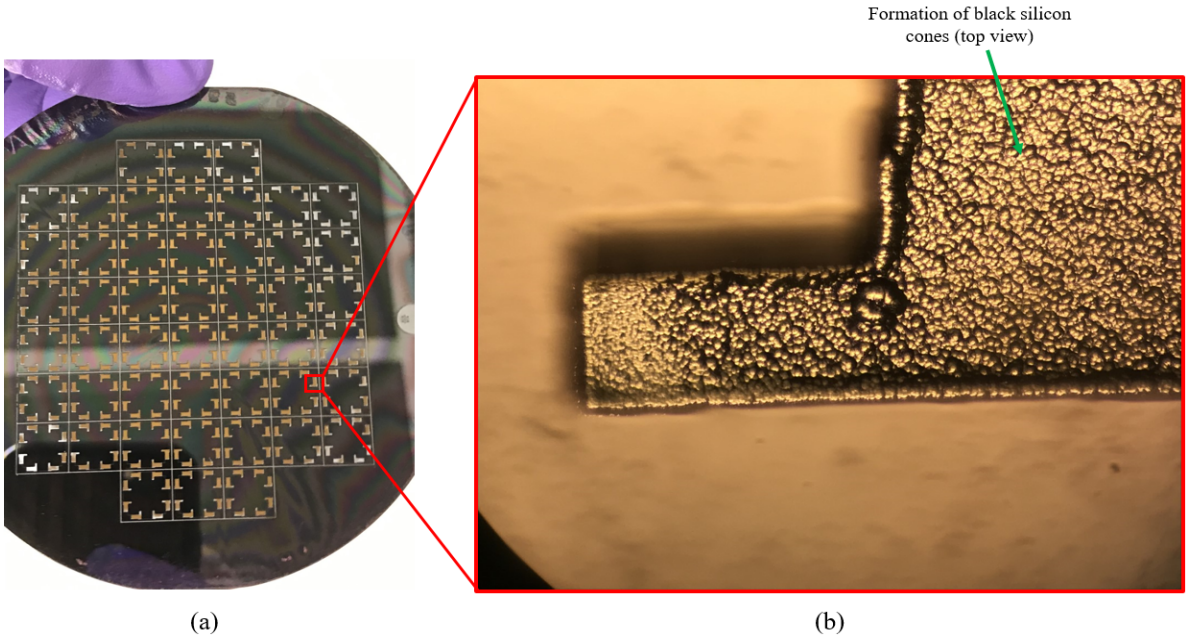

Figure 4.17: Black silicon formation during deep reactive ion etching of wafer handle layer. (a) Full wafer view. Silicon etch areas are yellow-brown instead of grey-silver indicating a transition to black silicon. (b) Enhanced view of etch area. Black silicon "cones" appear as "bubbles" from top view.

etch step [81]. Ideally, the fluoropolymer ($Si_xO_yF_z$) acts to promote anisotropic etching of Si by coating the sidewalls of the etch profile. However, residual fluoropolymer can remain on the etch surface forming a "micromask" which prevents fluorine radicals from etching the masked Si subsrate in subsequent etch steps. This results in the formation of cone or grass-like Si structures that appear black due to their high optical wavelength absorption. Figure 4.16 graphically depicts a possible mechanism by which black silicon can form. Interestingly, a widely used method, the black silicon method, has been employed to maximize DRIE aspect ratios. The black silicon method entails increasing the O_2 flow rate until black silicon is formed. Next, passivation gas flow rate is increased until the black silicon is no longer present. Passivation gas or O_2 can then be adjusted to account for more positively (excess O_2) or negatively (excess passivation gas) tapered sidewalls [82].

During the fabrication of MVIs, the formation of black silicon was mitigated by reducing the DRIE passivation step time from seven seconds to five seconds. Figure 4.17 displays the

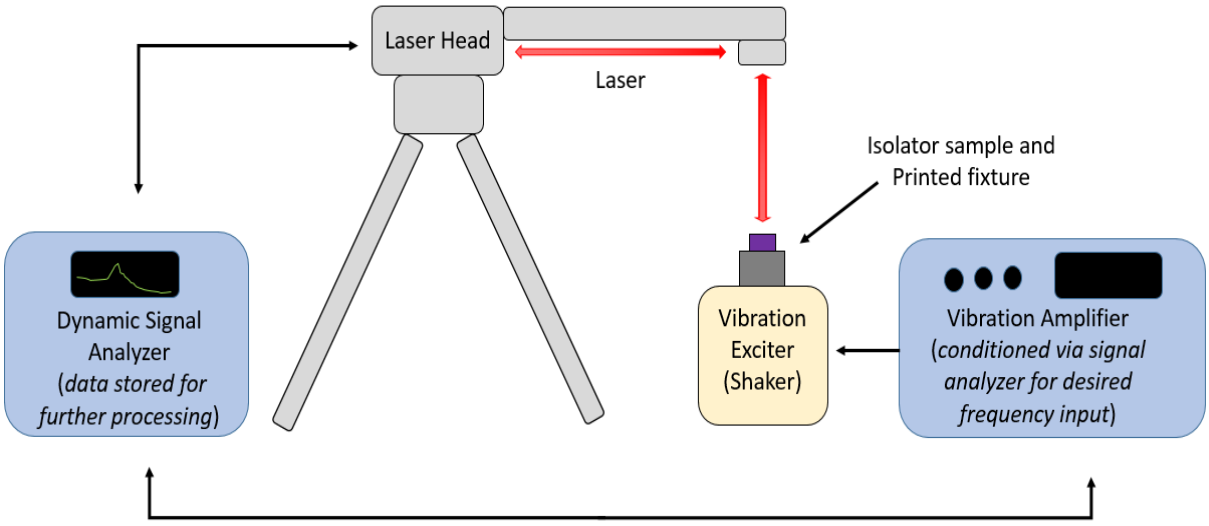

Figure 4.18: Transmissibility testing setup for microisolator frequency response characterization. A mechanical shaker excites the isolator across a 6.2 kHz bandwidth and laser vibrometers measure displacements for given frequencies. Note that two lasers are used during testing: one to measurement the isolator response, another to measure the response of the reference test fixtures.

handle layer of a wafer during DRIE and a magnified etch area in which the silicon is transitioning to black silicon. The bubble-like structures forming on the silicon surface are black silicon cones. Note that true black silicon is not formed because the sidewalls of the cones are not right angles to the silicon surface. Because the cones have sloped sidewalls, the silicon takes on a brown or yellowish tinge as seen in Figure 4.17(a).

4.3 Dynamic Performance of Undamped Micromachined Vibration Isolators

4.3.1 Transmissibility Test Setup of Undamped MVIs

After fabrication each isolator type, the dynamic performance is quantified via experimental testing. Testing involved analyzing the transmissibility of each isolator when excited across a 6.2 kHz bandwidth. The performance of each isolator can be characterized by its quality factor (Q), resonant frequency (f_r), and the attenuation profile within its stopband.

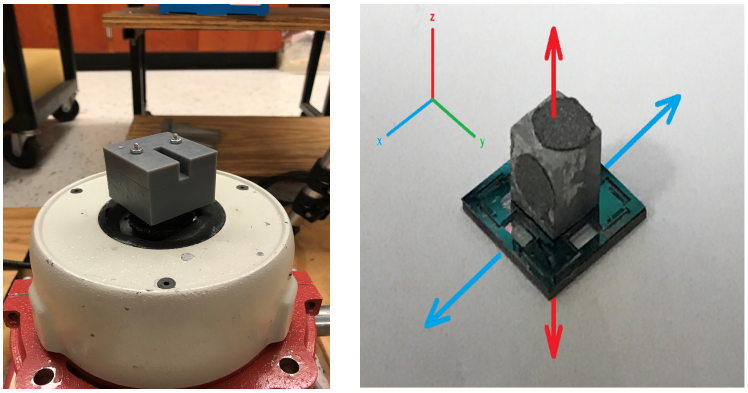

Figure 4.19: (a) 3D-printed test fixture to allow transmissbility testing of microisolators on large mechanical shaker. The DUT is clamped between two separate printed pieces about the isolator's fixed frame. (b) Axis coordinates in reference to isolator/Al test cube combination. Mechanical shaker actuates in the z-axis direction.

Acquiring the transmissibility consists of exciting the microisolator with mechanical vibration and studying its response. The vibration was applied via a mechanical shaker and can be described as random noise across a 400 to 6600 Hz bandwidth. The response is the relative displacement of the isolator's central platform to the excited base on which the isolator is affixed. The displacement ratio of the central platform to excited base across the bandwidth yields the transmissibility of the isolator. Laser Doppler vibrometry is used to measure the displacements. Reflective tape is applied to the platform and base to allow measurements to be taken by lasers (laser sensitivity was set to 20 μm/V). Figure 4.18 displays a simplified diagram of the testing setup. Note that only one laser emitter is shown for simplicity, yet two lasers are required in the actual testing setup (isolator response laser and reference laser). The output signal for each laser emitter was fed into a dynamic signal analyzer. The analyzer serves to pair the measured displacements with their corresponding excitation frequency. The analyzer was also used to condition the output of the vibration amplifier and mechanical shaker.

The mechanical shaker is a rather large and cumbersome piece of equipment. There is a stark contrast in size between it and the microisolator that it is intended to excite. In order to test the isolator on the shaker, a test fixture is fabricated to house the device-under-test

(DUT) [Figure 4.19(a)]. The test fixture was 3D-printed and made of a UV-curable photopolymer. The fixture is composed of two separate pieces which clamp together to hold the isolator fixed. A 500 μm wide rim around the perimeter of a square cavity in the test fixture allows the isolator to be clamped about its fixed frame while providing sway space for the central mass to oscillate. A 110 mg aluminum cube is attached to the isolator to emulate the mass of a sensor [4.19(b)]. The complete isolator/fixture configuration is presented in Figure 4.20.

The transmissibility test was conducted for each isolator variation. As mentioned before, testing consisted of measuring the response of the isolators across the 400 to 6600 Hz bandwidth. Note that excitation and measurements were performed along the z-axis. The analyzer was instructed to sweep across the bandwidth. The responses were compiled to form the transmissibility profile of that sweep. Sweeping was performed 500 times and the

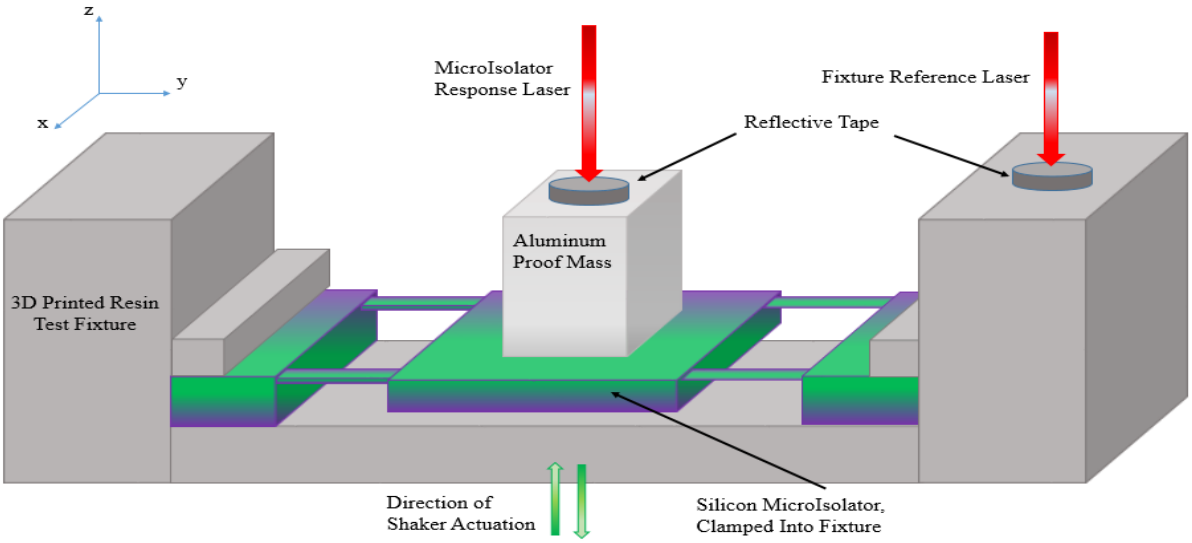

Figure 4.20: Transmissibility testing setup for microisolator frequency response characterization. A mechanical shaker excites the isolator across a 6.2 kHz bandwidth and laser vibrometers measure displacements for given frequencies. Note that two lasers are used during testing: one to measurement the isolator response, another to measure the response of the reference test fixtures.

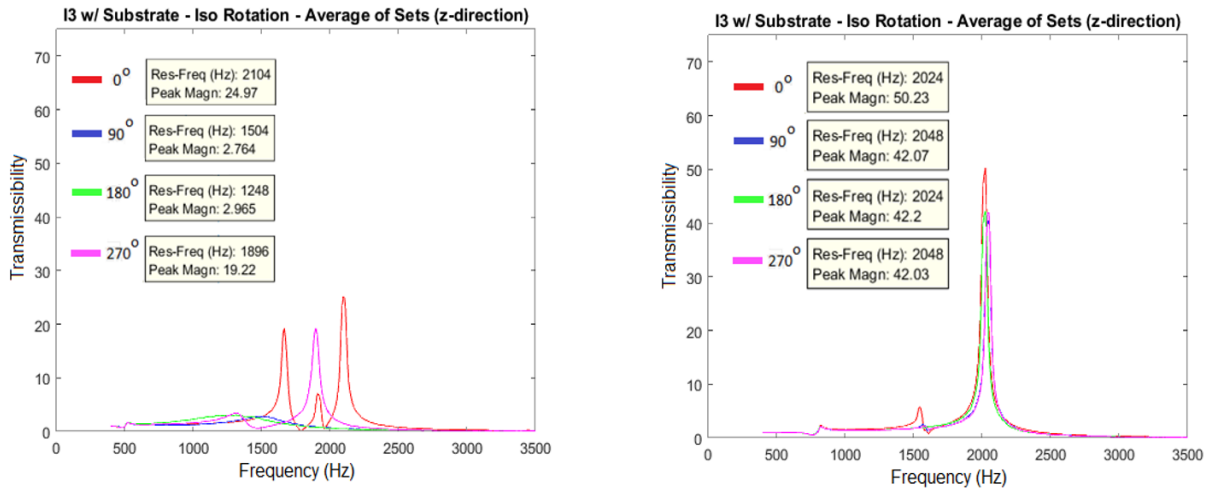

(a) (b)

Figure 4.21: Comparison of transmissibility uniformity after z-axis rotation. (a) Machined plexiglass fixture displays variation in resonant frequency from 1.248 kHz to 2.104 kHz and Q from 2.965 to 24.97. (b) Printed resin fixture shows much more consistent results. Only a 24 Hz range in resonant frequency is exhibited. Variation in Q is just 8.2.

transmissibility sample for each sweep was collected and averaged into a single transmissibility test set. Each isolator variation was subjected to a minimum of 5 test sets resulting in a minimum of 2500 transmissibility samples per excitation frequency.

To ensure consistency and repeatability while testing, the isolators were periodically rotated 90° in the test fixture. This served to ensure that measured z-axis displacements were rotationally symmetric. Originally, we utilized a machined plexiglass fixture which exhibited poor rotational uniformity. Measured Qs and f_rs varied wildly when a tested device was rotated 90°. However, the introduction of the 3D-printed resin fixture provided significantly more uniform responses. Figure 4.21 displays a comparison of the response of an isolator rotated in 90° intervals in (a) original plexiglass fixture and (b) 3D printed fixture.

4.3.2 Transmissibility Test Equipment

The test equipment used for MVI transmissibility testing is displayed in Figure 4.22. An HP35655A dynamic signal analyzer [Fig. 4.22(a)] is used to set testing parameters including

Figure 4.22: Test equipment used for during transmissibility analysis of fabricated MVIs.

frequency range, sample resolution, and number of recorded samples. Additionally, the analyzer sets output parameters excitation type (random noise, sinusoidal, chirp, etc.) and excitation level for the PA500L power amplifier by Ling Dynamic Systems [Fig. 4.22(b)]. The power amplifier excites a V408 electrodynamic shaker also from Ling Dynamic Systems [Fig. 4.22(c)] which actuates the device under study.

Displacement measurements are made using two Polytec OFV 353 laser vibrometer sensors/emitters [4.22(d)] which measure displacement of the device under study using laser Doppler vibrometry. Polytec OFV 2610 [4.22(e)] laser controllers are used to set the sensitivity of the laser in μm/V.

4.3.3 I1 Undamped Dynamic Performance

The I1 isolator variation without substrate experimentally demonstrated a resonant frequency of 1.344 kHz, a 6.4% deviation from the 1.43 kHz resonant mode observed in simulation. I1 w/o substrate exhibits a peak transmissibility of 30.39 as shown in Figure 4.23(a). To characterize the stopband attenuation, the -20 dB or 0.1 transmissibility frequency, f_{-20dB} is considered. At this frequency the output displacement has dropped to just 10% of the input. I1 w/o substrate demonstrates f_{-20dB} at 2.84 kHz as indicated in Figure 4.23(b).

I1 w/ substrate exhibits f_r at 1.312 kHz with a Q of 16.7 as shown in Figure 4.23 (c). Percent difference between the simulated (1.41 kHz) and experimental f_r is 7.47%. Notably, the secondary mode exhibits a transmissibility which exceeds unity just before 4 kHz. The f_{-20dB} point appears at just 1.65 kHz indicating excellent attenuation in the stopband until the peak before 4 kHz as shown in the logarithmic plot in Figure 4.23(d).

Both of the I1 MVI variations exhibit undesirable resonant modes before the primary out-of-plane resonant mode. Interestingly, the I1 w/ substrate exhibits a vibration band gap before 2 kHz.

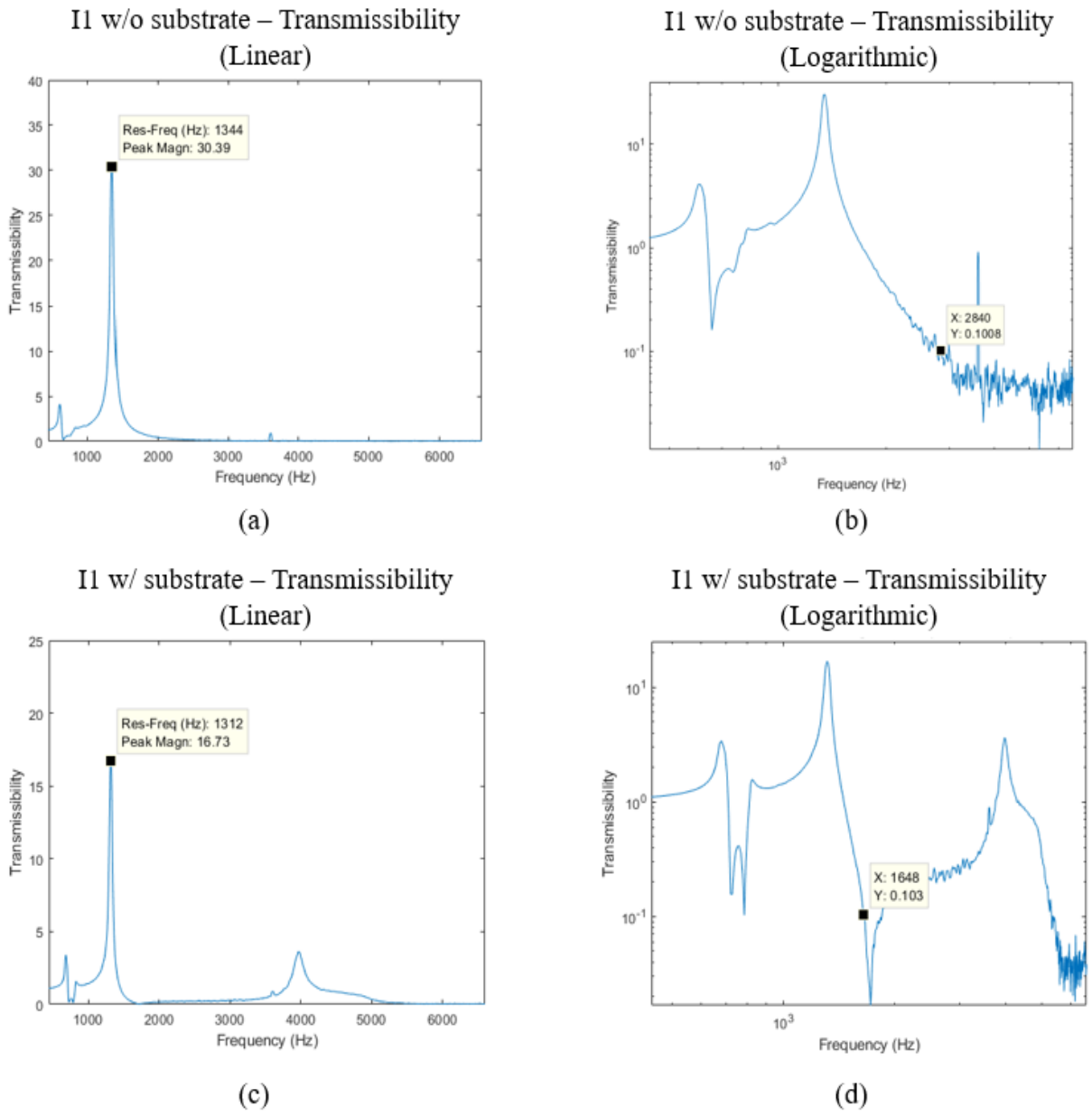

Figure 4.23: I1 MVI transmissibility profiles. I1 w/o substrate (a) linear and (b) logarithmic. I1 w/ substrate (c) linear and (d) logarithmic.

4.3.4 I2 Undamped Dynamic Performance

I2 isolators without substrate exhibit a Q of 38.2 at a f_r of 1.776 kHz. The percent difference between the experimentally observed and simulated (1.887 kHz) f_r is 6.25%. Stopband attenuation in I2 is not as rapid as in I1, with f_{-20dB} at 3.52 kHz. I2's transmissibility profile can be seen in Figure 4.24 (a) and (b).

I2 w/ substrate exhibits f_r at 2.009 kHz with a Q of 59.89. The percent difference between the simulated (2.50 kHz) and experimental f_r was found to be 19.64%. Stopband attenuation in I2 occurs at a higher frequency than I1, with f_{-20dB} approximately 4.67 kHz. The I2's transmissibility profile can be seen in Figure 4.24 (c) and (d).

Both the I2 variations exhibit the undesired resonance before the primary resonance observed in the I1 variations.

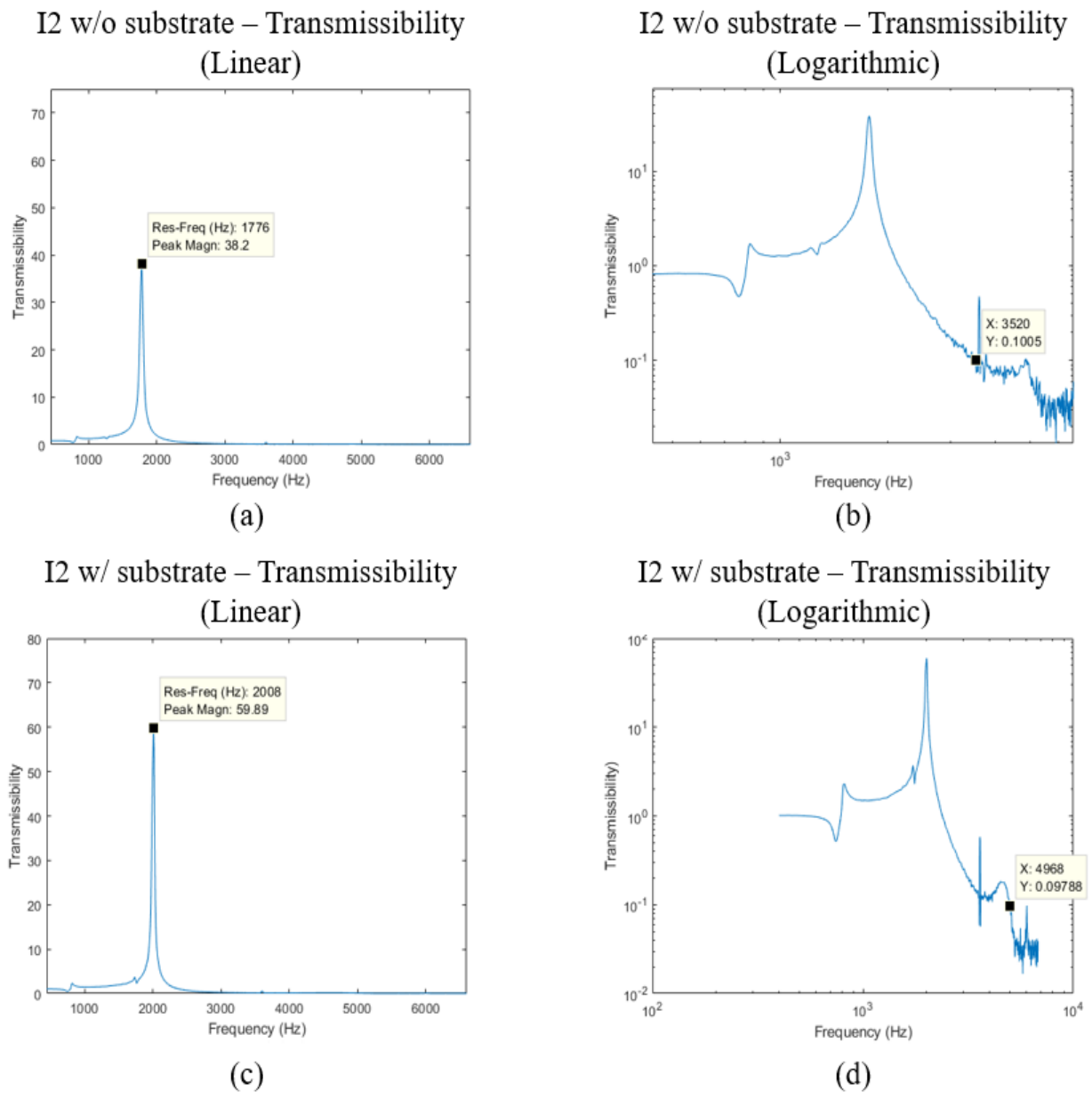

Figure 4.24: I2 MVI transmissibility profiles. I2 w/o substrate (a) linear and (b) logarithmic. I2 w/ substrate (c) linear and (d) logarithmic.

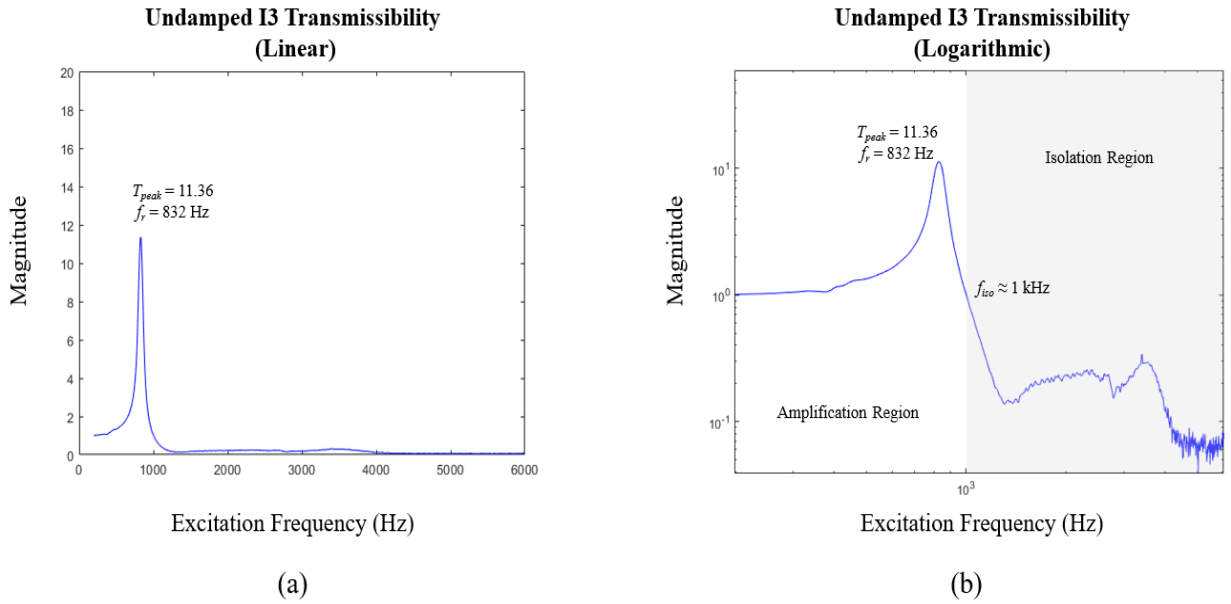

Figure 4.25: I3 MVI undamped transmissibility profile (a) linear and (b) logarithmic.

4.3.5 I3 Undamped Dynamic Performance

The undamped I3 transmissibility is shown in Figure 4.25 which presents the average transmissibility profile of 8000 samples at each frequency step (Δf = 8 Hz) between 400 Hz and 6600 Hz. The experimentally observed peak transmissibility, T_{peak}, is 11.36. This corresponds to an undamped effective damping ratio of $\zeta_{ud} = 0.044$. The resonant frequency determined by experiment (832 Hz) matches well with the resonant frequency derived analytically (850 Hz) and from FEA simulation (844 Hz). The undamped isolation region, f_{iso}, begins right at 1 kHz. Resonances in the isolation region are present from 1300 to 3500 Hz where there is a notable excitation peak. This peak is thought to be an artifact of the test setup as it is present in tests of other devices.

Table 4.3: Undamped MicroIsolator Performance Summary

Isolator Variation	f_r **(FEA, kHz)**	f_r **(Exp, kHz)**	**Quality Factor**	f_{-20dB} **(kHz)**
I1 w/ sub.	1.41	1.312	16.7	1.65
I1 w/o sub.	1.43	1.344	30.39	2.84
I2 w/ sub.	2.50	2.01	59.89	4.67
I2 w/o sub.	1.887	1.796	38.2	3.52
I3	0.844	0.850	11.36	4.712

4.3.6 Undamped Dynamic Performance Summary

A summary of the undamped dynamic performance of the MVI variations is given in Table 4.3. FEA and experimental results for fundamental resonant frequencies are in good agreement. However, measured quality factors indicate significantly increased induced acceleration sensitivity near the MVI's resonant frequency. To mitigate this added acceleration sensitivity at resonance, damping must be added to reduce the system quality factor. Chapter 5 provides an overview of previously used techniques to increase MVI damping and it details the novel use of microfibrous meshes and polymers to increase system damping.

4.4 Reliability Studies on the Undamped I3 MVI

4.4.1 Finite Element Study of Peak Von Mises Stress Under Harmonic Acceleration

An FEA study using COMSOL Mulitphysics is performed to determine the peak Von Mises stress exhibited by the I3 MVI under harmonic acceleration magnitudes ranging from 1 G to 100,00 G. In yield analysis, the Von Mises (VM) stress is often compared to the yield strength (for ductile materials) of a material to estimate whether or not a material will plastically deform [83]. If the computed VM stress exceeds the material yield strength, plastic deformation is predicted. Because single-crystal silicon (SCS) is a brittle, not ductile, material, the simulated VM stresses are compared to the ultimate tensile strength (UTS) of SCS (brittle materials do not exhibit plastic deformation like ductile materials). The UTS is

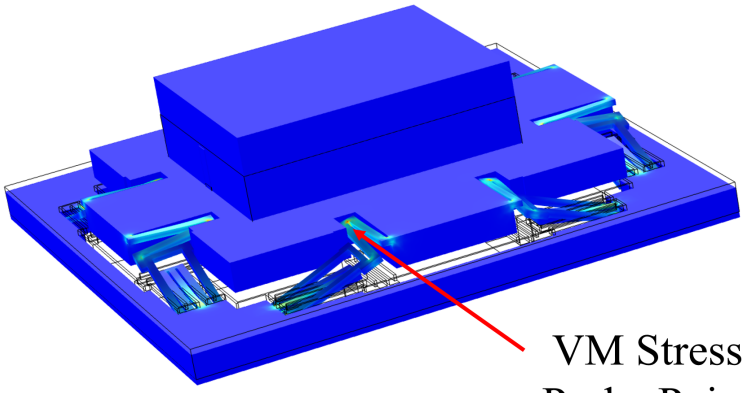

Figure 4.26: Probe point on I3 MVI for peak Von Mises stress simulation for acceleration magnitudes from 1 G to 100,000 G's. The probe point is located on the spring flexures (Spring Element 3 as shown in Figure 4.4).

the maximum stress the material can endure before fracture. In brittle materials, the yield strength and UTS are very similar. In [3], Petersen lists the UTS of SCS at 7 GPa.

Figure 4.26 shows the probe point at which the VM stress is measured during simulation. This point is the point of peak VM stress during excitation of the primary resonant mode. To excite the isolator, a harmonic acceleration boundary condition in the out-of-plane direction is applied to the bottom surface of the MVI outer frame with magnitudes ranging from 1 to 100,000 G's. The acceleration magnitudes are applied across an excitation bandwidth from 400 to 6600 Hz.

Figure 4.27 displays the results of the FEA study. The VM stress at the probe point is plotted across the excitation bandwidth for each of the acceleration magnitudes and compared to the UTS of SCS (dashed red line). Significant VM stress peaks occur at both the primary out-of-plane resonant mode and the second and third rotational modes. Simulation results suggest that acceleration magnitudes of 100 G's and greater result in peak VM stresses exceeding the UTS of SCS when the I3 is undamped.

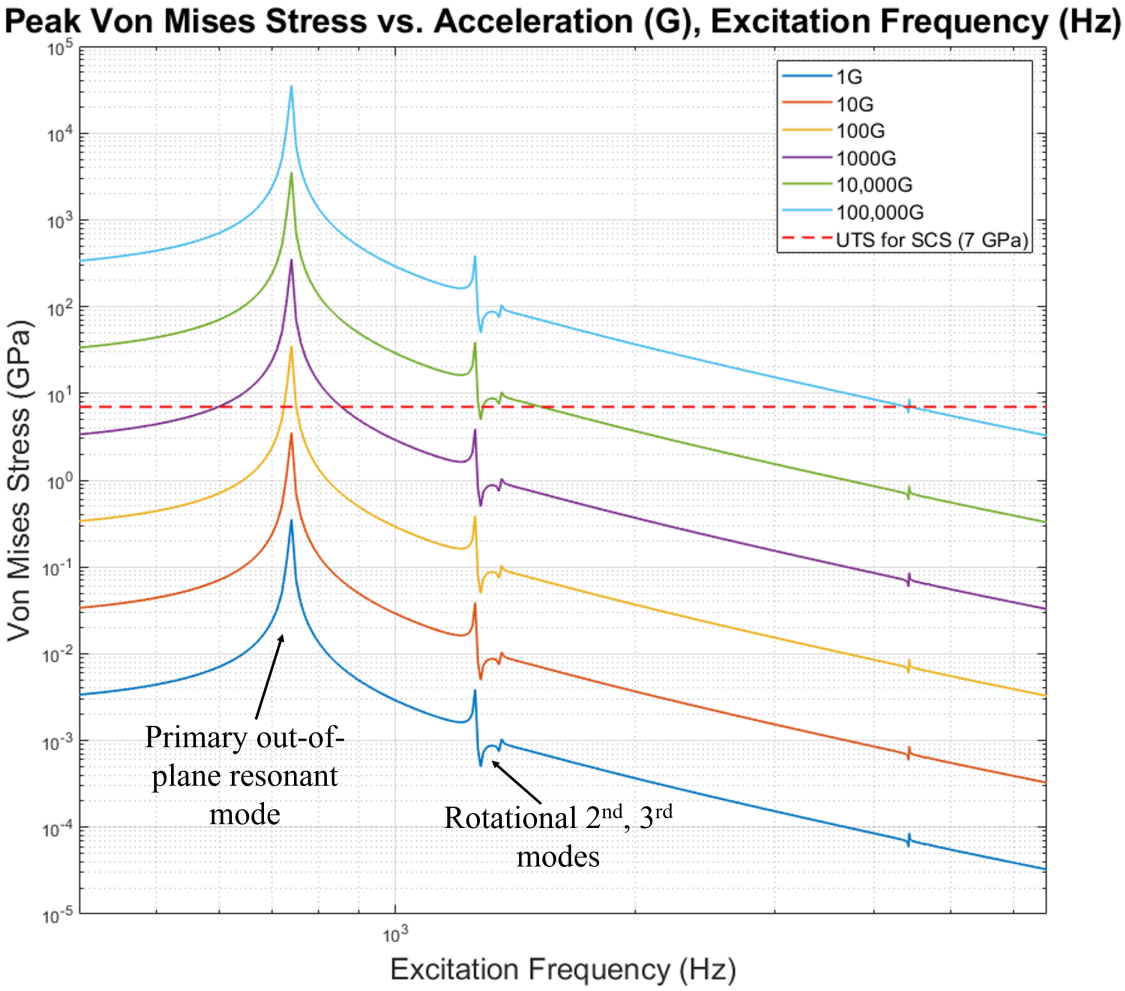

Figure 4.27: Peak Von Mises stress on I3 MVI under acceleration magnitudes ranging from 1 to 100,000 G across a 400 to 6600 Hz bandwidth. VM stress peaks are present at the primary resonant mode as well as at the second and third rotational modes.

4.4.2 72 Hour Vibration Testing

The reliability of the I3 MVI is experimentally tested via a 72 hour vibration test. The isolator is subjected to random noise vibration for 72 Hours using the testing setup described in Section 4.3.1 and the transmissibility is sampled every 12 hours for a total of seven samples. The recorded transmissibility profile for each of the seven samples is plotted in Figure 4.28.

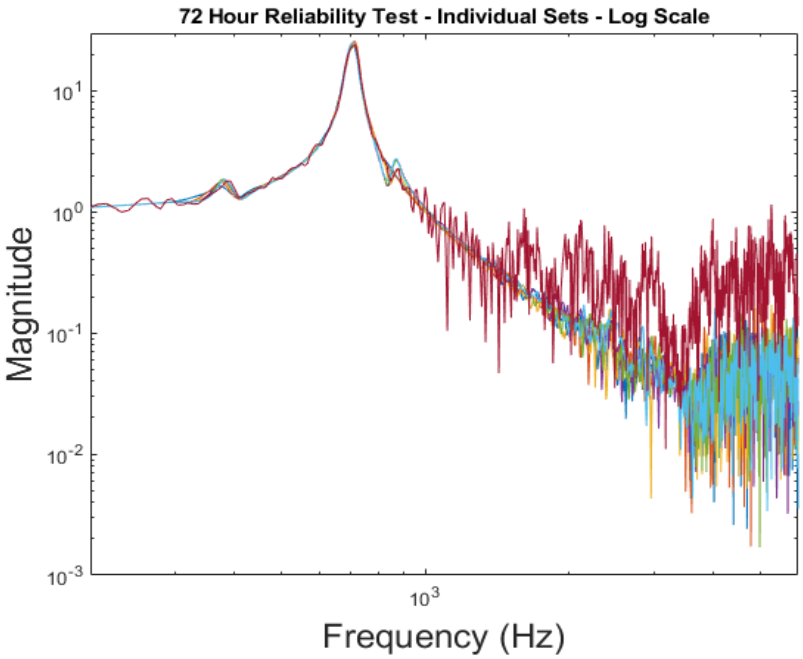

Figure 4.28: Individual transmissibility profiles for 72 hour undamped I3 reliability test. Seven transmissibility samples are taken at 12 hour intervals to monitor change in the performance over time.

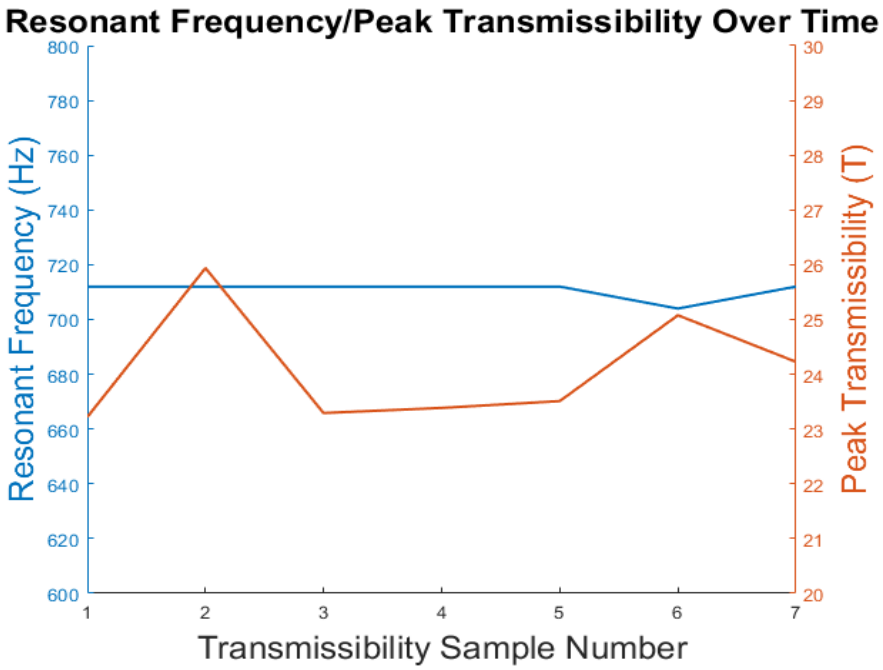

Figure 4.29: Peak transmissibility and resonant frequency of each sample for 72 hour undamped I3 MVI reliability test.

The peak transmissibility and resonant frequency for each of the seven samples is plotted in Figure 4.29. The undamped isolator exhibits very consistent performance throughout the reliability test. The resonant frequency stays consistently at 712 Hz except for a single sample (Sample 6) at 704 Hz. The measured T_{peaks}s range from 23.22 to 25.94, just a difference of 2.72.

4.5 Alternative Fabrication Technologies for MVIs

4.5.1 Additive Manufacturing

An alternative fabrication method for MVIs is available using additive manufacturing. Additive manufacturing, or 3D printing, was first described in 1986 by Hull [84] and is considered "the process of joining materials to make objects from 3D model data, usually layer by layer" [85], [86]. Select 3D printing technologies include fused deposition modeling (FDM), selective laser sintering (SLS), inkjet printing, stereolithography (SLA), and 3D plotting. FDM printing is the most common printing paradigm of polymer-based materials. It consists of heating a thermoplastic filament to its melting point and extruding the melted filament layer by layer to construct the desired 3D object. SLS printing operates by the selective sintering of powder using a high power laser. SLA printing uses photopolymers that are cured by a UV laser. The photopolymers are in the form of a liquid resin which polymerize after exposure to the UV laser. This polymerization is carried out one layer at a time such that each 2D polymerization layer is added atop the previous layer of polymerization to produce a finished 3D object [86].

Since the conception of 3D printing, there has been a significant increase in the available materials which can be printed as well as significant improvement in the resolution at which features can be printed. Resolution as high as 10 μm is now achievable using SLA printing [86]. Such improvements in the resolution of additively manufactured devices along with their quick fabrication and turnaround times make them increasingly interesting candidates for rapid prototyping and even finished product applications of micromechanical devices. Unlike

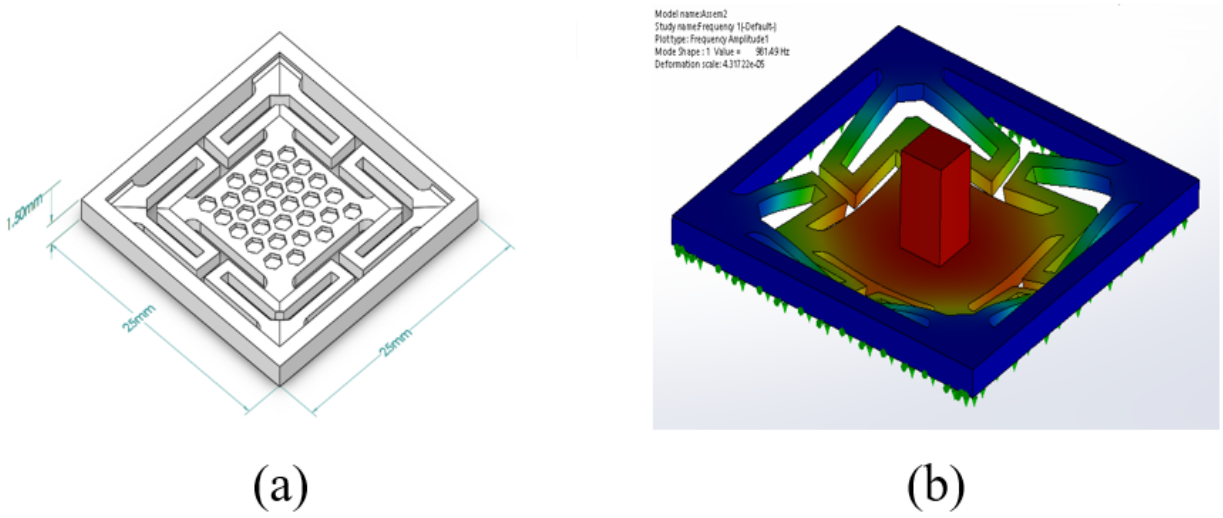

Figure 4.30: CAD Model of 3D printed MVI. (a) CAD model of printed MVI design dimensions. The X,Y lengths are 25 mm x 25 mm with a thickness of 1.5 mm. (b) FEA simulated primary resonant mode.

traditional MEMS devices, 3D printed devices do not require expensive lithography, etching, and thin-film deposition tools for fabrication. Sections 4.5.2 and 4.5.3 detail the use of FDM and SLA printing to produce microscale vibration isolators. The isolation performance of the 3D printed MVIs is then tested and compared [87].

4.5.2 Design and FEA Modeling of Additively Manufactured MVIs

To investigate the use of additive manufacturing for MVI prototyping, a 25 mm x 25 mm x 1.5 mm MVI was designed using CAD software [Fig. 4.30(a)]. The MVI was designed to exhibit a primary resonant frequency of approximately 1 kHz when loaded with a 110 mg proof mass.

Modal FEA analysis was performed using the material parameters from FormLabs' Grey Resin 1 (FLGPGR04) [88] to estimate the primary resonant frequency. The simulated resonant frequency was 982 Hz, just a 1.8% difference from the desired resonant frequency. Figure 4.30(b) displays the simulated primary resonant mode.

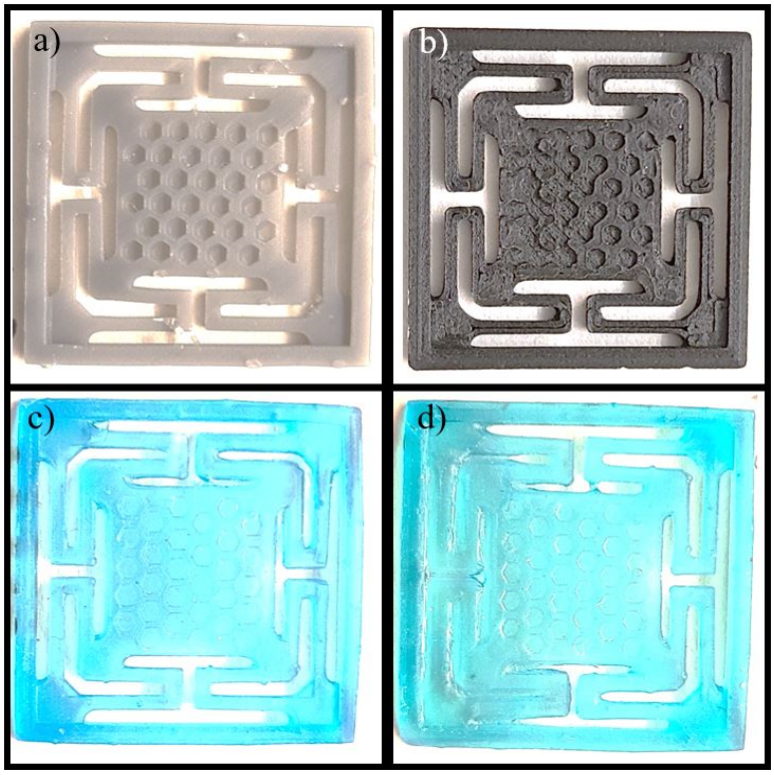

Figure 4.31: Additively Manufactured Vibration Isolators. Isolators printed with: (a) Formlab's Grey Resin. (b) Markforged's Onyx Material. (c) Formlab's Tough Resin. (d) Formlab's Tough Resin with poor print quality and defects.

4.5.3 Fabrication and Testing of Additively Manufactured MVIs

The designed MVI is printed using both FDM and SLA methods. In total 25 isolators were printed. The printed isolators are displayed in Figure 4.31. The MVIs were printed using three different materials: Markforged's Onyx (FDM, 10 total isolators), Formlab's Grey Resin (SLA, 5 total isolators), and Formlab's Tough Resin (SLA, 10 total isolators).

The transmissibilities of the fabricated isolators were tested using the laser doppler vibrometry setup detailed in Section 4.3.1 with a 110 mg Al proof mass added to the isolators' central platform. Transmissibility results for each of the FDM printed Onyx material isolators are shown in Figure 4.32. Isolators exhibited resonant frequencies of about 900 Hz and less variation in Q than in either of the SLA printed materials.

The transmissibilities of each of the five SLA printed Formlabs' Grey Resin vibration isolators are shown in Figure 4.33. Grey Resin isolators exhibited a very consistent resonant

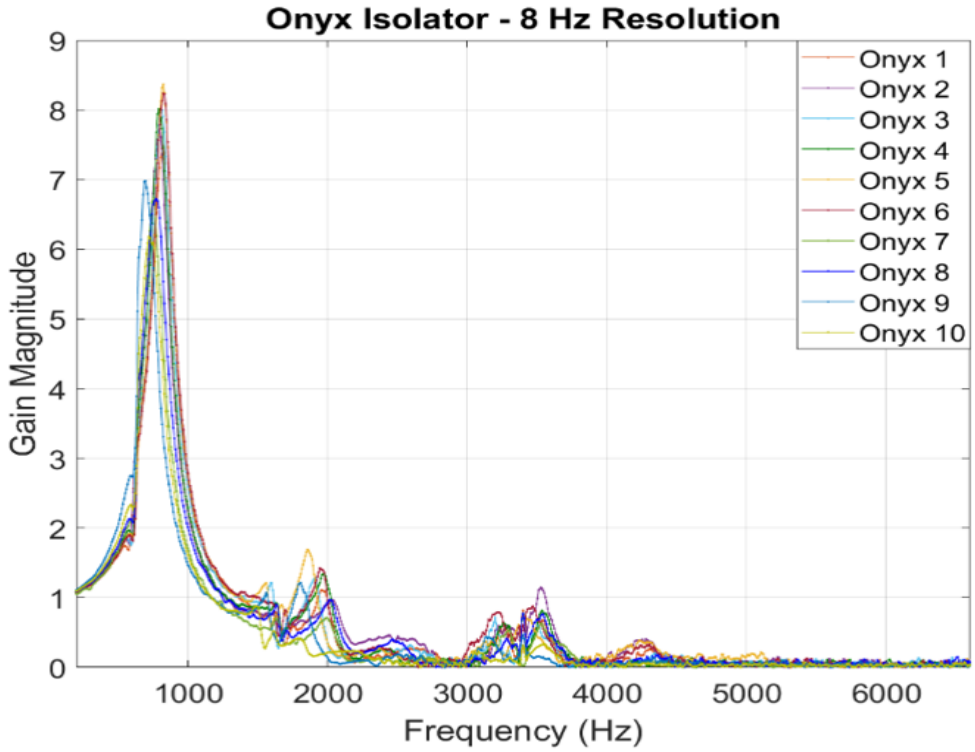

Figure 4.32: Transmissibility of FDM printed Markforged Onyx vibration isolator

frequency of nearly 1 kHz with slightly greater variation in Q than the Onyx isolators. Quality factors ranged from approximately 12 to 19.

Figure 4.34 displays the transmissibilities for each of the SLA printed Tough Resin vibration isolators. The Tough Resin vibration isolators exhibit the greatest variation in resonant frequency of the three materials. The measured quality factors range from approximately 11 to 14.

In summary, the 3D printed vibration isolators exhibit similar experimental resonant frequencies to the resonance indicated in FEA simulation. Interestingly, significant variation in the reliability and consistency of the isolator performance is observed in each of the three tested materials. The FDM printed Onyx isolators exhibit high reliability in both resonant frequency and quality factor. Both of the SLA printed vibration isolators exhibit considerable variation in either resonant frequency (Tough Resin) or quality factor (Grey Resin).

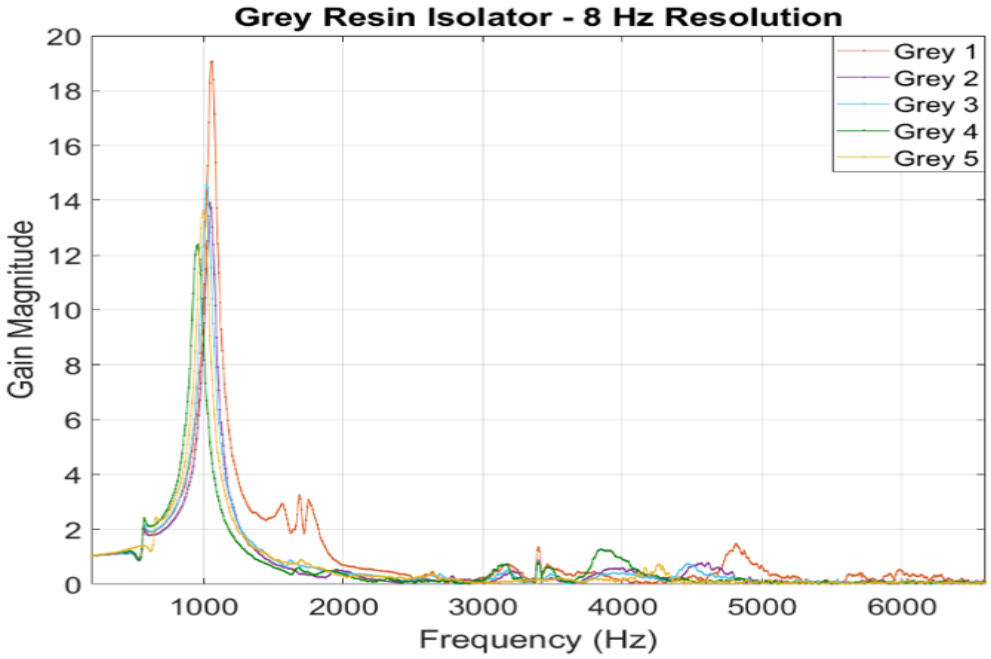

Figure 4.33: Transmissibility of SLA printed Grey Resin vibration isolator

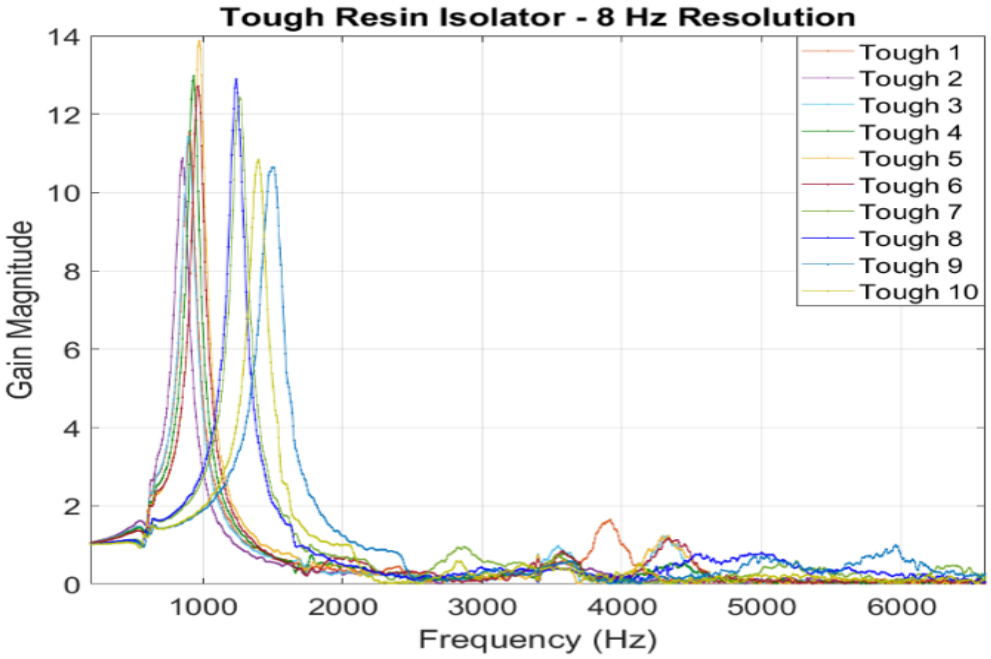

Figure 4.34: Transmissibility of SLA printed Tough Resin vibration isolator.

Further development of 3D printed MVIs will require a number of advancements including a reliable means of adding conductive traces for data acquisition from isolated sensors.

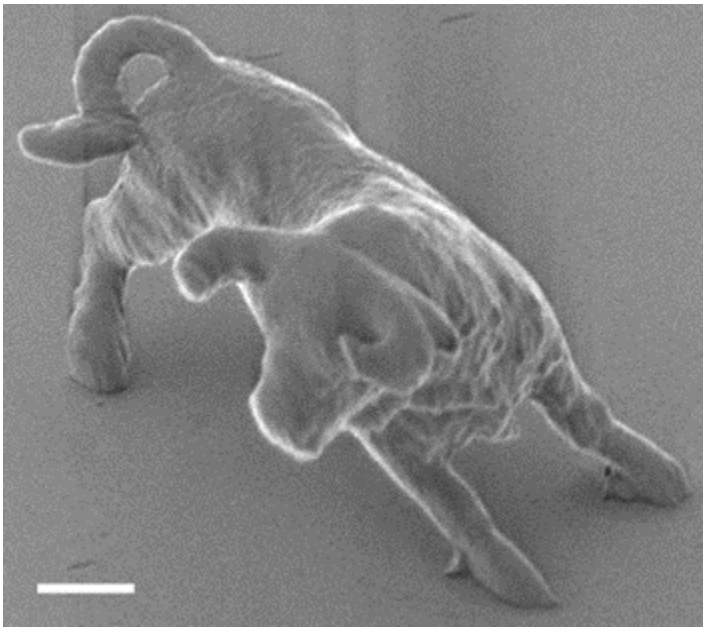

Figure 4.35: Microbull printed using TPP. Scale bar is 2 μm. From Kawata [96].

Another concern is the temperature-dependent mechanical properties exhibited by polymers used in additive manufacturing that may be altered during typical electronics packaging procedures like reflow soldering.

Recently, conductive nanomaterials such as metal nanoparticles, metal nanowires, graphene, carbon nanotubes, and conductive polymers have emerged as a means of applying conductive traces to 2D and 3D printed devices [89]. Such advancements may provide a means of applying electrical traces to 3D-printed vibration isolators.

4.5.4 Two-Photon Polymerization: A Possible Path to Nano-Scale Mechanical Isolation

Two-photon polymerization (TPP) refers to the microscale stereolithography technique first presented by Maruo in 1997 in which a photosensitive material, typically in the form of a resin composed of a photoinitiator and constituent monomers, is selectively exposed to a laser of a particular wavelength in order to selectively polymerize regions of the resin [90]. The polymerization requires two-photon excitation of a photoinitiator for an electron

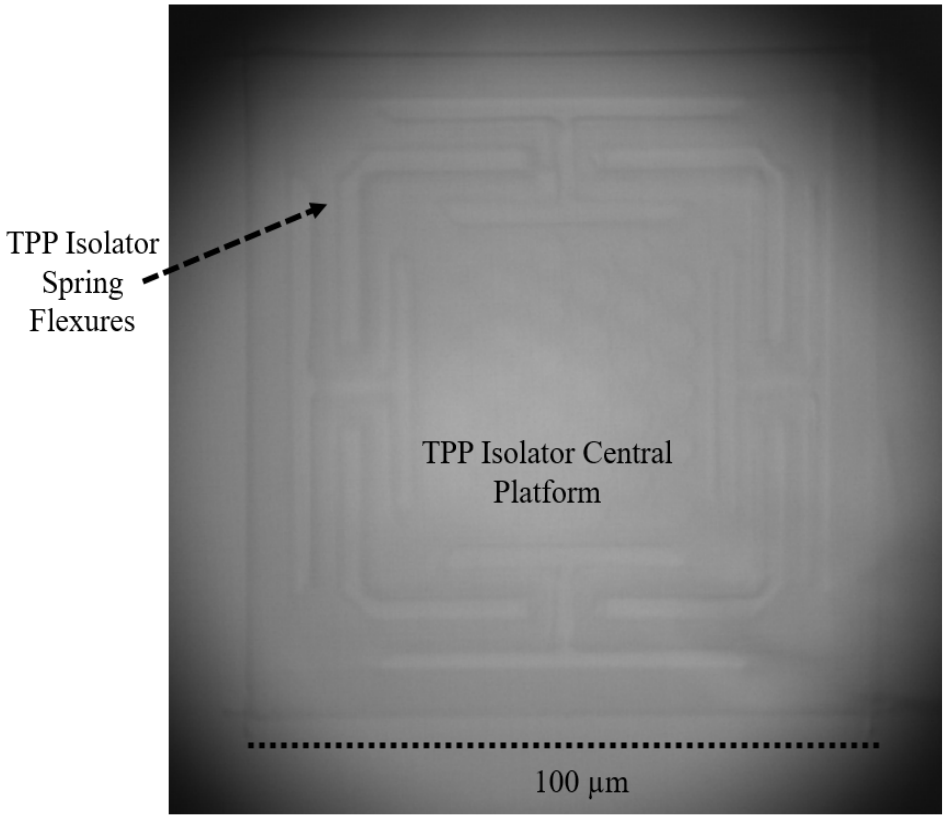

Figure 4.36: Vibration isolator fabricated using two photon polymerization.

to move from an occupied state to a higher energy state [91]. Excellent resolution has been demonstrated using TPP. Resolution is typically *less than* the wavelength of the excitation laser used and resolutions less than 50 nm have been demonstrated [92].

Given the excellent resolution available using TPP as well as the three dimensional control of the polymerization process, TPP has been used in an increasing number of micromachining applications. These advantages have generated interest in mechanical devices printed using TPP [93], [94], [95]. Such advantages may make TPP a candidate process for the fabrication of nanoscale vibration isolation systems.

While TPP does exhibit some of the drawbacks of 3D-printed vibration isolators such as serial fabrication and poor compatibility with existing microfabrication techniques, methods have been developed for selective metallization of TPP structures [97], [98].

An additional mechanical advantage of TPP polymers is their significantly lower elastic moduli (E). Many of these polymers exhibit E's around 1 GPa [99], about 130 times lower than the E of <100> Si. This low E allows the designed TPP isolator to retain a much lower resonant frequency ($\sqrt{130} = 11.4$ times lower) than a Si isolator given the same dimensions.

Figure 4.36 shows a 100 μm by 100 μm variation of the vibration isolator detailed in Sections 4.5.2 and 4.5.3. The isolator was fabricated via TPP using a 520 nm femtosecond-pulse laser.

Chapter 5

Damping Techniques for Shock Reliability

As noted in Section 3.2, increased damping is required to reduce the added acceleration sensitivity induced by MVI resonance. Two previously studied damping methods are the use of heavy gases and the use of electrostatic feedback control. In [100] Kim *et al* investigate the effects of varying gas pressure on the transmissibility of a vibrating MEMS structure. Gas chemistries including SF_6, N_2, SO_2, water vapor, and air were evaluated for their damping performance at pressures ranging from 0.1 Torr to ambient. While heavier gases did exhibit greater damping (SF_6 reduced Q from 150.2 at 0.2 Torr to 15.7 at 540 Torr), the Q's exhibited by the MEMS structure are still large and correspond to significantly increased acceleration sensitivity.

Using electrostatic feedback control Kim *et al* reduce the Q of a vibrating MEMS device from approximately 135 to approximately 60 at a pressure of 50 mTorr [101]. A parallel-plate capacitor is formed by the device and a PCB upon which the device is mounted. The relative velocity of the device to the PCB is sensed via the capacitor using Dean's method detailed in [102]. The measured velocity is then compared to a reference as control input. As in the case of heavy gas damping, the Q's exhibited by the measured device can induce high acceleration sensitivity in an isolated device. Additionally, implementing these damping techniques requires significant added packaging and fabrication complexity. Thus, alternative methods of damping MVIs are needed. The remainder of this chapter discusses the use of microfibrous meshes (Section 5.1) and polymers (Section 5.2) to damp MVI dynamic response [103], [104].

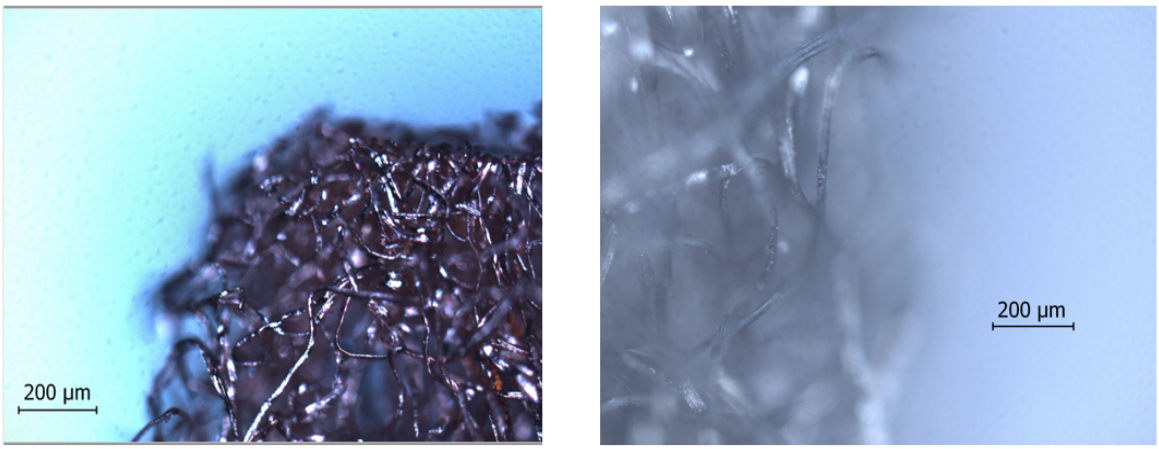

Figure 5.1: Enhanced view of microfibrous meshes for isolator damping. (a) Microfibrous copper mesh. (b) Microfibrous nickel mesh.

5.1 Microfibrous Mesh Damping

As an alternative to using electrostatic actuation and heavy gases for the damping of microisolators, microfibrous meshes (MFMs) are used to contribute damping to the MVI. The use of MFMs reduces the fabrication complexity relative to electrostatic damping and does not require the vacuum packaging environment needed for heavy gas damping. Instead, the mesh can be integrated into the microisolator configuration through a solder attachment step. In this work, the damping performance of both Ni and Cu MFMs is explored. Figure 5.2 shows a microscopic image of both the Cu (Figure 5.2(a)) and the Ni (Figure 5.2(b)) MFMs. The primary damping mechanism by which the microfibrous meshes dissipate energy is through frictional contact between adjacent microfibers. Friction between fibers results in the dissipation of energy as heat throughout the mesh.

The MFMs are fabricated through a traditional wet lay-up paper processing technique in which preformed rolls of micron diameter metal fibers (Ni, Cu, stainless steel, etc.) are combined with cellulose fibers. A subsequent high temperature hydrogen sintering step removes the cellulose fibers and results in binding of the metal fibers at their respective

(a) (b)

Figure 5.2: Microfibrous mesh sheets from which samples are cut. Thickness of sheets is 2 mm. (a) Microfibrous copper mesh sheet. (b) Microfibrous nickel mesh sheet.

junctures [105]. Tatarchuk *et al* initially developed this method to produce high surface area electrodes with adjustable void volumes and porosities for heterogeneous catalysis in batteries, fuel cells, and double-layer capacitors [106, 107, 108, 109].

The MFMs come in sheets a few millimeters thick. The desired damping geometry can then be cut out of the sheet using shears or a straight razor. The mesh sheets are displayed in Figure 5.2. After the desired damping geometry is cut from the sheet, the damper can be solder-attached to an isolator. The solder attachment procedure used to adhere MFMs to MVIs for vibration isolation testing is detailed in Appendix D. First, the mesh is solder-attached to a Cu base insert. The base insert is rigidly fixed to the testing fixture using an adhesive. Next, the isolator is solder-attached to the mesh. Figure 5.3 displays the complete insert, mesh damper, and MVI configuration using Ni mesh.

Previous works have investigated the damping properties of microfibrous meshes. Soobramaney *et al* studied the damping and stiffness properties of sheets of microfibrous Ni mesh with varying fiber diameters from 4 μm to 12 μm when subjected to a range of accelerations.

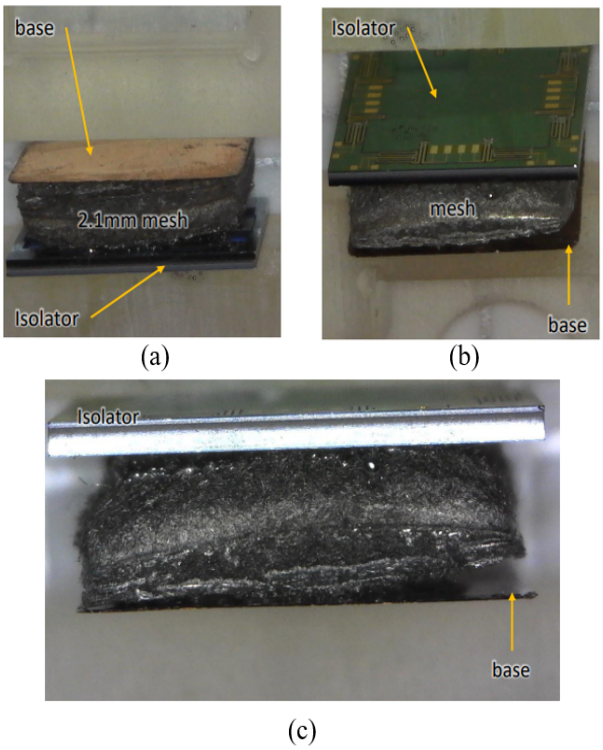

Figure 5.3: I3 MVI with Microfibrous Ni Mesh added for damping. (a) View of Cu base to be fixed to the test fixture. (b) Isolator view. (c) Side view.

Experimentally determined damping ratios range from 0.1 to 0.21 with increasing fiber diameter [110]. Uses of Ni mesh as a damper include damping to reduce high frequency noise to improve MEMS gyroscope performance and damping to reduce noise pollution emitted from a motorcycle muffler [111, 112]. The damping properties of the Cu mesh also investigated in this work have not been studied in detail.

5.2 Polymer Damping

Polymers are used to damp unwanted vibration in a wide variety of applications including acoustics, structural engineering, and ergonomics. The primary damping mechanism of polymers under cyclic loading is the generation of heat due to internal friction generated among polymer chains during deformation. The energy loss per cycle is given by [113]:

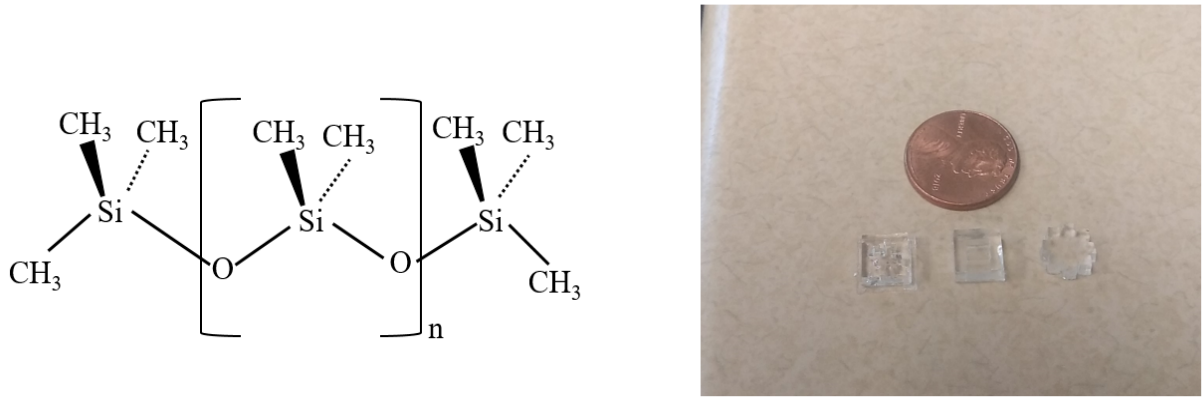

(a) (b)

Figure 5.4: Polydimethylsiloxane (PDMS) (a) PDMS molecular structure. (b) Sample PDMS damping geometries produced with 10:1 cure ratio (polymer:catalyst).

$$U_{\mathrm{d}} = \pi E'' {\epsilon_0}^2 \tag{5.1}$$

Where U_d is the energy converted to heat per cycle and ϵ_0 is maximum strain deformation of the polymer. Under cyclic loading polymers can be modeled as viscoelastic solids using the Kelvin-Voigt model discussed in Section 3.2.2 [114]. The MVI damping performance of two polymers, polydimethylsiloxane (PDMS) and a commercially available viscoelastic urethane (Sorbothane), are explored in this work.

5.2.1 Polydimethylsiloxane (PDMS)

PDMS is a commercially available polymer composed of $[SiO(CH_3)_2]$ subunits. Applications for PDMS have grown in recent years due to its compatibility with soft lithography and fabrication process techniques as well as its biocompatibility and permeability to many gases. PDMS is prepared from a two part elastomer and catalyst mixture using commercially available Sylgard^{TM} 184 by Dow® [115]. The preparation procedure used to fabricate PDMS dampers discussed in this work is detailed in Appendix E. PDMS is cured in a

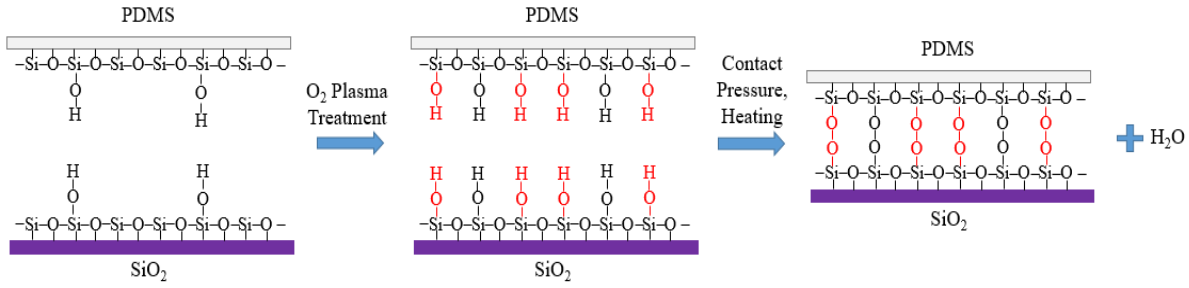

Figure 5.5: Bonding mechanism of PDMS to SiO_2 using oxygen plasma treatment. Reproduced from [119].

stereolithography 3D-printed mold (Formlabs Form 3 printer) to achieve desired damper geometries [Figure E.1]. Figure 5.4(a) displays the chemical structure of PDMS and Figure 5.4(b) displays PDMS samples fabricated and tested for their MVI damping properties.

The mechanical stiffness and damping properties of PDMS have been investigated in a number of works. Roubino and Ioppolo studied the Young's modulus and loss factor of a number of PDMS beams ranging in length from 3.7 to 9.2 mm with 300 μm thicknesses [116]. The studied frequency range was from 10 to 1500 Hz. The measured Young's moduli ranged from 1 to 2.6 MPa in 10:1 (elastomer to catalyst ratio) PDMS and from 0.6 to 1.1 MPa in 20:1 PDMS. Loss factors ranged from 0.2 to 0.4 in 10:1 and 0.2 to 0.5 in 20:1 PDMS. In [117] Johnston *et al* investigated PDMS stiffness as a function of curing time and temperature in 10:1 bulk PDMS samples. Stiffness ranged from 1.32 to 2.97 MPa for curing temperatures from 25 °C to 200 °C with stiffness increasing with higher cure temperatures.

An advantage of PDMS as a damping material for MVIs is its well established ability to bond to both Si and SiO_2. Gajasinghe *et al* report the bond strength between 10:1 PDMS and Si with native oxide is 340 kPa and the bond strength between 10:1 PDMS and SiO_2 is 241 kPa [118]. These high bond strengths allow a PDMS damper to be directly bonded to the MVI handle layer. A typical bonding procedure uses an O_2 plasma treatment of both oxide and PDMS surfaces. Plasma treatment results in a higher density of hydroxyl groups

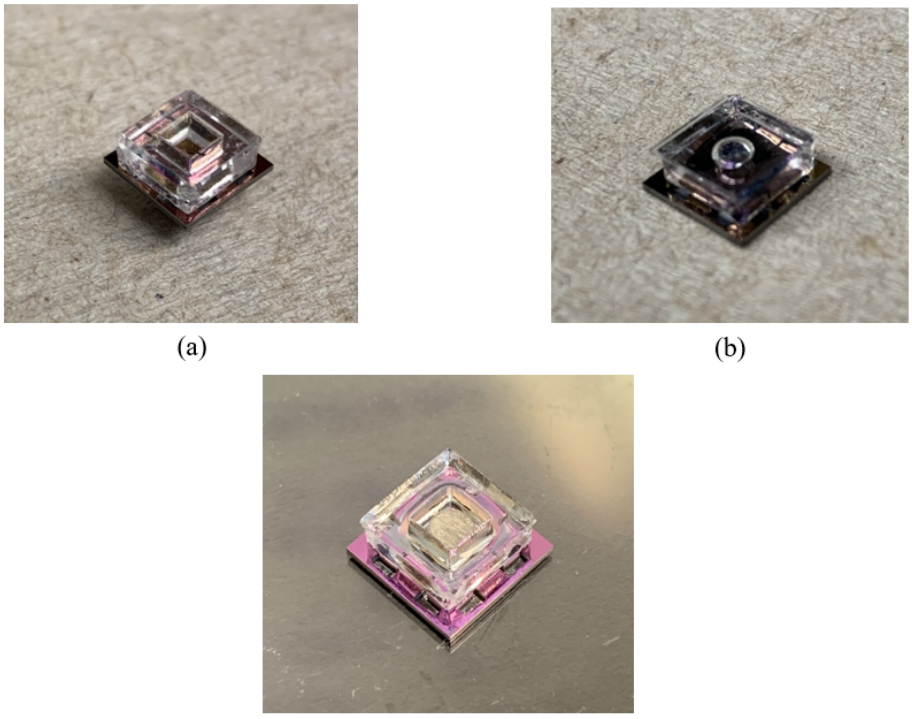

Figure 5.6: Examples of PDMS dampers bonded to I3 MVI. (a)Square donut-shaped damper. (b)Square donut-shaped damper with cavity filled with silicone oil. (c)Square donut damper with steel counter mass attached to MVI handle layer.

on the PDMS and oxide surfaces. These hydroxyl groups then form oyxgen-oxygen bonds when the two surfaces are brought into contact and heated [119]. Figure 5.5 demonstrates the bonding mechanism between PDMS and SiO_2.

The bonding procedure for adhering PDMS dampers to MVIs is borrowed from [120] which details PDMS to PDMS bonding. The alignment of the dampers to the MVIs is achieved using a 3D printed alignment jig [Figure F.1]. Appendix F details the damper-MVI adhesion procedure.

5.2.2 Viscoelastic Urethane (Sorbothane)

Sorbothane® (Sorbothane) is a viscoelastic urethane polymer that is widely used for shock and vibration damping applications. Sorbothane was developed and implemented in the late 1970's and early 1980's by Maurice Hiles as foot insoles to reduce shock experienced

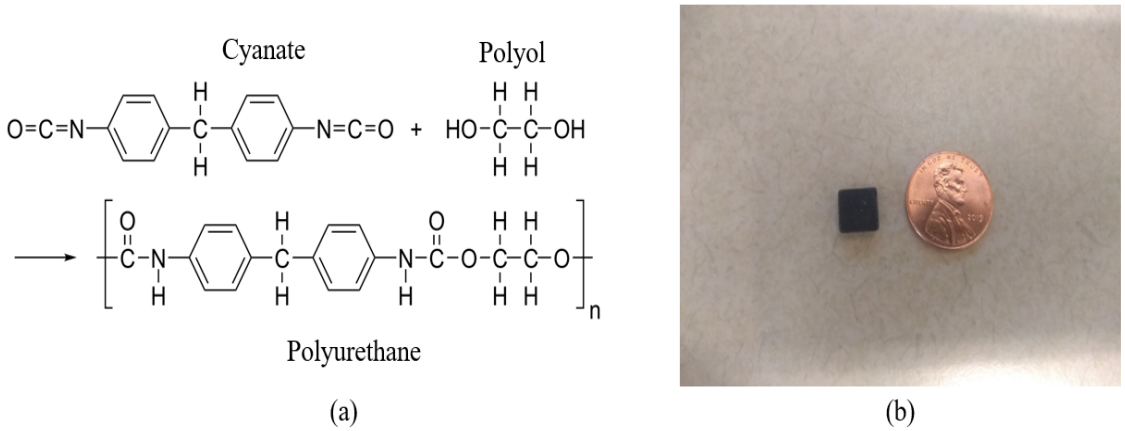

Figure 5.7: Polyurethane chemistry and Sorbothane Damper Sample. (a) Urethane monomers are formed from the reaction of an isocyanate and a polyol. (b) Sorbothane damper shown with penny for scale.

by the body during running and walking [121]. Since its introduction Sorbothane has found damping applications in fields as disparate as athletic padding [122], acoustic absorption [123], industrial gaskets, electronics, ergonomics [124], and spacecraft equipment isolation [125].

The mechanical properties of Sorbothane are well characterized for low frequencies ($f \leq 50$ Hz) and vary depending on the durometer or hardness rating of the Sorbothane. Sorbothane is available in durometer ratings of 30, 50, and 70. The loss factors at 50 Hz range are 0.37 for durometer 70, 0.65 for durometer 50, and 0.8 for durometer 30. The Young's moduli for durometers 30, 50, and 70 are 0.675, 1.2, and 2.05 MPa at 50 Hz [126].

Sorbothane damper samples are cut into 8x8 mm^2 squares from 2.54 mm thick sheets. The dampers are adhered to MVIs using industrial strength adhesive.

5.3 MFM and Polymer Damped MVI Finite Element Analysis

The modal responses and transmissibilities of the damped microisolator are simulated using COMSOL Multiphysics 5.5. The simulations are designed to emulate the testing conditions described in Section 5.4. The 110 mg proof mass with a 5 mg laser reflector is fixed to the central platform of the microisolator. The damping material is fixed to the bottom of the central platform to emulate the solder (MFM), adhesive (sorbothane), or bonding (PDMS) attachment. Figure 5.8(a) displays the model setup in COMSOL. Transmissibility is simulated via the application of harmonic excitation to the fixed outer frame of the isolator and the base of the damping material [Fig.5.8(b)]. The remaining boundaries are kept free. The transmissibility is given by the ratio of the displacement of a point in the center of the central platform divided by a reference point located on the outer frame exhibiting unity displacement.

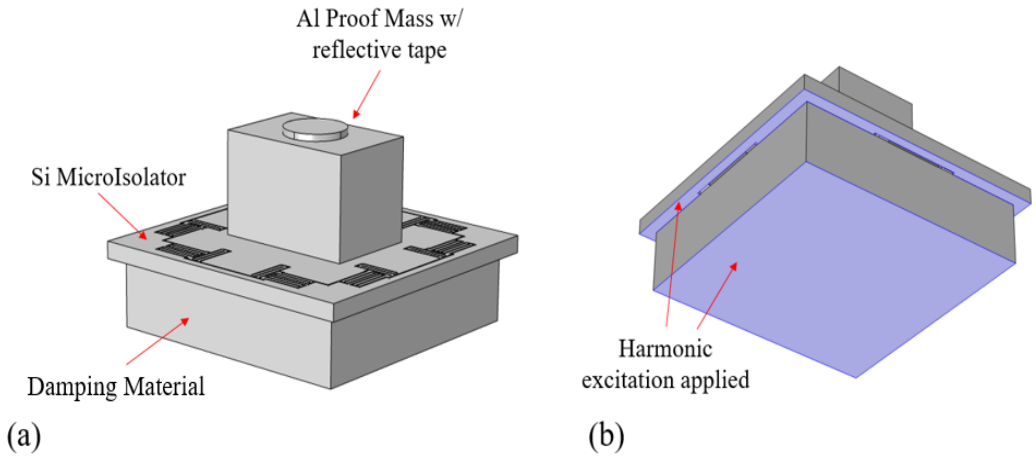

Figure 5.8: Finite element model setup for COMSOL Multiphysics simulation of isolator transmissibility. (a) Material definition of critical simulation geometries. The damping material is not present in undamped simulation. (b) Harmonic excitation applied to indicated boundaries along z-axis (out-of-plane). Harmonic excitation is applied only to the outer frame in the undamped case.

Table 5.1: Material Parameters for Frequency Domain, Modal Simulation in COMSOL Multiphysics

Material	**Young's Modulus, E (GPa)**	**Poisson's Ratio, ν**	**Density (kg/m^3)**	**Loss Factor**
Silicon	130	0.28	2330	-
Aluminum	70	0.35	2700	-
Nickel Mesh	$0.3*10^{-3}$	0.49	600	0.42
Copper Mesh	$0.3*10^{-3}$	0.49	300	0.42
PDMS (10:1)	$1*10^{-3}$	0.495	970	$10^{-4}(f)$ + 0.18
Sorbothane (Duro 70)	$2*10^{-3}$	0.5	1362	0.44

A linear, elastic material model is used to define each of the simulated structures. The Young's Modulus, E, of silicon is set to 130 GPa which corresponds to the out-of-plane modulus for a <100> Si wafer [75]. Table 5.1 lists the material parameters utilized in simulation. The appropriate E for the Ni mesh is calculated from the experimentally determined spring constant in [110]. Using Hooke's law:

$$E = \frac{kD}{A} \tag{5.2}$$

Where k is the experimentally determined spring constant (7.5 kN/m), A is the cross-sectional area of the Ni mesh contacting the microisolator handle layer (≈ 50 mm^2), and D is the depth of the Ni mesh (2 mm). Note that we assume the spring constant of the mesh to be geometry independent, while the Young's modulus is geometry dependent. This is assumed for the purposes of the FEA simulation and because mechanical characterization of the microfibrous mesh is limited. Because the Cu mesh has not been previously characterized, the material parameters for estimation of Cu mesh damping are borrowed from the Ni mesh.

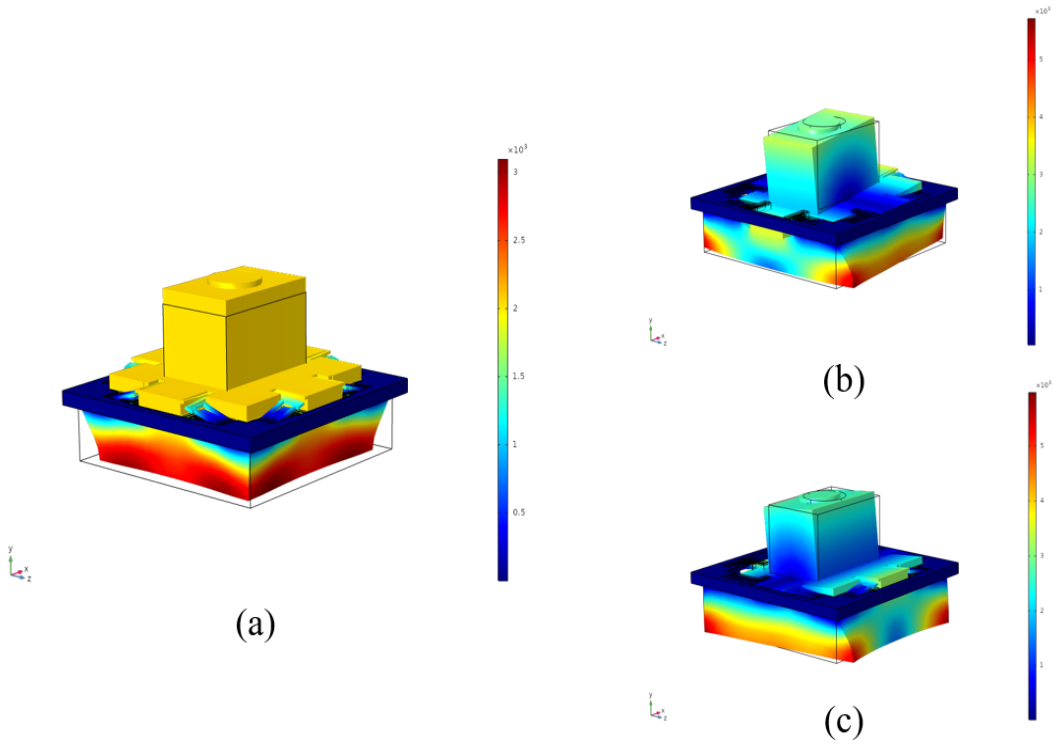

Figure 5.9: First three simulated eigenmodes for the Ni/Cu MFM damped microisolator with normalized displacement. (a) The first eigenmode appears at 1376 + j210.8 Hz. As in the undamped case, the mode shape is displacement in the out-of-plane axis. (b) The second mode shape is rotation about the z-axis at 1462 + j219.56 Hz. (c) Third eigenmode appears at 1500.6 + j234.3 Hz with rotation orthogonal to the second mode. Note, again, the frequency split between second and third modes is a result of unequal proof mass dimensions in the in-plane axes. However, the frequency split is reduced significantly in the damped case.

Equation 5.2 is also used to estimate the added stiffnesses (k) of the polymer materials in analytical calculations given Young's moduli.

The governing equation of motion used in the COMSOL frequency domain, modal solver for solid mechanics is:

$$-\rho\omega^2\mathbf{u} = \nabla \cdot (FS)^T + \mathbf{F}_v e^{j\phi} \tag{5.3}$$

Where ρ is the mass density, ω is the angular frequency, $\mathbf{u}$ is the displacement, F is the deformation gradient tensor, S is the second Piola-Kirchoff stress tensor, and $\mathbf{F}_\mathrm{v}$ and ϕ are the force magnitude and the phase of the harmonic excitation, respectively.

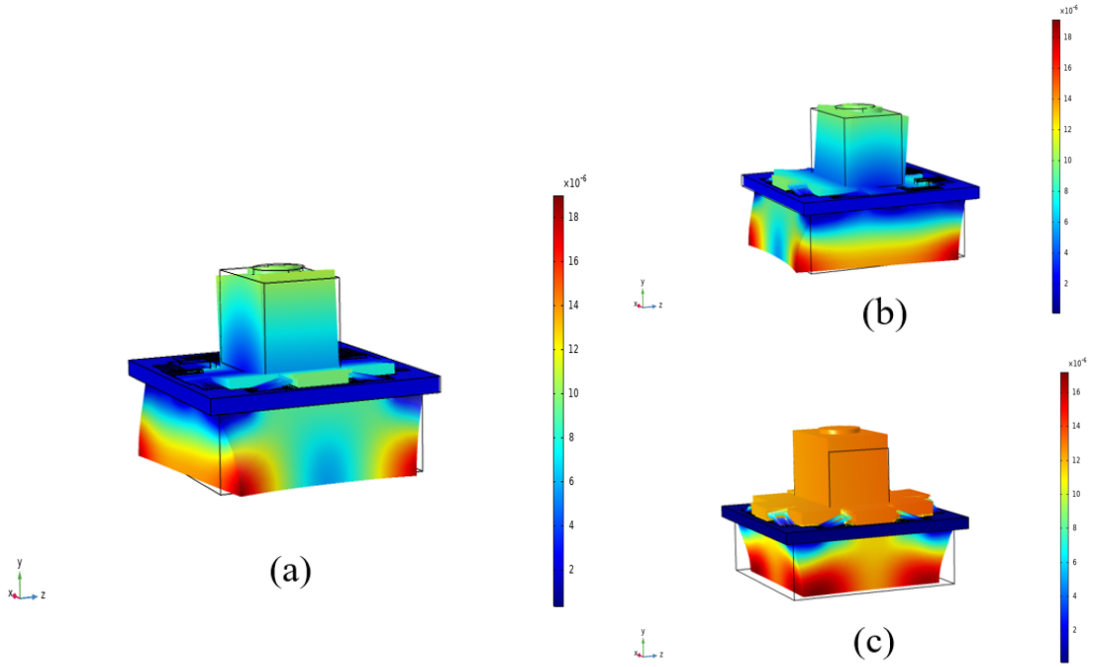

Figure 5.10: First three simulated eigenmodes for the polymer (PDMS and Sorbothane) damped microisolator with normalized displacement. Because of the greater out-of-plane stiffness of the polymer material relative to the MFMs, the rotational modes appear at lower frequencies than the primary out-of-plane mode. (a) The first eigenmode is rotation about the z-axis. (b) Second eigenmode is rotation about the x-axis. (c) Third eigenmode exhibits out-of-plane, y-axis translation. A summary of the eigenfrequencies for the respective eigenmodes for each of the damping materials is provided in Table 5.2.

Figure 5.9 displays the first three eigenmodes of the MFM damped microisolator. An isotropic damping ratio, ζ, of 0.21 ($\eta = 0.42$) is added to the MFM material to contribute damping in simulation. This value corresponds to the highest measured damping ratio for the 12 μm diameter Ni fiber mesh in [110]. The simulated fundamental eigenmode appears at 1376 + j210.8 Hz. The imaginary component of the frequency vector indicates energy loss during resonance such that the real part of the vector is near the resonant frequency, f_r, and the magnitude of the vector yields the undamped natural frequency, f_n (1391 Hz). Note that the normalized displacement of the fundamental mode is greatly reduced compared to the undamped case. Using Equation 3.18 with the stiffness of the Ni mesh added to the

Table 5.2: Modal Simulation Results for Undamped and Damped MicroIsolator

Damping Material	**1st Eigenfrequency [Hz] (Mode Shape)**	**2nd Eigenfrequency [Hz] (Mode Shape)**	**3rd Eigenfrequency [Hz] (Mode Shape)**
Undamped	844 (y-axis translation)	1245 (z-axis rotation)	1371 (x-axis rotation)
Ni/Cu Mesh	1376 + j210.8 (y-axis translation)	1462 + j219.6 (z-axis rotation)	1501 + j234.4 (x-axis rotation)
PDMS (10:1)	1513.6 + j267 (z-axis rotation)	1536.9 + j276 (x-axis rotation)	1574 + j278.8 (y-axis translation)
Sorbothane (Duro 70)	2199 + j438.2 (z-axis rotation)	2229 + j445.4 (x-axis rotation)	2318 + j463.3 (y-axis translation)

total isolator stiffness, we analytically estimate $f_n \approx 1350$ Hz. The second and third modes, again, display rotation about the in-plane axes, yet the frequency split between the modes is greatly reduced relative to the undamped case ($\Delta f_r = 38$ Hz). The second eigenmode appears at 1462 + j219.56 Hz while the third mode appears at 1500.6 + j234.3 Hz.

Figure 5.10 shows the first three eigenmodes for the polymer damped microisolator. Both the PDMS and Sorbothane damped microisolator exhibit rotational modes at lower frequencies than the out-of-plane, y-axis translation mode. This is likely due to the increased stiffness in the out-of-plane direction due to the higher values of E for both polymers. A summary of the eigenfrequencies and their corresponding modes shapes is given in Table 5.2.

In addition to the eigenmodes, the displacement transmissibility is simulated for the damped case. The results are presented in the subsequent section as a comparison to the measured experimental results.

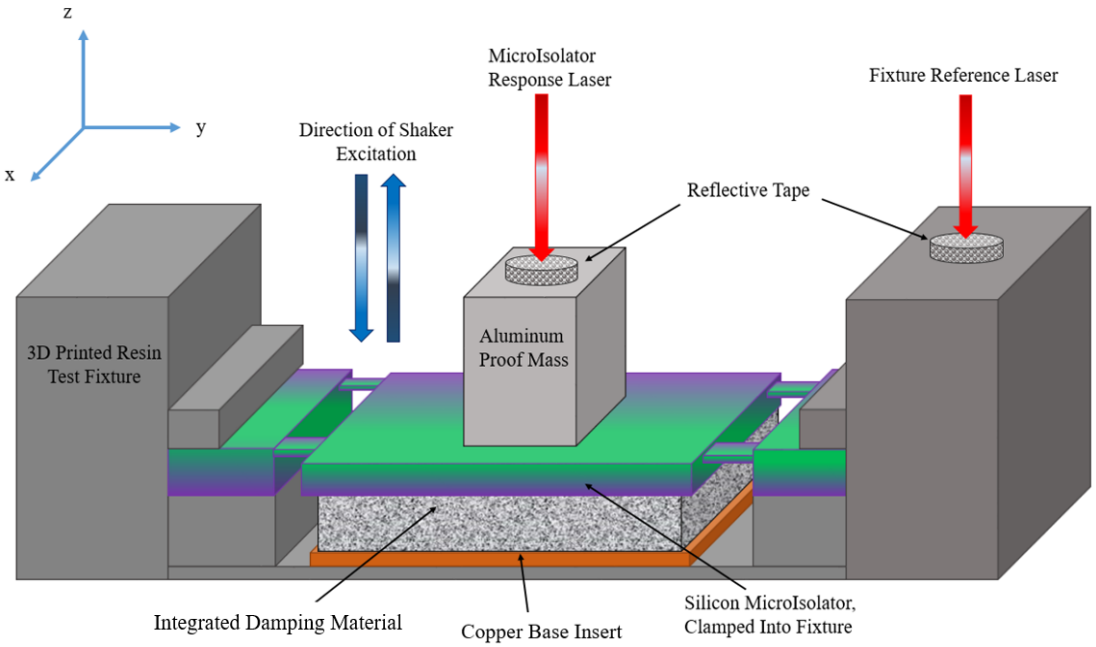

Figure 5.11: Transmissibility test setup for addition of integrated damping materials (MFMs and polymers). A copper base insert is added to fix the the bottom of the MFMs to the to the printed test fixture.

5.4 MFM and Polymer Damped MVI Transmissibility Testing

The damping performance of the MFMs and polymers on the dynamic response of an I3 MVI was tested using the transmissibility test setup detailed in Section 4.3.1. The integrated damping material is added to the test setup as shown in Figure 5.11. The results of the damped MVI transmissibility test are given in Section 5.4.1 (Ni and Cu microfibrous meshes) and Section 5.4.2 (PDMS and Sorbothane).

5.4.1 Microfibrous Mesh Damping Results

Nickel Mesh Damping Results

The experimental results of the Ni mesh damped isolator are presented in Figure 5.12 along with the analytically derived and FEA simulated transmissibility profiles. Note that in the analytical calculation $\zeta = 0.21$ defines the *system* damping ratio according to equation 2. Whereas, $\zeta = 0.21$ is used to define just the damping contributed by the Ni mesh in FEA

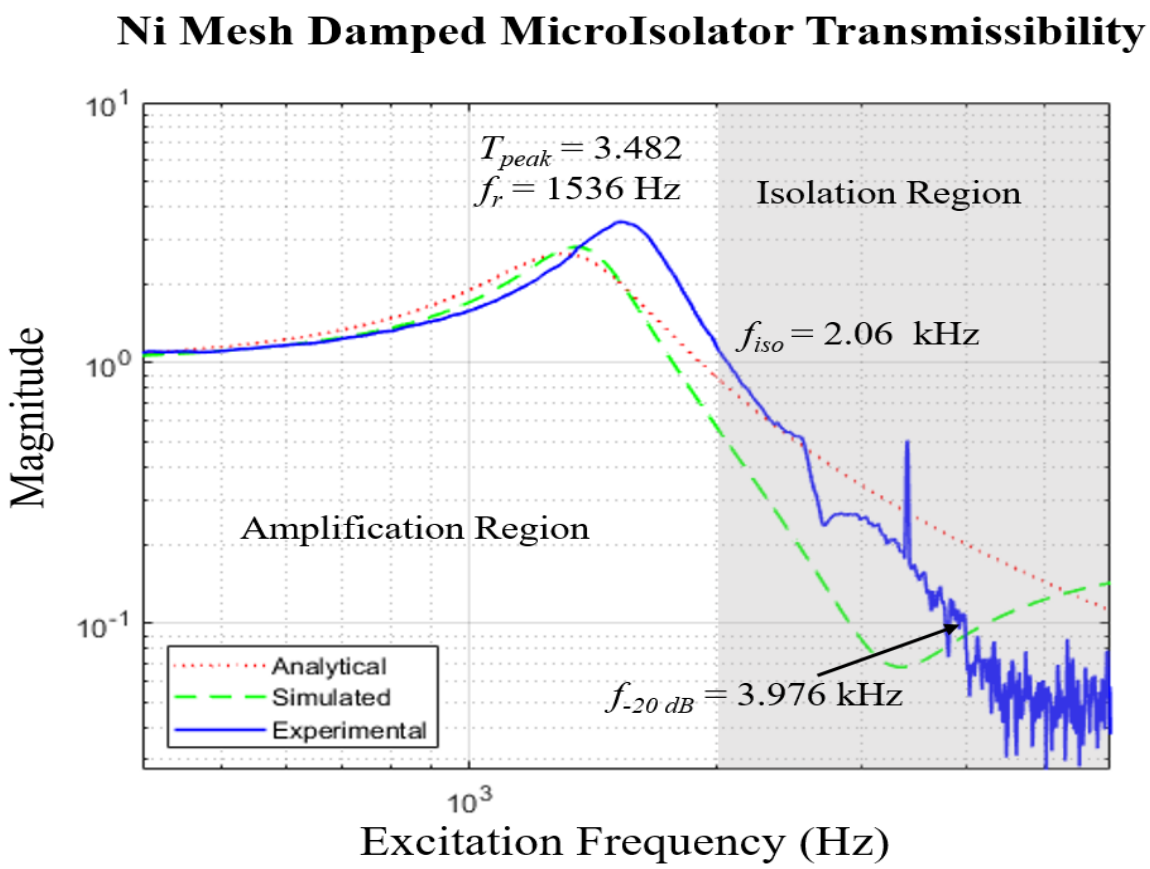

Figure 5.12: Nickel mesh damped microisolator transmissibilities for analytical, simulated, and experimental cases with amplification and isolation regions shown for experimental data. Peak transmissibility is reduced to 3.482 and resonant frequency is increased to 1.536 kHz. The peak transmissibilities of the analytical and simulated cases are 2.625 at 1.3 kHz and 2.789 at 1.35 kHz, respectively.

simulation. The assumption in both cases is that the Ni mesh damping will dominate any other loss mechanisms present in the test emulation.

As in the undamped case, these experimental results are the average of 8000 samples at each frequency step. Experiment demonstrates significantly reduced peak transmissibility in the Ni mesh damped case relative to the undamped case ($T_{peak} = 3.48$ vs. 11.36) as well as an increase in the resonant frequency ($f_r = 1536$ vs. 832 Hz). Additionally, the isolation frequency shifts upward by approximately 1 kHz due to the added stiffness of the mesh. The frequency at which the the isolator displacement is 10% of the input displacement, f_{-20dB}, is 3.976 kHz.

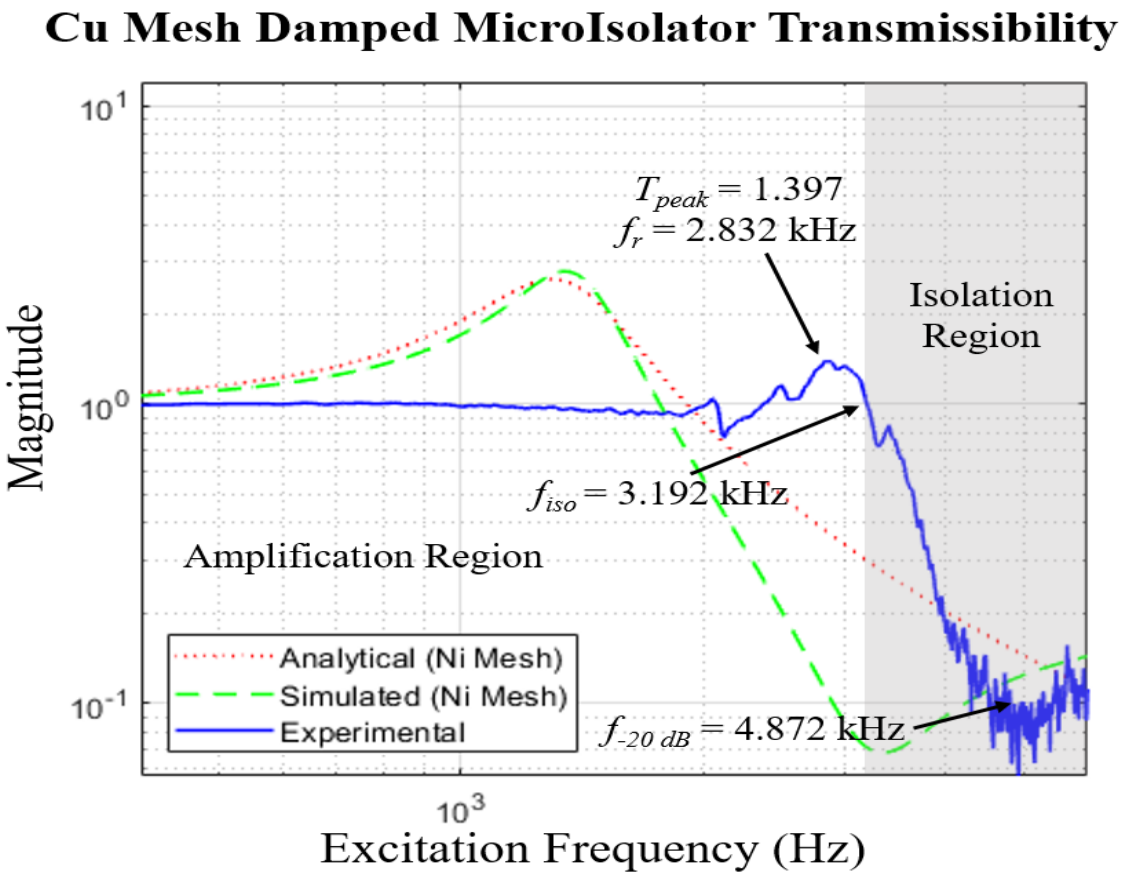

Figure 5.13: Copper mesh damped microisolator for experimental case compared to analytical and simulated cases for Ni mesh damped isolator. The Cu mesh exhibits significantly greater stiffness and damping than the Ni mesh isolator. Observed peak transmissibility is just 1.397 at 2.832 kHz. The isolation region begins at 3.192 kHz and the -20 dB frequency is at 4.872 kHz.

Cu Mesh Damping Results

The experimentally observed transmissibility profile for the Cu mesh damped microisolator is shown in Figure 5.13. The observed transmissibility profile is compared to the simulated and calculated profile for the Ni mesh damped microisolator.

The Cu mesh damped microisolator exhibits a peak transmissibility of 1.397 at 2.832 kHz. The isolation region begins at 2.832 kHz and the -20 dB frequency occurs at 4.872 kHz. The Cu mesh contributes much higher damping and stiffness to the microisolator than the Ni mesh.

5.4.2 Polymer Damping Results

PDMS Damping Results

PDMS damping of the microisolator results in a T_{peak} of 2.353 at 1.792 kHz. The transmissibility profile is displayed in Figure 5.14. The isolation frequency is increased to 2.352 kHz and the -20 dB frequency occurs at 3.648 kHz.

The experimentally observed peak transmissibility differs slightly from the analytically derived peak transmissibility (2.991 at 1.749 kHz) and the simulated peak transmissibility (2.558 at 1.53 kHz). Notably, the experimental transmissibility profile exhibits an additional

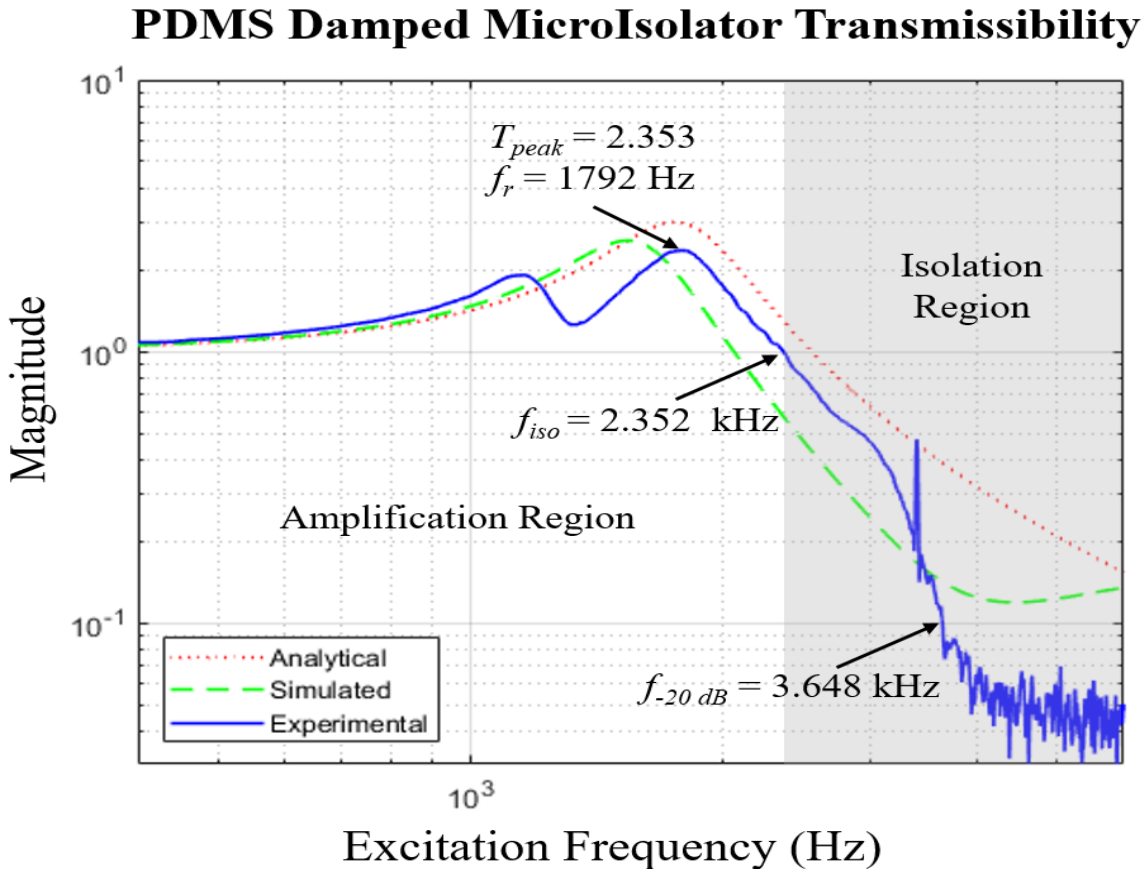

Figure 5.14: PDMS (10:1) damped microisolator transmissibilities for analytical, simulated, and experimental cases. Peak transmissibility is reduced to 2.353 at 1.792 kHz. Isolation region begins at 2.352 kHz and the -20 dB frequency is 3.648 kHz. Analytical peak transmissibility is 2.991 at 1.749 kHz. The simulated peak transmissibility 2.558 at 1.53 kHz. Note the presence of an additional peak at 1.15 kHz. This is likely due to rotational modes exhibiting some out-of-plane displacement.

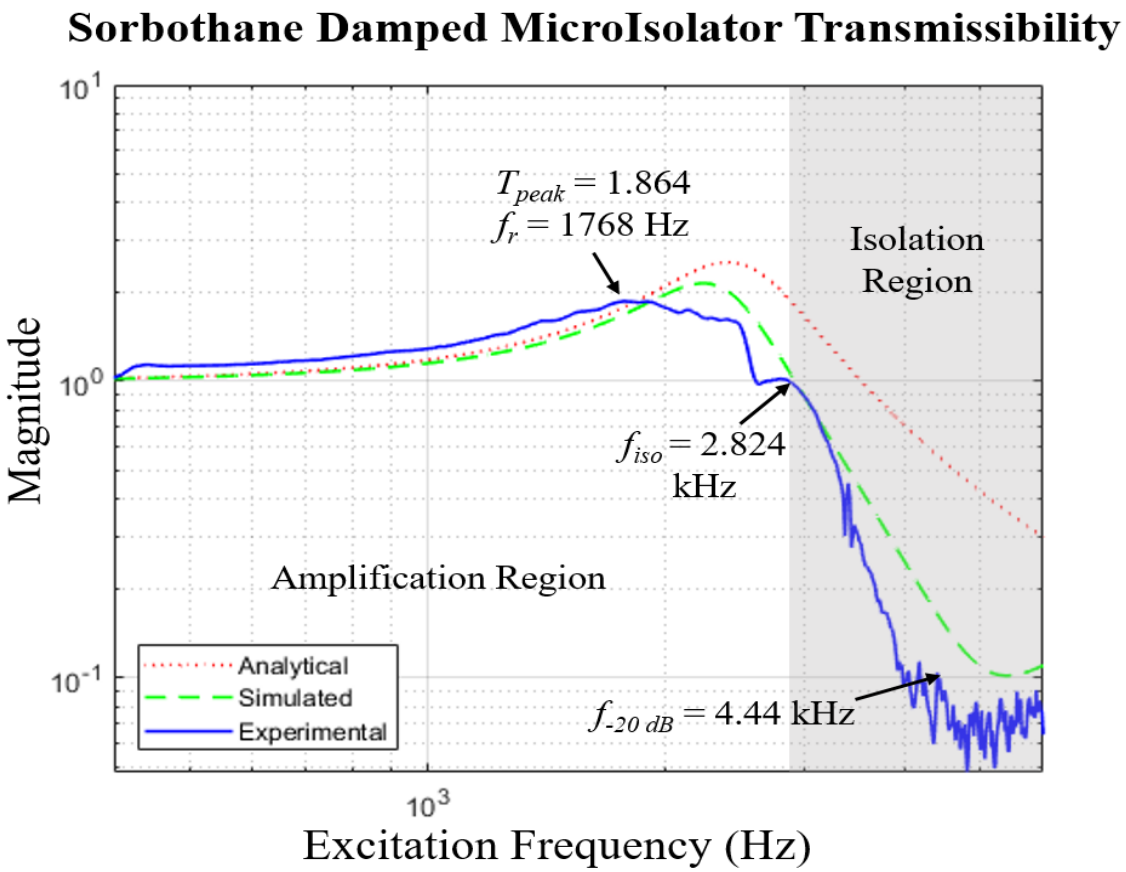

Figure 5.15: Sorbothane® Duro 70 damped microisolator transmissibilities for analytical, simulated, and experimental cases. The peak transmissibility under sorbothane damping is reduced to 1.864 at 1.768 kHz. Experimental results perform better than FEA simulated model (2.143 at 2.23 kHz) and analytical results (2.527 at 2.405 kHz). The isolation region begins at 2.824 kHz with a -20 dB frequency of 4.44 kHz..

resonance at 1.15 kHz. This additional resonance is likely from out-of-plane displacement caused by the rotational modes observed in FEA simulation. These modes are also likely present, but less noticeably so due to the greater damping, in the sorbothane damped microisolator.

The analytically calculated transmissibility assumes an added k_{damp} of 20 kN/m from PDMS. This is estimated using Equation 5.2 and estimating k from a known E ($\approx$1 MPa for 10:1 PDMS).

Sorbothane Damping Results

The sorbothane damped transmissibility results are displayed in Figure 5.15. Sorbothane damping reduces T_{peak} to just 1.864 at 1.768 kHz. The mechanical stiffness of the Sorbothane increases the resonant frequency and the isolation frequency (2.824 kHz) relative to the undamped case. Transmissibility is reduced to 0.1 at 4.44 kHz.

Experimentally observed transmissibility differs slightly from the results derived via simulation and analysis. FEA simulated T_{peak} was 2.14 at 2.23 kHz. Analytical results determined from Equation 3.19 estimate T_{peak} to be 2.527 at 2.4 kHz. The resonant frequency is estimated using an added stiffness of 40 kN/m from the Sorbothane (from Equation 5.2).

5.4.3 Damping Material Performance Summary

A summary of the critical performance metrics for each of the undamped and damped cases is provided in Table 5.3 and Table 5.4. Note that the derived natural frequency, f_n, quality factor, Q, damping ratio, ζ_{eff}, and stiffness ratio, N, assume the second-order KV-damped transmissibility model discussed in Chapter III.

Experimental results, in agreement with both analytical and simulated results, demonstrate that not only do the added damping materials contribute additional damping to the system, they also contribute significant added stiffness. For all materials the added k_{damp} exceeded the isolator's stiffness, k_{iso}. This results in a clear design tradeoff. Reduction of the peak transmissibility is afforded at the expense of increasing the system isolation frequency and vice versa. Thus, careful design of the microisolator and careful selection of the integrated damping material is crucial to meet strict isolation requirements.

Each damping material tested possesses both advantages and disadvantages relative to other tested materials. Advantages of the use of microfibrous mesh as a passive damping material for microisolators include its compatibility with a vacuum environment due to no outgassing, its ability to be preformed into any desirable geometry, and its ability to be solder-attached to the microisolator central platform as discussed in this work. Disadvantages of the

Table 5.3: Performance Metrics for Undamped and Damped MicroIsolator

Damping Material	**Resonant Frequency, f_r (kHz)**	**Undamped Natural Frequency, f_n (kHz)**	**Isolation Frequency, f_{iso} (kHz)**	**-20 dB Frequency, f_{-20dB} (kHz)**
Undamped	0.832	0.834	1.004	4.172
Ni Mesh	1.536	1.57	2.060	3.976
Cu Mesh	2.832	3.33	3.192	4.872
Sorbothane	1.768	1.92	2.824	4.44
PDMS	1.792	1.87	2.352	3.648

Table 5.4: Additional Performance Metrics for Undamped and Damped MicroIsolator

Damping Material	**Peak Transmissibility, T_{peak}**	**Quality Factor, Q**	**Effective Damping, ζ_{eff}**	**Stiffness Ratio, N**
Undamped	11.36	11.31	0.044	0
Ni Mesh	3.482	3.31	0.151	2.5
Cu Mesh	1.397	0.90	0.51	15
Sorbothane	1.864	1.511	0.29	4.3
PDMS	2.353	2.083	0.196	4.03

MFM material are the nonelastic deformation of the MFM fibers under high displacement which results in nonuniform mesh thicknesses and reliability concerns for prolonged use, incompatibility with wafer-scale fabrication processes, and conductivity of metallic fibers which causes electrical shorting in exposed metal traces (such as those on the microisolator itself).

Advantages of polymer materials include better previous mechanical characterization, the ability (in the case of PDMS) to be integrated into a wafer-scale fabrication process, the ability (in the case of PDMS) to be bonded directly to the microisolator handle layer, and previous application to a wide variety of damping and isolation solutions (sorbothane).

Concerns for polymer damper integration include temperature dependent properties that may degrade performance in harsh environments, a propensity to outgas (PDMS), and, in the case of sorbothane, lack of a reliable method of attaching the damper to the microisolator outside of commercial or industrial adhesives.

5.5 Investigation of the Performance of Alternate Damper Geometries Using PDMS

Given the control available over the geometry of PDMS using 3D-printed molds, the PDMS dampers may be designed to meet specific isolation requirements. In this section the performance of a square "donut-shaped" PDMS damper is investigated. The intent of the design is to increase the resonant frequency at which rotational modes occur in the isolator's transmissibility relative to the resonant frequency of the primary out-of-plane mode. Ideally, these resonances will occur after the primary out-of-plane resonance unlike the observed PDMS-damped I3 transmissibility in Figure 5.14. The proposed donut geometry includes a rectangular cavity which is intended to reduce the out-of-plane stiffness while retaining the rotational stiffness along the in-plane axes. Additionally, the inclusion of a cavity allows the addition of a counter mass (Section 5.5.2) or the addition of viscous fluid intended to improve the system damping (Section 5.5.3).

5.5.1 I3 Dynamic Performance with PDMS Donut Damper

The donut damper measures 7 x 7 x 2.5 mm^3 with a 3 x 3 x 2.5 mm^3 cavity in the center. Figure 5.16(a) shows the COMSOL Multiphysics FEA model of the I3 isolator with PDMS donut damper added. FEA simulations indicate the primary resonant mode now occurs before the two rotational modes. The respective eigenfrequencies are 1620 + j307.84 Hz for the primary out-of-plane mode (Figure 5.16(b)), 1642 + j323.38 Hz for the z-axis rotational mode (Figure 5.16(c)), and 1671 + j337.6 Hz for the x-axis rotational mode (Figure 5.16(d)).

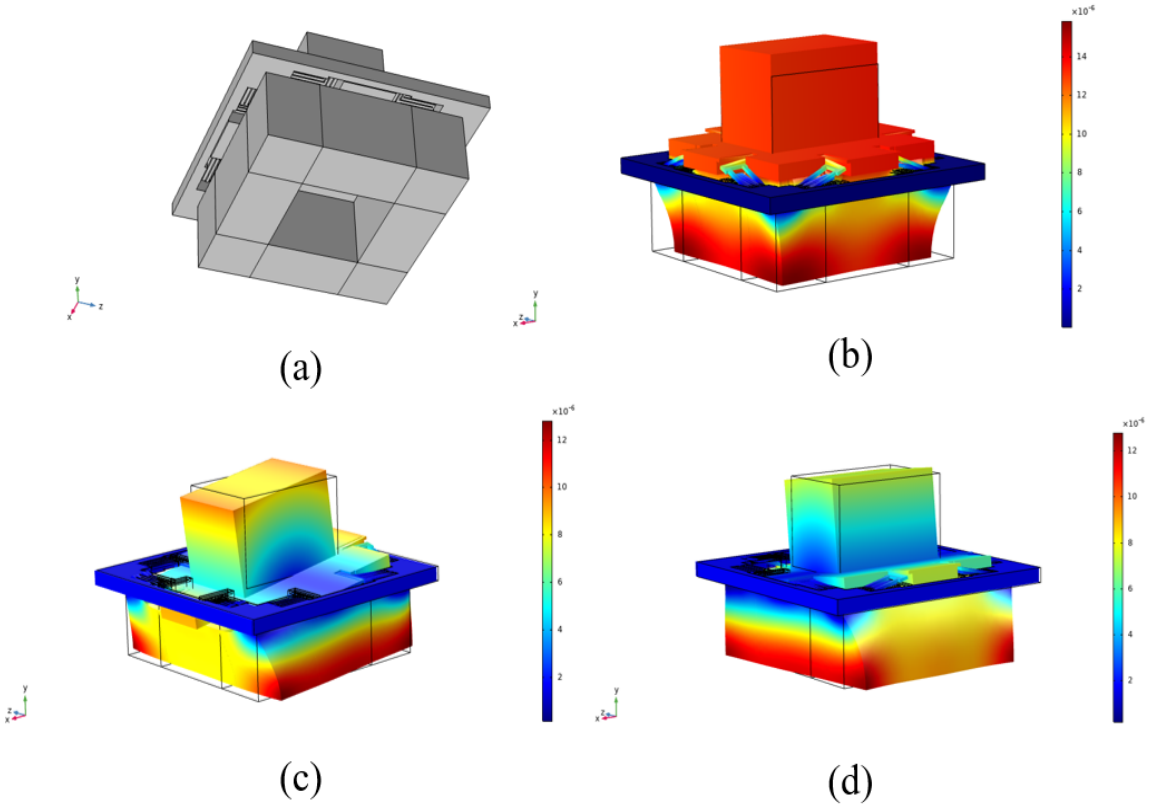

Figure 5.16: FEA Model and Eigenmodes for I3 Damped with PDMS Donut Damper. (a) FEA model showing square donut-shaped PDMS damper. (b) First resonant mode (out-of-plane) at 1620 + j307.84 Hz. (c) Second eigenmode (rotational about z-axis) at 1642 + j323.38 Hz. (d) Third eigenmode (rotational about x-axis) at 1671 + j337.6 Hz.

Thus, FEA simulation indicates that the alternative damper design reduces stiffness in the primary resonant mode while retaining stiffness in the rotational modes.

The transmssibility of an I3 MVI damped with the alternative donut-shaped damper was tested experimentally using the laser vibrometry setup detailed in Section 4.3.1. The experimentally tested sample is shown in Figure 5.6 (a). Figure 5.17 compares the experimentally observed transmissibility to the COMSOL FEA simulated transmissibility. Material parameters for PDMS were kept the same as in previous simulations. The exhibited T_{peak} for the donut-damped I3 is 2.844 and the resonant frequency, f_r, is 1.112 kHz. The

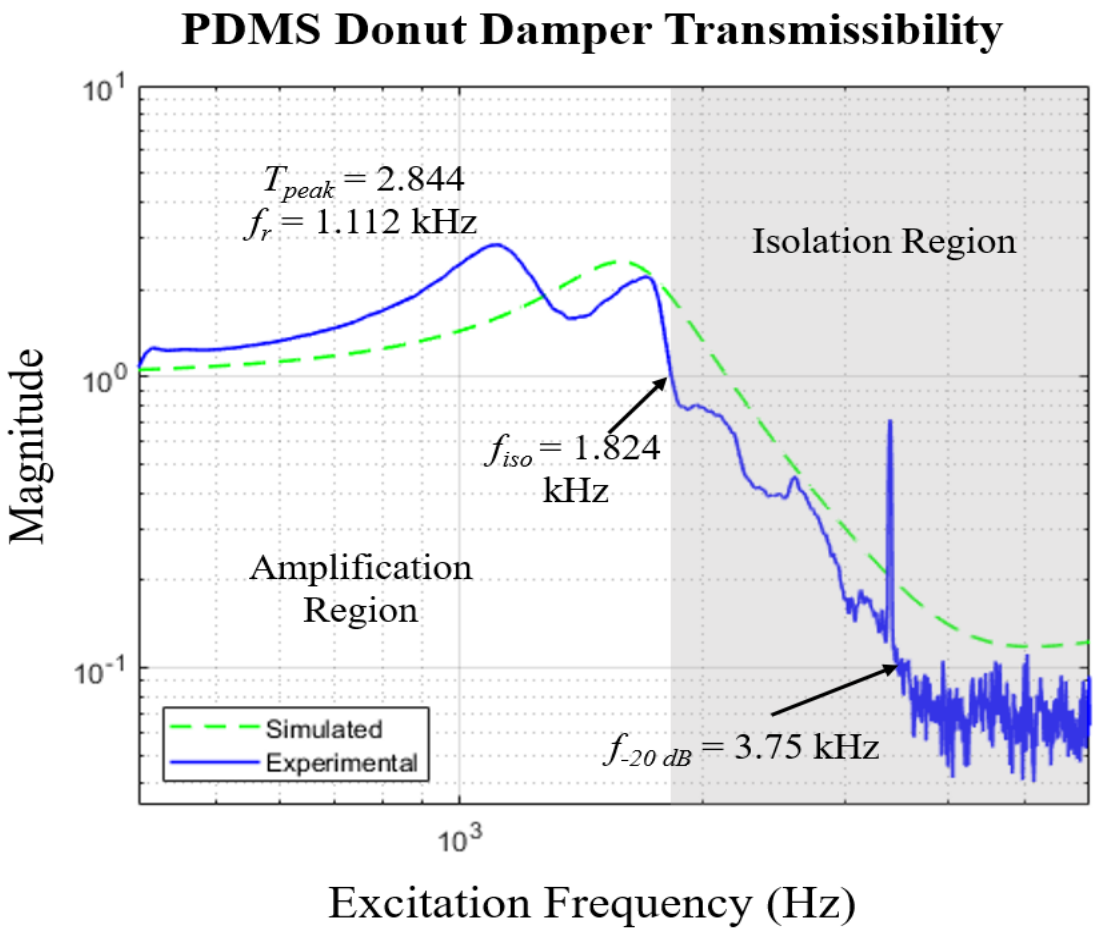

Figure 5.17: Experimental and simulated dynamic response for I3 damped with PDMS donut damper.

transmissibility profile still exhibits multiple resonances before f_{iso} (1.824 kHz), but the resonance containing T_{peak} occurs *before* the additional resonances, unlike the PDMS damped transmissibility in Section 5.4.2. This suggests that the donut-shaped damper may not have successfully reduced the out-of-plane stiffness of the isolator/damper system. Note that the second resonance occurs very close to the T_{peak} of the simulated model (1580 Hz (simulated) vs. 1688 Hz (experimental)). This suggests that the out-of-plane resonance may be occurring at the second resonant peak. However, it is also possible that the experimental setup possessed significantly less out-of-plane stiffness than in the simulated model and, thus, the first resonance is the out-of-plane resonance at a much lower f_r.

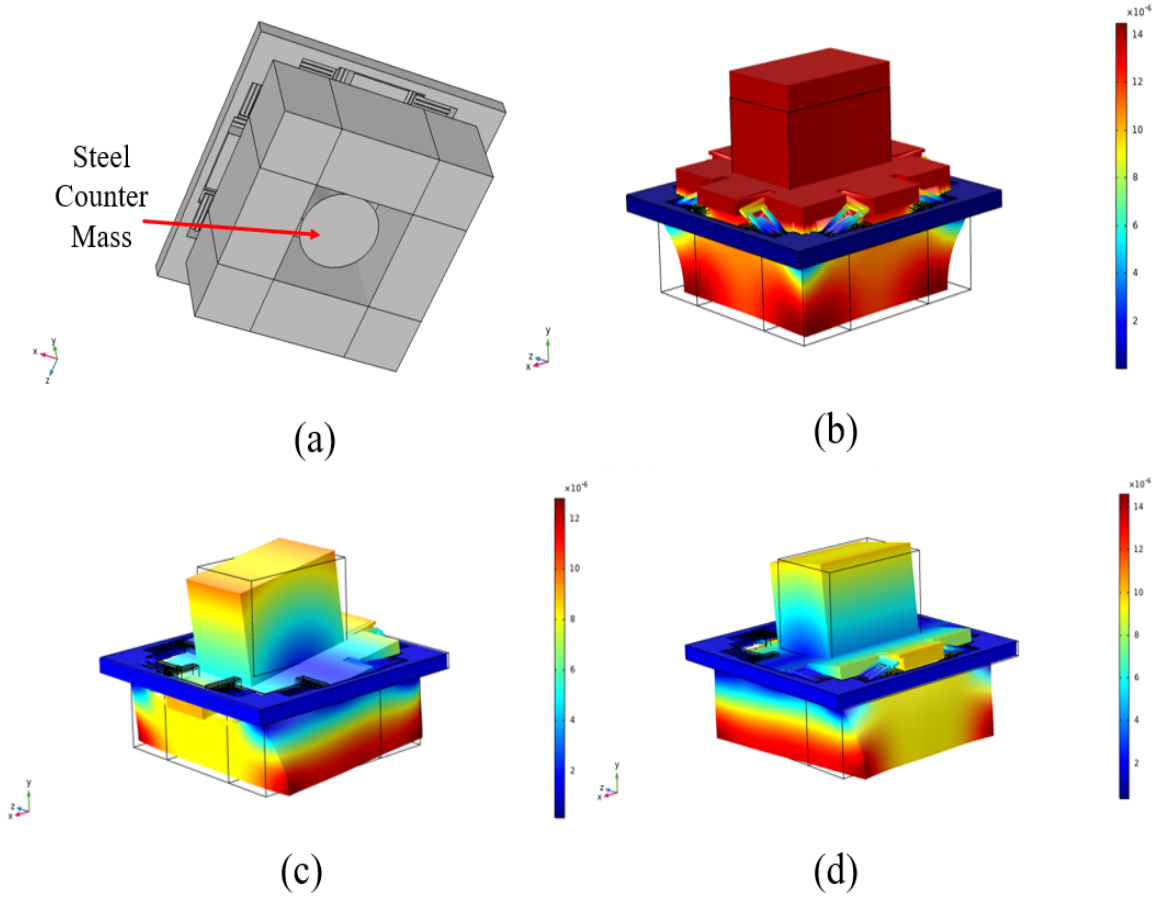

Figure 5.18: FEA model and eigenmodes for I3 damped with PDMS donut damper with added steel counter mass. (a) FEA model showing square donut-shaped PDMS damper with added steel counter mass. (b) First resonant mode (out-of-plane) at 1422 + j247 Hz. (c) Second eigenmode (rotational about z-axis) at 1620 + j308 Hz. (d) Third eigenmode (rotational about x-axis) at 1653 + j325 Hz.

5.5.2 I3 Dynamic Performance with PDMS Donut Damper and Steel Counter Mass

An additional advantage of the donut-shaped damper is the ability to attach a small counter mass to the MVI handle layer. This counter mass (CM) adds additional mass to the system resulting in a drop in the resonant frequency and an increase in the frequency split between the primary resonant mode and the rotational modes. A 76 mg steel CM with a radius of 1.33 mm and a length of 1.5 mm is attached to the MVI handle layer using an industrial strength adhesive. The FEA model for the damper setup is shown in Figure

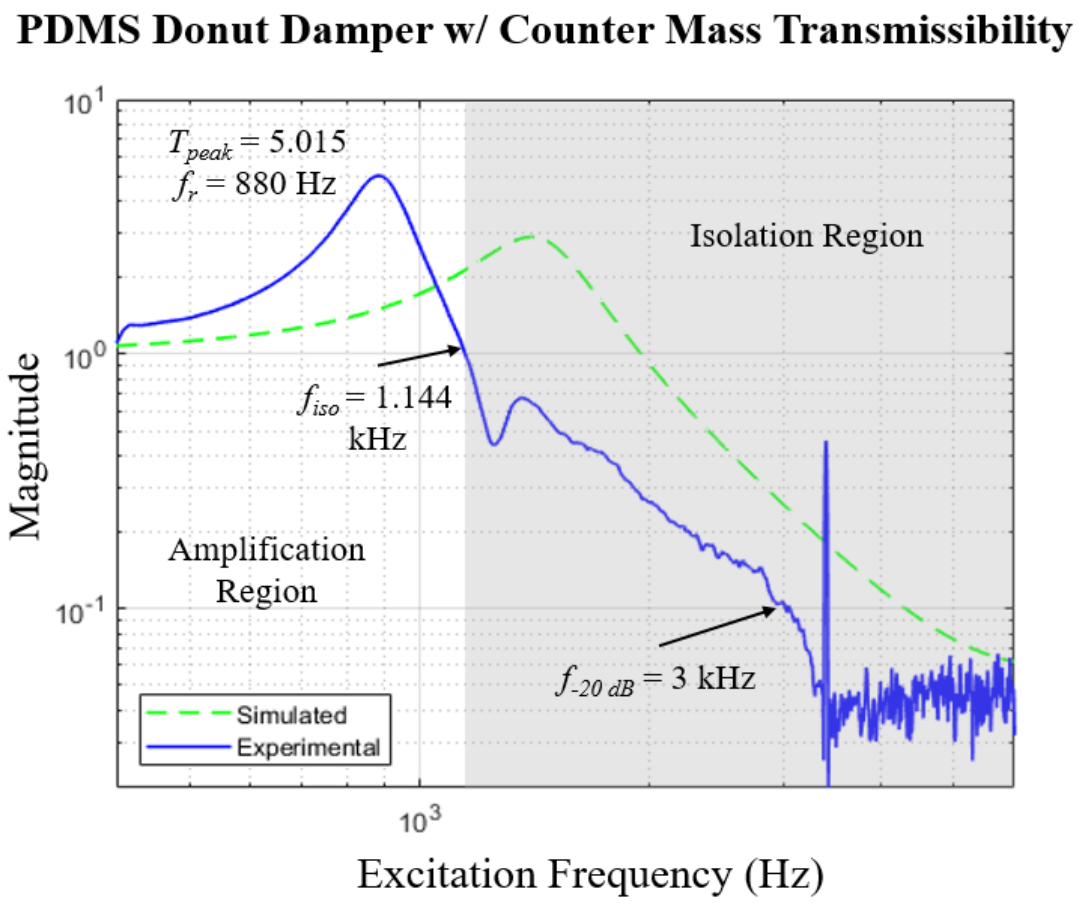

Figure 5.19: Experimental and Simulated Dynamic Response for I3 Damped with PDMS Donut Damper with Steel Counter Mass

5.18(a). FEA simulations indicate a significantly reduced primary resonance relative to the setup without CM (1422 + j247 Hz) [Fig. 5.18(b)]. The rotational modes occur at similar frequencies to the setup without CM (1620 + j308 Hz for z-axis rotation and 1653 + j325 Hz for x-axis rotation). The mode shapes are shown in Figure 5.18(c) and Figure 5.18(d).

The transmissibility of an I3 MVI damped with a donut damper and loaded with a 76 mg steel CM was experimentally tested. The experimentally tested sample is shown in Figure 5.6(c). A comparison of the experimental and simulated transmissibility is shown in Figure 5.19. Consistent with theory when total mass is increased, both the experimental and simulated T_{peak} increased and f_r decreased. Experimental transmissibility exhibited a T_{peak} of 5.015 at f_r of 880 Hz with f_{iso} at just 1.144 kHz. The results suggest CMs may be

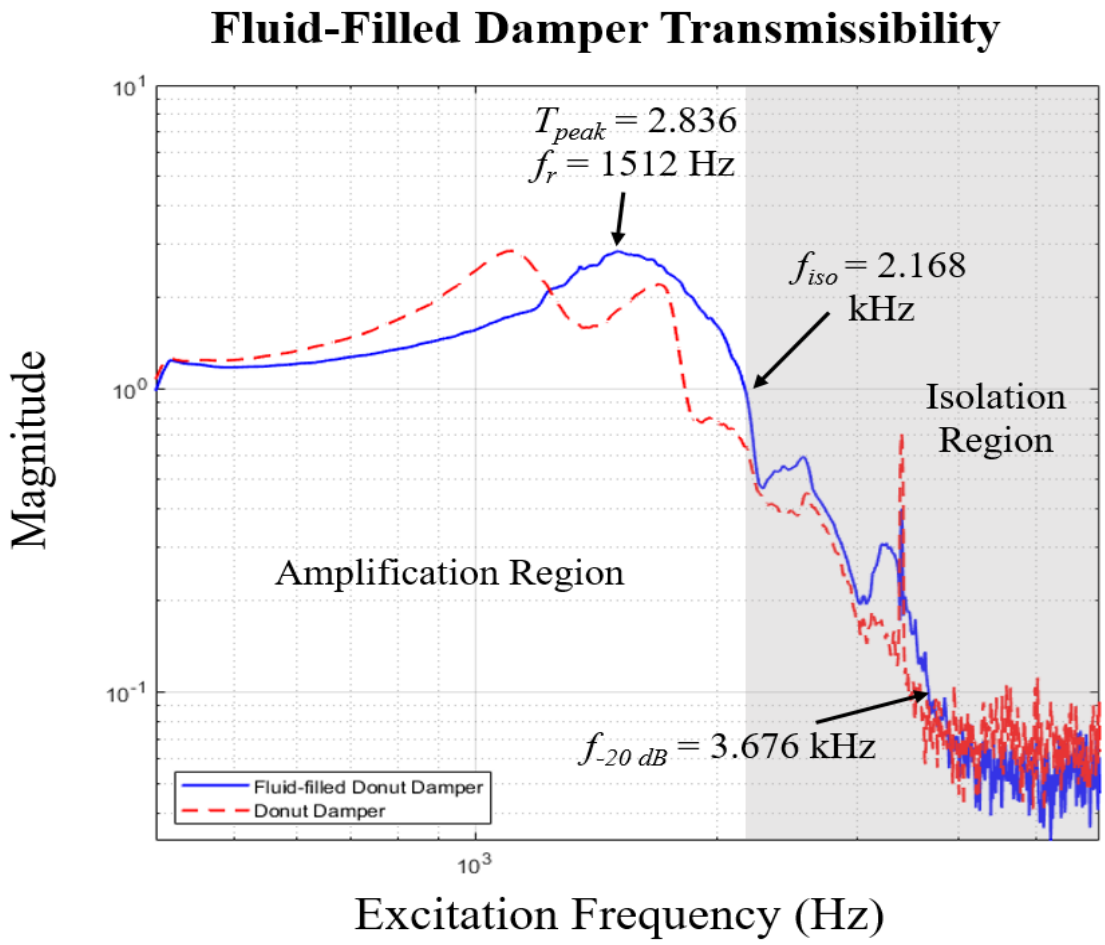

Figure 5.20: Experimental dynamic response for I3 damped with PDMS donut damper filled with silicone oil

used to tune the f_r and f_{iso} after MVI fabrication and damper integration. Also of note is the increased frequency split between the first and second resonant modes (880 Hz vs. 1352 Hz).

5.5.3 I3 Dynamic Performance with PDMS Donut Damper and Viscous Fluid filled Cavity

In [127], Singh *et al* demonstrate the improved damping performance of PDMS blocks when silicone oil filled microchannels are integrated into the PDMS blocks. An increase in the fundamental frequency and an increase in the damping ratio and loss factor is observed

relative to the original PDMS blocks. The increased damping is attributed to the development of slip boundary counditions between the silicone oil and the PDMS block which causes frictional dissipation of energy. An attempt to utilize this phenomenon for improved damping of MVIs is made via the integration of silicone oil into the PDMS donut-shaped damper.

Figure 5.20 displays the dynamic response of an I3 MVI damped with a silicone oil filled PDMS damper. The dynamic response is compared to the response from the I3 damped with PDMS donut damper without silicone oil. The silicone oil is injected into the PDMS damper prior to damper attachment to the MVI handle layer. The results are consistent with those observed in [127]. The addition of the silicone oil results in a slightly reduced T_{peak} (2.836 vs. 2.844) and a significantly increased f_r (1.512 kHz vs. 1.112 kHz). Observed f_{iso} is 2.168 kHz and f_{-20dB} is 3.676 kHz.

5.6 Reliability Studies for Damped I3 MVI

5.6.1 72 Hour Vibration Testing - Cu Mesh Damped I3 MVI

Similar to the undamped 72 hour vibration testing performed on the undamped I3 MVI, a 72 hour vibration test was performed on a Cu MFM damped I3 MVI to evaluate the long term reliability of the Cu MFM damped isolator.

The individual transmissibility profiles recorded during the test are presented in Figure 5.21. Note that the initial sample (at t = 0) exhibits a T_{peak} of 2.89 and a resonant frequency of 3.1 kHz. All subsequent samples exhibit a significantly higher T_{peak} and significantly lower resonant frequencies. Figure 5.22 displays the T_{peak} and resonant frequency for each transmissibility sample.

The change in the transmissibility profile suggests degradation of the damping performance of the Cu mesh over time. The increase in T_{peak} corresponds to a decrease in the effective damping of the material and the decrease in the resonant frequency corresponds to reduced effective stiffness. Together, these changes suggest a reduction in the adhesion

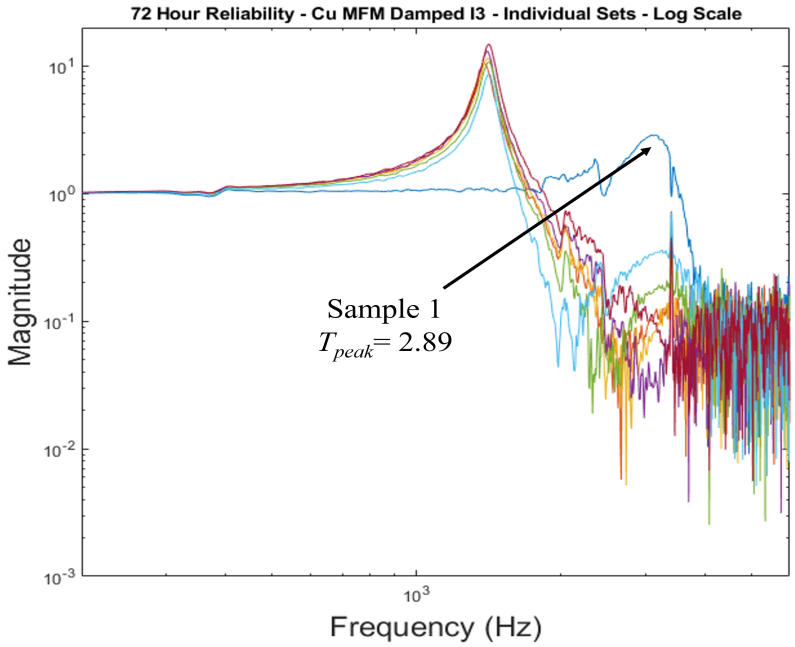

Figure 5.21: Individual transmissibility profiles for 72 hour Cu MFM damped I3 reliability test. Seven transmissibility samples are taken at 12 hour intervals to monitor change in the performance over time.

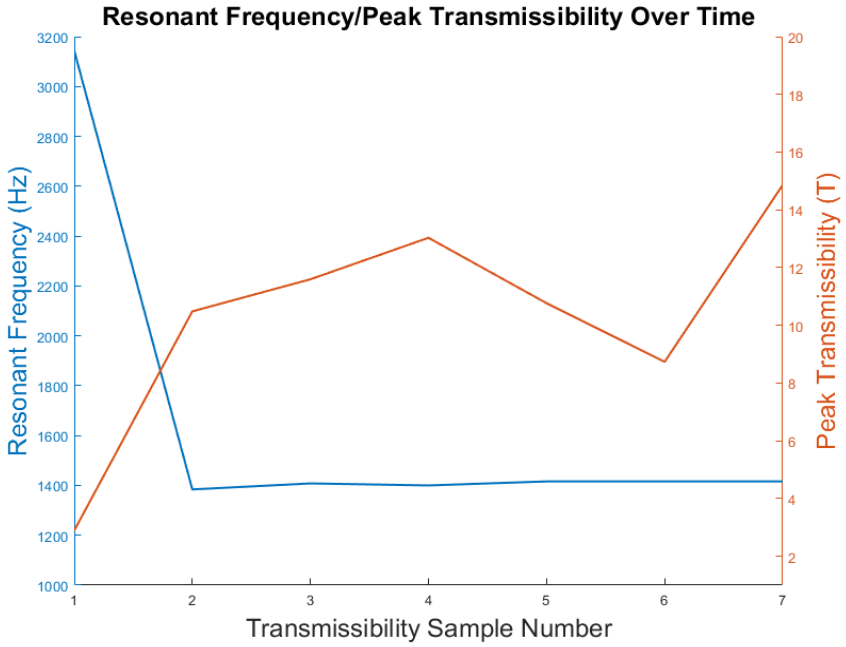

Figure 5.22: Individual transmissibility profiles for 72 hour Cu MFM damped I3 reliability test. Seven transmissibility samples are taken at 12 hour intervals to monitor change in the performance over time.

contact between the MVI and the damper and/or a change in the material properties of the MFM over time. Such a material change may be the result of copper's ductility.

While the change in damping performance of time of the Cu MFM may pose challenges to long term damping applications of the mesh, the Cu (and Ni) MFM may have single-use damping applications in harsh environments such as rocket launches.

5.6.2 72 Hour Vibration Testing - Sorbothane Damped I3 MVI

A sorbothane damped I3 MVI was also tested using the 72 hour vibration reliability test. The sorbothane damped MVI exhibited very consistent results throughout each of the seven samples. Figure 5.23 displays the transmissibility profile for each individual sample. The T_{peak} and resonant frequency for each sample is plotted in Figure 5.24. Measured T_{peak} ranged from 1.64 (Sample 5) to 2.29 (Sample 1) and resonant frequencies range from 3.312 kHz (Sample 1) to 3.456 kHz (Sample 5).

Note that similar to the Cu MFM damped test there is a change from the T_{peak} and resonant frequency of the initial (t=0) sample to the succeeding samples. However, the change is drastically reduced in the sorbothane damped test relative to the Cu MFM damped test. The results of this test suggest that sorbothane, and possibly other viscoelastic polymers, may be better suited for long duration damping applications than MFM damping materials.

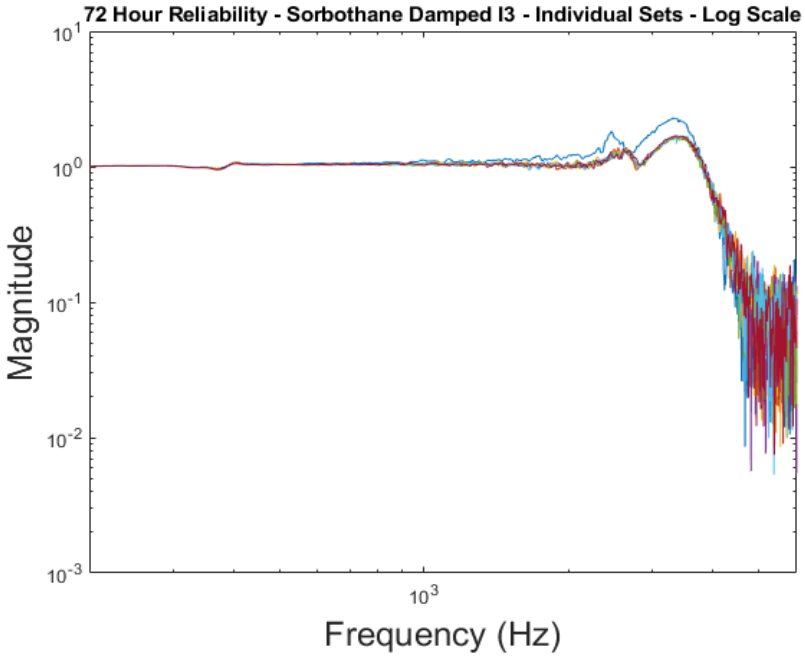

Figure 5.23: Individual transmissibility profiles for 72 hour Sorbothane damped I3 reliability test. Seven transmissibility samples are taken at 12 hour intervals to monitor change in the performance over time.

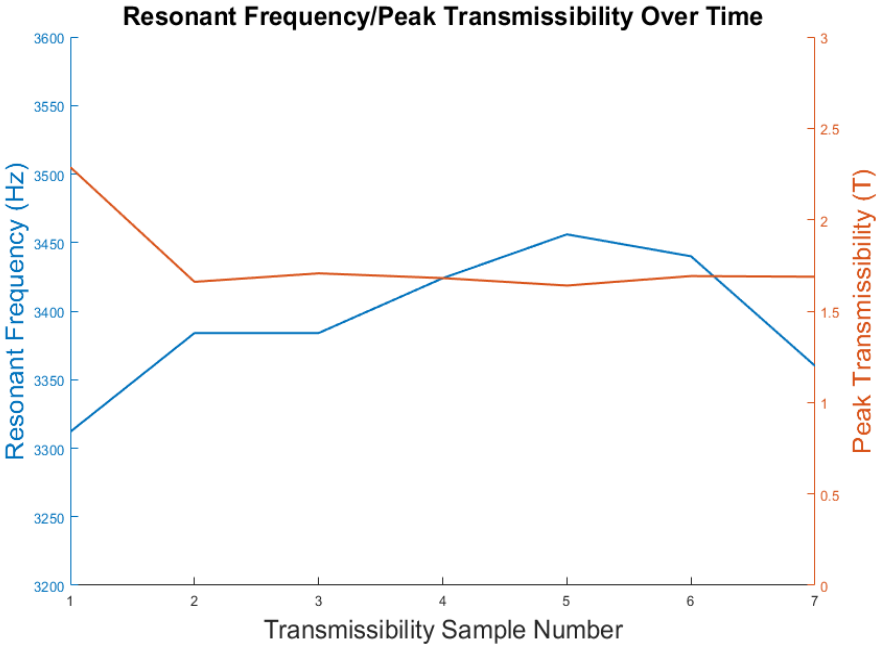

Figure 5.24: Individual transmissibility profiles for 72 hour undamped I3 reliability test. Seven transmissibility samples are taken at 12 hour intervals to monitor change in the performance over time.

Chapter 6

Validation of Micromachined Vibration Isolation via Integration of Piezoelectric Accelerometer and Future Work

6.1 Integration of Piezoelectric Accelerometer

In order to validate the isolation provided by the MVIs, a high-bandwidth piezoelectric accelerometer (ENDEVCO® Model 12M15 PICOCHIP [128], [129]) is integrated onto the MVI. Figure 6.1 shows a schematic diagram of the piezo accelerometer to be integrated. A process flow for the integration of the accelerometer onto I3 MVIs is displayed in Figure 6.2.

The first step is an additional electron beam deposition of Ti/Cu/Au (50/250/20 nm) to add metallization traces specific to the accelerometer. An aluminum shadow mask is used to mask the isolator during metal deposition. The added traces are intended to accommodate the accelerometer and to overlap the previously deposited traces in order to allow signal flow

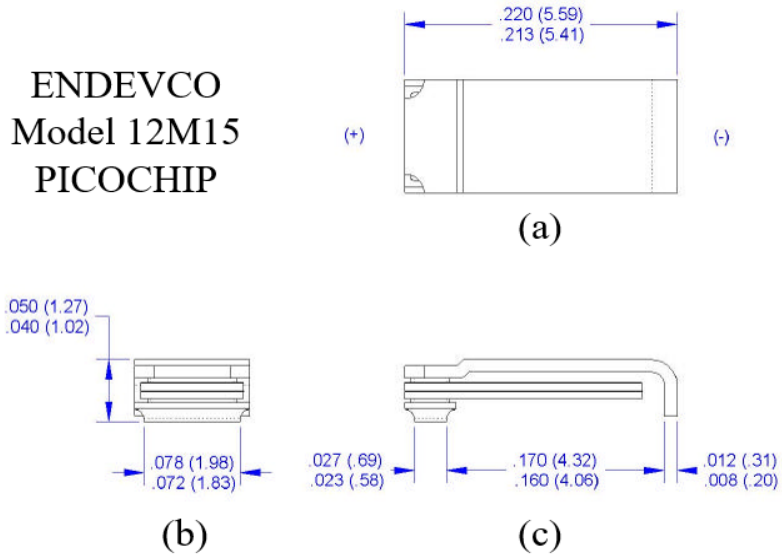

Figure 6.1: ENDEVCO® Model 12M15 PICOCHIP Schematic. Dimensions in inches (mm in parentheses). (a) Top down view. (b) Lengthwise view. (c) Side view.

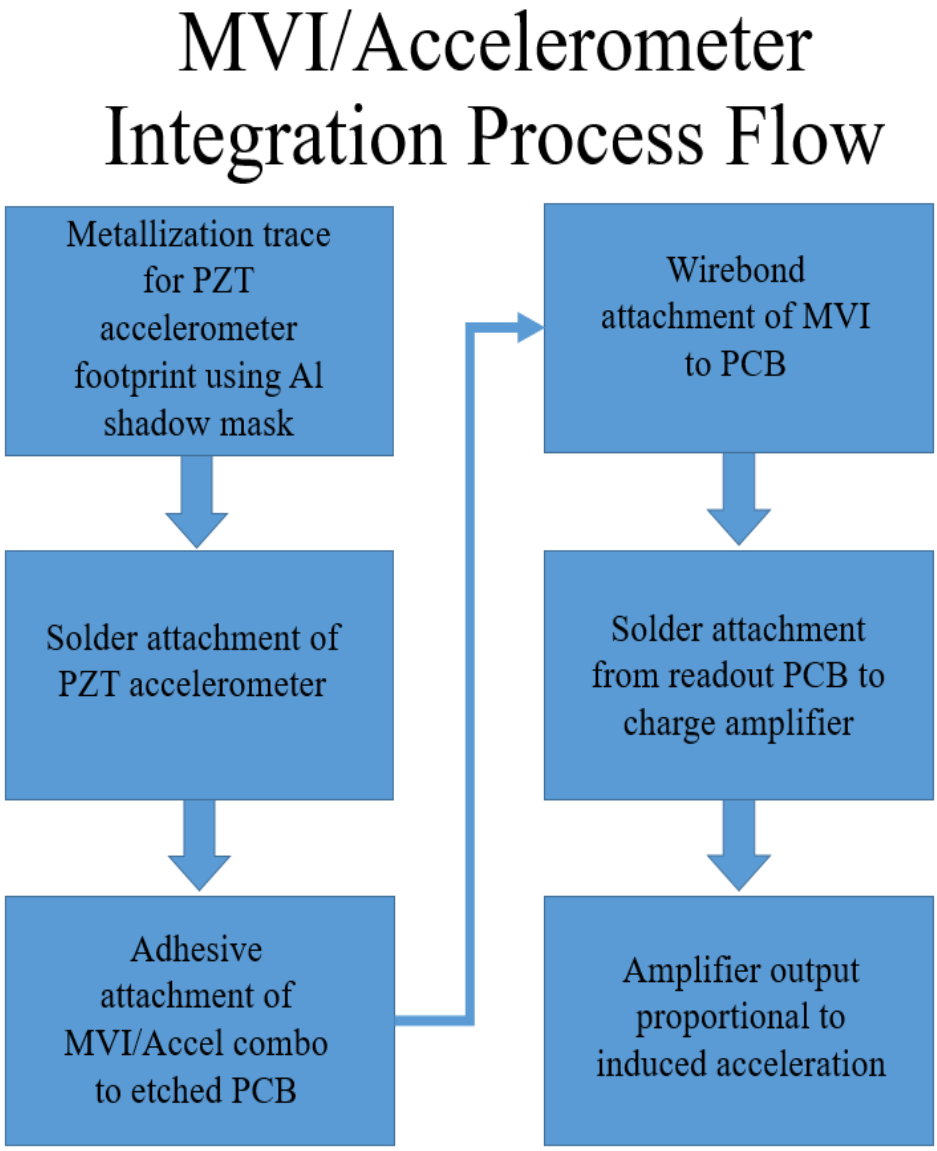

Figure 6.2: Process flow for post-fabrication integration of piezoelectric accelerometer onto MVI.

to the outer frame of the isolator. Note this step is not necessary if the first device layer metallization is designed with traces specific to the sensor to be isolated. Figure 6.3 displays the I3 MVI with the added footprints and the Al shadow mask used for metallization.

Once metallization traces are added, the accelerometer is solder attached to the device layer of the MVI. Figure 6.4 shows the Picochip accelerometer mounted onto the MVI via solder attachment. The MVI/accelerometer combination can then be integrated onto an etched copper printed circuit board (PCB). An SLA-printed spacer is added between the

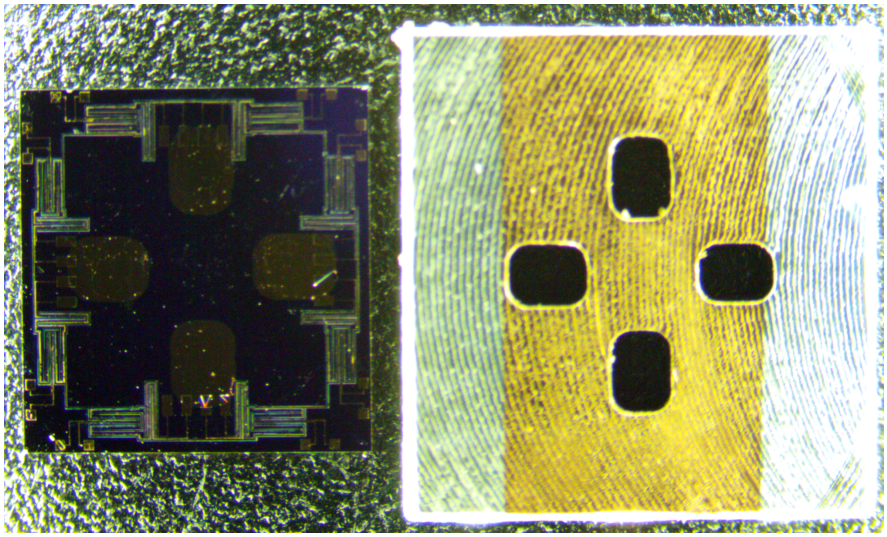

Figure 6.3: I3 MVI with added metallization traces for accelerometer integration and Al shadow mask.

MVI and the PCB to allow space for the isolator to oscillate. Additionally, the spacer allows spacing for the addition of desired damping material.

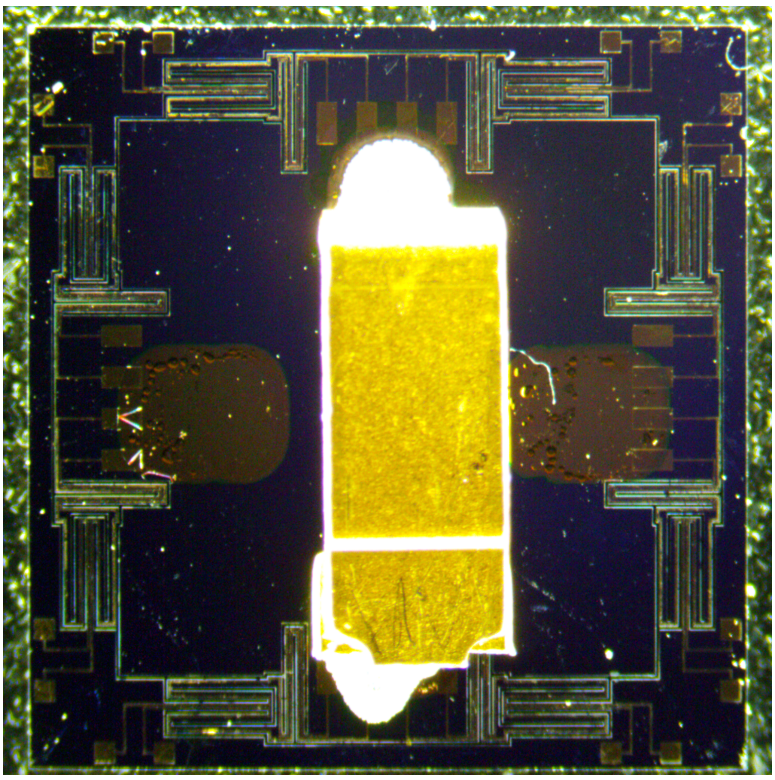

Figure 6.4: I3 MVI with piezoelectric accelerometer solder attached.

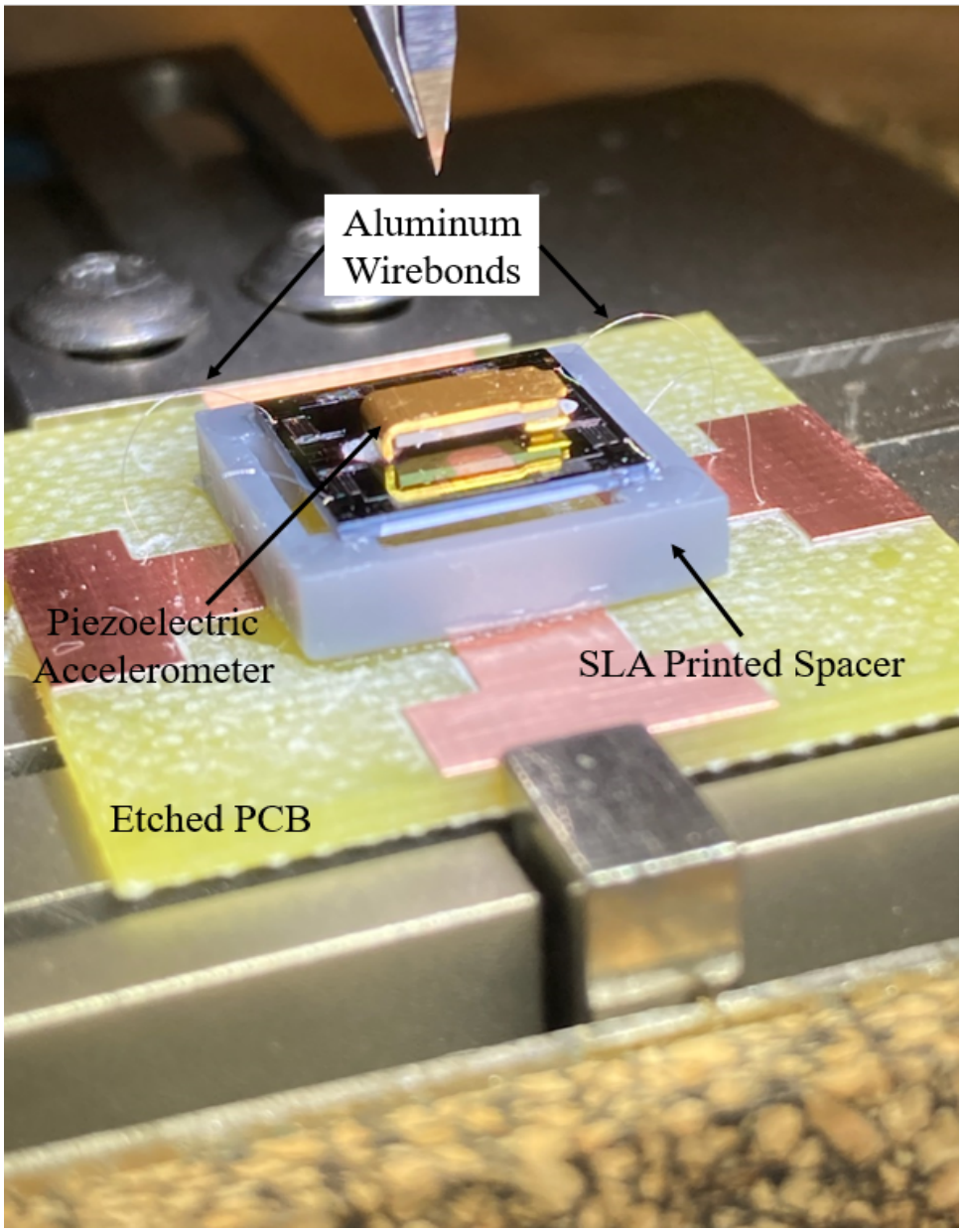

Figure 6.5: Integration setup with piezoelectric accelerometer on I3 MVI. An SLA printed spacer separates the accel/iso combo from the etched PCB to which the isolator output is wirebonded.

Next, the pads on the MVI outer frame are wirebonded to the PCB using 1 mil Al wire. Figure 6.5 shows the complete setup with etched PCB. The two output wires can then be soldered to the PCB output and input into an amplification circuit. A possible output voltage amplification circuit from [129] using an LF356 op-amp is displayed in Figure 6.6.

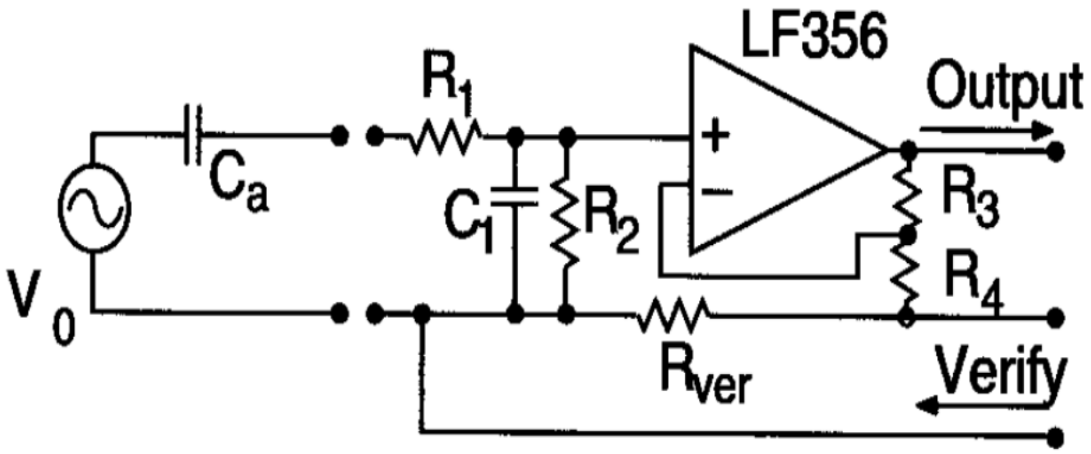

Figure 6.6: Isolator output amplification circuitry.

Voltage V_0 is the piezoelectric voltage generated by the 12M15 accelerometer under harmonic excitation.

6.2 Integrated Piezoelectric Accelerometer Results

To validate the isolation effectiveness of the I3 MVI, RMS voltage output proportional to acceleration from the 12M15 was recorded from 100 Hz to 6000 Hz in 50 Hz steps for both an unisolated accelerometer and an isolated accelerometer. A 1 g acceleration was applied at each frequency step. An integrated circuit piezoelectric (ICP) accelerometer was used as a reference control for monitoring the acceleration magnitude at each frequency step. The MVI/accelerometer combo was damped using Cu MFM.

The acceleration reponses for the reference ICP accelerometer, the unisolated 12M15 piezoelectric accelerometer, and the isolated 12M15 piezoelectric accelerometer are shown in Figure 6.7 (above). Note that at high frequencies the acceleration magnitude of the isolated accelerometer decreases significantly relative to the unisolated accelerometer. This indicates the I3 MVI is effectively filtering high frequency excitation. Also note the presence of resonant peaks throughout the amplification region of the isolated accelerometer. These peaks are expected given the resonant modes exhibited by the MVI.

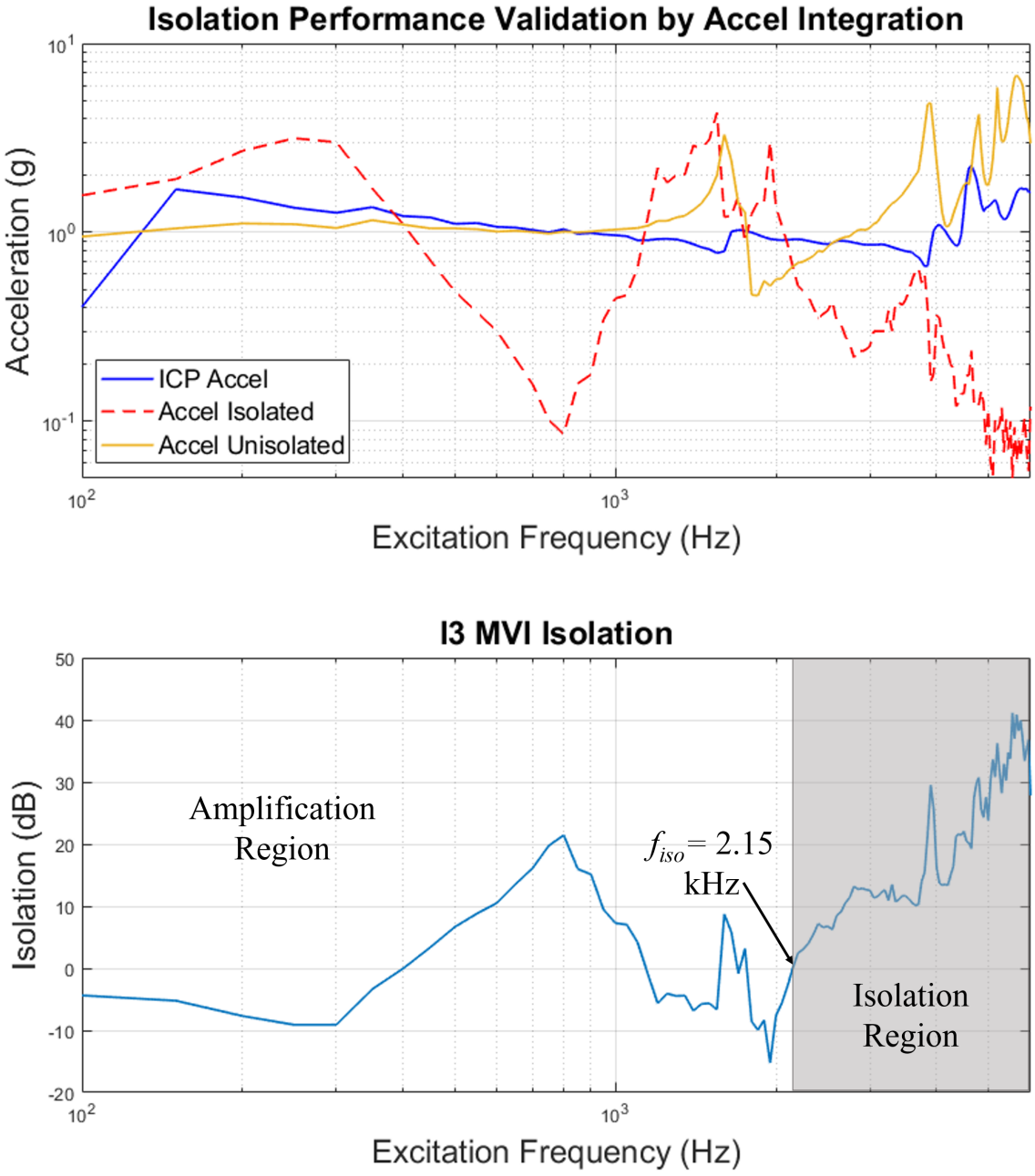

Figure 6.7: Measured accelerations for isolated and unisolated piezoelectric accelerometer with ICP reference accelerometer (above). Accelerometers are excited sinusoidally at 1 G from 100 to 6000 Hz in 50 Hz steps. Below is plotted the isolation provided by the I3 MVI at each frequency step.

Also in Figure 6.7 is a plot of the isolation provided by the I3 MVI (below) as a function of the excitation frequency.

The mechanical isolation provided by the MVI is directly analogous to the insertion loss (IL) provided by an electrical filter. The expression to calculate the isolation provided by the MVI is:

$$Isolation(dB) = 20 * log(\frac{A_0}{A_i}) \tag{6.1}$$

Where A_0 is the acceleration magnitude at a given frequency recorded by the unisolated accelerometer and A_i is the acceleration magnitude at a given frequency recorded by the isolated accelerometer. The I3 MVI exhibits an isolation frequency (point of 0 dB isolation) at 2.15 kHz. Peak recorded isolation is 41.14 dB at 5.55 kHz.

6.3 Future Work

The work presented in this dissertation is by no means an exhaustive treatment of the all of the topics discussed within it. There is still much research to be conducted in the fields of vibration isolation and MEMS sensor reliability and on the topic of micromachined isolators. It is the aim of the author for this dissertation to serve as a guide for future investigations in these and in related fields. In that light, the following subsections are suggested topics which warrant further research.

6.3.1 Reliability

Additional long term vibration reliability studies should be performed. The possible durations of these long term tests could range from a few hours to as much time as the curious researcher is willing to invest in such a study. These studies could be designed to compare the effect of various damping materials on the reliability of the tested MVI/damper combo for various damping techniques and materials and they could also compare the reliability of

different MVI designs. Also, vibration reliability studies for various harmonic acceleration magnitudes should be conducted in order to experimentally determine the possible harsh environment operating conditions for which the MVI is suitable. Acceleration magnitudes resulting in MVI fracture failure could represent an upper limit on the vibration levels in certain environments which might render MVI integration ineffective.

6.3.2 Fabrication

Mentioned in this dissertation are alternative techniques for the fabrication of MVIs beyond Si micromachining (additive manufacturing and TPP). As these technologies mature in coming years, they may provide advantages, in addition to those already listed, to traditional Si micromachined MVIs. Such advantages may make them better suited for certain microscale isolation applications. Thus, continued study of alternative means of MVI fabrication is warranted. For example, additive manufacturing provides much better fabrication control in three dimensions than Si micromachining. For certain isolation applications, this 3D control may be a worthy tradeoff to the wafer-scale batch fabrication possible with traditional micromachining.

6.3.3 Damping

In addition to the damping materials studied in the dissertation, many more materials, such as rubber, foams, oils, etc., are used in damping applications and may be applicable to microscale isolation applications. Future damping research could investigate means of integrating these alternative damping materials and evaluating their damping performance.

Also of interest is the effect of damper geometry on the dynamic response of MVIs. PDMS is a geometry-definable material with which geometry studies can be conducted.

Development of a wafer-scale, batch fabrication-compatible damping solution is also of interest. Thus far all dampers have been adhered/integrated to the MVI after the MVIs have been released from the wafer via the through handle layer etch. A material such as PDMS

allows the damping material to be spun-on to the wafer if wafer-scale damper integration is desired.

6.3.4 Integration

Thus far, only the Cu MFM damped I3 MVI configuration has been validated via the integration of a piezoelectric accelerometer. Future work should characterize the isolation performance of the I3 MVI both undamped and with alternative damping materials via integration of a piezoelectric accelerometer. Also, integration of other MEMS sensors such as gyroscopes should be studied. The acceleration sensitivity attenuation provided by the MVI should be measured and characterized.

Bibliography

[1] Nathanson, H. C., and R. A. Wickstrom. "A resonant-gate silicon surface transistor with high-q band-pass properties. " *Applied Physics Letters* 7.4 (1965): 84-86.

[2] G. Cibuzar, "MEMS," in Fabrication Engineering at the Micro- and Nanoscale, S. Campbell, Ed. New York, NY: Oxford University Press, 2013, p. 595.

[3] K. Petersen, "Silicon as a mechanical material," *Proceedings of the IEEE*, vol. 70, no. 5, pp. 420–457, 1982.

[4] R. Bogue, "Recent developments in MEMS sensors: a review of applications, markets and technologies," *Sensor Review*, vol. 33, no. 4, pp. 300–304, 2013.

[5] "MEMS and Nanotechnology Applications," MNX. [Online]. Available: https://www.mems-exchange.org/MEMS/applications.html. [Accessed: 16-Oct-2020].

[6] E. Veilleux, "Vibration Control of Printed-Circuit Boards in a Dynamic Environment," *IEEE Transactions on Parts, Materials and Packaging*,vol. 6, no. 3, pp. 100–105, 1970

[7] P. Wilke, C. Johnson, P. Grosserode, and D. Sciulli, "Whole-spacecraft vibration isolation for broadband attenuation," 2000 IEEE Aerospace Conference. Proceedings (Cat. No.00TH8484).

[8] Conor D. Johnson, Paul S. Wilke, Kenneth R. Darling, "Multi-axis whole-spacecraft vibration isolation for small launch vehicles," Proc. SPIE 4331, Smart Structures and Materials 2001: Damping and Isolation, (2 July 2001); https://doi.org/10.1117/12.432699

[9] J. Reynolds, D. Catling, R. C. Blue, N. I. Maluf, and T. Kenny, "Packaging a piezoresistive pressure sensor to measure low absolute pressures over a wide sub-zero temperature range," *Sensors and Actuators A: Physical*, vol. 83, no. 1-3, pp. 142–149, 2000.

[10] T. Yang, T. Wang, G. Li, J. Shi, and X. Sun, "Vibration Characteristics of Compression Ignition Engines Fueled with Blended Petro-Diesel and Fischer-Tropsch Diesel Fuel from Coal Fuels," *Energies*, vol. 11, no. 8, p. 2043, Jul. 2018.

[11] A. Fujiwara, K. Matsuo, and H. Yamashita, "Vibration analysis of oil-injected twin-screw compressors using simple simulated waveforms," *Proceedings of the Institution of Mechanical Engineers, Part E: Journal of Process Mechanical Engineering*, vol. 225, no. 2, pp. 105–116, 2011.

[12] E. Peiner, R. Mikuta, T. Iwert, H. Fritsch, P. Hauptmann, K. Fricke, and A. Schlachetzki, "Micromachined resonator for cavitation sensing," *Sensors and Actuators A: Physical*, vol. 76, no. 1-3, pp. 266–272, 1999.

[13] T. G. Brown, "Harsh military environments and microelectromechanical (MEMS) devices," SENSORS, 2003 IEEE, Toronto, Ont., 2003, pp. 753-760 Vol.2.

[14] T. G. Brown et al., "Strap-down microelectromechanical (MEMS) sensors for high-g munition applications,"*IEEE Transactions on Magnetics*, vol. 37, no. 1, pp. 336-342, Jan. 2001.

[15] B. R. Davies, V. I. Bateman, F. A. Brown, S. Montague, J. R. Murray, D.Rey, and J. H. Smith, "Micromachined accelerometer design, modeling and validation," in Proc. Conf. Modeling Simulation Microsyst., SantaClara, CA, April 1998, pp. 552–556.

[16] D. K. Shaeffer, "MEMS inertial sensors: A tutorial overview," *IEEE Communications Magazine*, vol. 51, no. 4, pp. 100–109, 2013.

[17] M. K. Mishra, V. Dubey, P. M. Mishra, and I. Khan, "MEMS Technology: A Review," Journal of Engineering Research and Reports, pp. 1–24, 2019.

[18] G. D. Pasquale and A. Soma, "Reliability Testing Procedure for MEMS IMUs Applied to Vibrating Environments," *Sensors*, vol. 10, no. 1, pp.456–474, 2010.

[19] V. Srikar and S. Senturia, "The reliability of microelectromechanical systems (MEMS) in shock environments," *Journal of Microelectromechanical Systems*, vol. 11, no. 3, pp. 206–214, 2002.

[20] D. G. Mcintyre, S. J. Cunningham, J. S. Carper, P. D. Jaramillo, S. Tatic-Lucic, and L. E. Starr, "Characterization of the influence of fabrication methods on microstructure failure," *Sensors and Actuators A: Physical*, vol. 60, no. 1-3, pp. 181–185, 1997.

[21] A. Beliveau, G. Spencer, K. Thomas, and S. Roberson, "Evaluation of MEMS capacitive accelerometers," IEEE Design and Test of Computers, vol. 16, no. 4, pp. 48–56, 1999.

[22] D. Tanner, J. Walraven, K. Helgesen, L. Irwin, F. Brown, N. Smith, and N. Masters, "MEMS reliability in shock environments," 2000 IEEE International Reliability Physics Symposium Proceedings. 38th Annual (Cat. No.00CH37059).

[23] V. K. Khanna, "Adhesion–Delamination Phenomena at the Surfaces and Interfaces in Microelectronics and MEMS structures and Packaged Devices," *Journal of Physics D: Applied Physics*, vol. 44, no. 3, p. 034004, 2010.

[24] J. Meng, S. T. Douglas, and A. Dasgupta, "MEMS Packaging Reliability in Board-Level Drop Tests Under Severe Shock and Impact Loading Conditions–Part I: Experiment," *IEEE Transactions on Components, Packaging and Manufacturing Technology*, vol. 6, no. 11, pp.1595–1603, 2016.

[25] Y. Huang, A. S. S. Vasan, R. Doraiswami, M. Osterman, and M.Pecht, "MEMS Reliability Review," *IEEE Transactions on Device and Materials Reliability*, vol. 12, no. 2, pp. 482–493, 2012.

[26] K. Komvopoulos, "Surface engineering and microtribology for microelectromechanical systems," *Wear*, vol. 200, no. 1-2, pp. 305–327, 1996.

[27] A. Hartzel and D. Woodilla, "Reliability methodology for prediction of micromachined accelerometer stiction," in Proc. IEEE Int. Rel. Phys. Symp., Mar. 1999, pp. 202–205.

[28] M. P. de Boer, B. D. Jensen, and F. Bitsie,"A small area in-situ MEMS test structure to measure fracture strength by electrostatic probing," in SPIE Proc., vol. 3875, *Materials and Device Characterization in Micromachining*, Santa Clara, CA, Sep. 1999, p. 97.

[29] G. Subhash, A. D. Corwin, and M. P. de Boer,"Operational wear and friction in MEMS devices," in *Proc. 11th ICF*, 2005.

[30] T. Walewyns, G. Scheen, E. Tooten, L. El Fissi, P. Dupuis, and L. A. Francis, "Fabrication of a miniaturized ionization gas sensor with polyimide spacer," *Proc. SPIE* 8066, 80660J (2011).

[31] O. Raccurt et al.,"Influence of liquid surface tension on stiction of SOI MEMS,", *J. Micromech. Microeng.* 14, 1083 (2004).

[32] A. T. DiBenedetto, *The Structure and Properties of Materials*. New York: McGraw-Hill, 1967

[33] D. Tanner, J. Walraven, K. Helgesen, L. Irwin, D. Gregory, J. Stake, and N. Smith, "MEMS reliability in a vibration environment," 2000 IEEE International Reliability Physics Symposium Proceedings. 38th Annual (Cat. No.00CH37059).

[34] U. Beerschwinger, D. Mathieson, R. L. Reuben, and S. J. Yang, "A study of wear on MEMS contact morphologies," *J. Micromech. Microeng.*, vol. 4, no. 3, pp. 95–105, Sep. 1994.

[35] Ritchie R. "Mechanisms of fatigue-crack propagation in ductile and brittle solids." *International Journal of Fracture*, vol. 100, 55–83 (1999).

[36] J. Bagdahn and W. N. Sharpe, "Fatigue of polycrystalline silicon under long-term cyclic loading," *Sensors and Actuators A: Physical*, vol. 103, no. 1-2, pp. 9–15, 2003.

[37] Failure Analysis Associates, Inc. NSF/AFOSR/ASME Workshop, Tribology Issues and Opportunities in MEMS, Nov. 9–11, 1997. Reliability and Fatigue Testing of MEMS Christopher Muhlstein and Stuart Brown.

[38] C. L. Muhlstein, S. B. Brown, and R. O. Ritchie, "High-Cycle Fatigue of Single-Crystal Silicon Thin Films," *J. Microelectromech. Syst.*, vol. 10,no. 4, pp. 593–600, Dec. 2001

[39] A. L. Alter, I. B. Flader, Y. Chen, L. C. Ortiz, D. D. Shin and T. W. Kenny, "Characterization of Accelerated Fatigue in Thick Epi-Polysilicon Vacuum Encapsulated MEMS Resonators," in *Journal of Microelectromechanical Systems*, doi: 10.1109/JMEMS.2020.3021947.

[40] B. Khazaeili, J. Gonzales, and R. Abdolvand, "Acceleration Sensitivity in Bulk-Extensional Mode, Silicon-Based MEMS Oscillators," *Micromachines*, vol. 9, no. 5, p. 233, Dec. 2018.

[41] R. Filler, "The Acceleration Sensitivity of Quartz Crystal Oscillators: A Review," *IEEE Transactions on Ultrasonics, Ferroelectrics and Frequency Control*, vol. 35, no. 3, pp. 297–305, 1988.

[42] J. A. Kosinski and J. A. Gualtieri, "Acceleration sensitivity of surface wave resonators," IEEE Transactions on Ultrasonics, Ferroelectrics and Frequency Control, vol. 44, no. 6, pp. 1343–1347, 1997.

[43] H. F. Tiersten, D. S. Stevens, and R. D. Weglein, "Acceleration sensitivity of surface acoustic wave resonators," *Appl. Phys. Lett.*, vol. 48, pp. 97-99, 1986.

[44] J. Reid, V. Bright, and J. Kosinski, "A micromachined vibration isolation system for reducing the vibration sensitivity of surface transverse wave resonators," IEEE Transactions on Ultrasonics, Ferroelectrics and Frequency Control, vol. 45, no. 2, pp. 528–534, 1998.

[45] J. R. Reid, V. M. Bright, J. T. Stewart and J. A. Kosinski, "Reducing the normal acceleration sensitivity of surface transverse wave resonators using micromachined isolation systems," Proceedings of 1996 IEEE International Frequency Control Symposium, Honolulu, HI, USA, 1996, pp. 464-472.

[46] J. R. Reid, V. M. Bright and J. A. Kosinski, "A micromachined vibration isolation system for a 1 GHz STW resonator," Proceedings of International Frequency Control Symposium, Orlando, FL, USA, 1997, pp. 783-790.

[47] A.M. Shkel, "Type I and Type II Micromachined Vibratory Gyroscopes," Dig. Tech. Papers, IEEE/ION Position Location and Navigation Symposium (PLANS), San Diego, CA, USA (2006), pp. 586-593

[48] S. W. Yoon, S. Lee, and K. Najafi, "Vibration Sensitivity Analysis of MEMS Vibratory Ring Gyroscopes," *Sensors and Actuators A: Physical*, vol. 171, no. 2, pp. 163–177, 2011.

[49] Fang, X., Dong, L., Zhao, W. S., Yan, H., Teh, K. S., and G. Wang, (2018). "Vibration-Induced Errors in MEMS Tuning Fork Gyroscopes with Imbalance." *Sensors* (Basel, Switzerland), 18(6), 1755.

[50] S. W. Yoon, S. Lee, and K. Najafi, "Vibration-Induced Errors in MEMS Tuning Fork Gyroscopes," *Sensors and Actuators A: Physical*, vol. 180, pp. 32–44, 2012.

[51] B. Kim, R. H. Olsson, K. Smart, and K. E. Wojciechowski, "MEMS Resonators with Extremely Low Vibration and Shock Sensitivity," 2011 IEEE SENSORS Proceedings, 2011.

[52] M. Agarwal, K. Park, M. Hopcroft, S. Chandorkar, R. Candler, B.Kim, R. Melamud, G. Yama, B. Murmann, and T. Kenny, "Effects of Mechanical Vibrations and Bias Voltage Noise on Phase Noise of MEMS Resonator Based Oscillators," 19th IEEE International Conference on Micro Electro Mechanical Systems

[53] F.C Nelson "Vibration Isolation: A Review, I. Sinusoidal and Random Excitations," *Shock and Vibration*, 1 (5) (1994), pp. 485-493

[54] A. G. Piersol and T. L. Paez, *Harris' Shock and Vibration Handbook*, 6th ed. New York: McGraw-Hill, 2010.

[55] J. Giaime, P. Saha, D. Shoemaker, and L. Sievers, "A passive vibration isolation stack for LIGO: Design, modeling, and testing," Review of Scientific Instruments, vol. 67, no. 1, pp. 208–214, 1996.

[56] Reid, J.R. (1996). "Microelectromechanical Isolation of Acoustic Wave Resonators," Ph.D. dissertation, AIR FORCE INST OF TECH WRIGHT-PATTERSON AFB OH, Dec 1996. Accessed on: April 27, 2020.

[57] R. Dean, G. Flowers, N. Sanders, R. Horvath, M. Kranz and M. Whitley, "Micromachined Vibration Isolation Filters to Enhance Packaging for Mechanically Harsh Environments," *J. Microelectronics and Electronic Packaging*, Vol. 2, No. 4, 2005, pp. 223-231.

[58] S. W. Yoon, S. Lee, N. C. Perkins, and K. Najafi, "Analysis and Wafer-Level Design of a High-Order Silicon Vibration Isolator for Resonating MEMS Devices," *Journal of Micromechanics and Microengineering*, vol. 21, no. 1, p. 015017, 2010.

[59] K. Xu, N. Zhu, S. Cao, W. Su, W. Zhang and Y. Hao, "Design and simulation of MEMS thermal and vibration isolator based on PDMS beam arrays," 2016 IEEE 11th Annual International Conference on Nano/Micro Engineered and Molecular Systems (NEMS), Sendai, 2016, pp. 213-216, doi: 10.1109/NEMS.2016.7758235.

[60] D. J. Inman, *Engineering Vibration*. Upper Saddle River, New Jersey:Pearson Education, Inc., 2008

[61] E. I. Green, Am. Sci. 43, 584 (1955).

[62] R. Abdolvand, B. Bahreyni, J. Lee, and F. Nabki, "Micromachined Resonators: A Review," *Micromachines*, vol. 7, no. 9, p. 160, 2016.

[63] T. Braman and O. Grossman, "Designing Vibration and Shock Isolation Systems for MicroElectrical Machined Based Inertial Measurement Units," 2006 IEEE/ION Position, Location, And Navigation Symposium

[64] S. Reid, G. Cagnoli, D. Crooks, J. Hough, P. Murray, S. Rowan, M. Fejer, R. Route, and S. Zappe, "Mechanical dissipation in silicon flexures," *Physics Letters A*, vol. 351, no. 4-5, pp. 205–211, 2006.

[65] R. Nawrodt, A. Zimmer, T. Koettig, C. Schwarz, D. Heinert, M. Hudl, R. Neubert, M. Thürk, S. Nietzsche, W. Vodel, P. Seidel, and A. Tünnermann, "High mechanical Q-factor measurements on silicon bulk samples," *Journal of Physics: Conference Series*, vol. 122, p. 012008, Jan. 2008.

[66] A. G. Piersol and T. L. Paez, *Harris' Shock and Vibration Handbook*, 6th ed. New York: McGraw-Hill, 2010.

[67] Nihat Özkaya. *Fundamentals Of Biomechanics: Equilibrium, Motion, and Deformation*. New York, NY: Springer, 2012.

[68] X. Zhou, D. Yu, X. Shao, S. Zhang, and S. Wang, "Research and applications of viscoelastic vibration damping materials: A review," *Composite Structures*, vol. 136, pp. 460–480, 2016.

[69] J. M. Gere and S. P. Timoshenko, *Mechanics of Materials*, Third. Boston, MA: PWS-Kent, 1990.

[70] M. Carfagni and M. Pierini, "Determining the Loss Factor by the Power Input Method (PIM), Part 1: Numerical Investigation," *Journal of Vibration and Acoustics*, vol. 121, no. 3, pp. 417–421, Jan. 1999.

[71] C. Bert, "Material damping," *Journal of Sound and Vibration*, vol. 29, no. 2, pp. 129–153, 1973.

[72] E. Graesser and CR Wong, "The Relationship of Traditional Damping Measures for Materials with High Damping Capacity: A Review," in *M3D: Mechanics and Mechanisms of Material Damping*, edited by Kinra, V. and Wolfenden, A. (West Conshohocken, PA: ASTM International, 10.1520/STP17969S), 343-1992. https://doi.org/978-0-8031-5218-2

[73] B. Bottenfield, A. G. Bond, M. S. Kranz, R. N. Dean and M. L. Adams, "Variations in Micromachined Isolator Geometries for Sensor Performance in Harsh Environments," in *IEEE Transactions on Components, Packaging and Manufacturing Technology*, vol. 10, no. 4, pp. 659-668, April 2020, doi: 10.1109/TCPMT.2019.2947191.

[74] Fedder, G.K. "Simulation of Microelectromechanical Systems", Ph.D. Thesis, Department of Electrical Engineering and Computer Sciences, University of California at Berkeley, 1994. Accessed on: May 21, 2020

[75] M. A. Hopcroft, W. D. Nix, and T. W. Kenny, "What is the Youngs Modulus of Silicon?," *Journal of Microelectromechanical Systems*, vol. 19, no. 2, pp. 229–238, 2010.

[76] M. Elwenspoek and R. J. Wiegerink, *Mechanical Microsensors*. Berlin: Springer, 2011.

[77] C. Nguyen, Class Lecture, Topic: "Lecture 15 - Beam Combos." EE C245 – ME C218 Introduction to MEMS Design, Department of Electrical Engineering and Computer Science, University of California Berkeley, Berkeley, CA 94720, Oct., 2007.

[78] "Pyroshock Test Criteria", NASA-STD-7003A, National Aeronautics and Space Administration, Washington, DC, December 20, 2011.

[79] C. J. Mogab, "The Loading Effect in Plasma Etching," *Journal of The Electrochemical Society*, vol. 124, no. 8, p. 1262, 1977

[80] Karttunen, Jyrki Kiihamaki, Sami Franssila, "Loading effects in deep silicon etching,"Proc. SPIE 4174, Micromachining and Microfabrication Process Technology VI, (25 August 2000)

[81] F. Zhu, X. Zhang, and H. Zhang, "Formation mechanism of multi-functional black silicon based on optimized deep reactive ion etching technique with SF6/C4F8," *Science China Technological Sciences*, vol. 58, no. 2, pp. 381–389, 2015.

[82] H. Jansen, M. D. Boer, R. Legtenberg, and M. Elwenspoek, "The black silicon method: a universal method for determining the parameter setting of a fluorine-based reactive ion etcher in deep silicon trench etching with profile control", *Journal of Micromechanics and Microengineering*, vol. 5, no. 2, pp. 115–120, 1995.

[83] W. M. Huang X. Y. Gao. "Tresca and von Mises Yield Criteria: A View from Strain Space," Philosophical Magazine Letters (2004), 84:10, 625-629, DOI: 10.1080/09500830512331325091

[84] Hull, C.W., Apparatus for production of three-dimensional objects by stereolithography. 1986, Google Patents.

[85] F2792, Standard Terminology for Additive Manufacturing Technologies ASTM International, West Conshohocken, Pa, USA (2012)

[86] Xin Wang, Man Jiang, Zuowan Zhou, Jihua Gou, David Hui, 3D printing of polymer matrix composites: A review and prospective, *Composites Part B: Engineering* ,Volume 110, 2017, Pages 442-458, ISSN 1359-8368.

[87] Bond., A, Zhao, J., Bottenfield, B., Dean, R. N., Adams, M.L., Flowers, G., Perkins, E. (2020) "3D Printed MEMS Scale Vibration Isolators", 2020 International Mechanical Engineering Congress and Exposition, Portland, OR

[88] "Materials Data Sheet: Photopolymer Resin for Form 1+ and Form 2." Formlabs. [Online] Available: https://archive-media.formlabs.com/upload/XL-DataSheet.pdf. [Accessed: 05-Oct-2020].

[89] A. Kamyshny and S. Magdassi, "Conductive nanomaterials for 2D and 3D printed flexible electronics," *Chemical Society Reviews*, vol. 48, no. 6, pp. 1712–1740, 2019.

[90] Shoji Maruo, Osamu Nakamura, and Satoshi Kawata, "Three-dimensional microfabrication with two-photon-absorbed photopolymerization," Opt. Lett. 22, 132-134 (1997).

[91] T. Baldacchini, *Three-dimensional Microfabrication using Two-Photon Polymerization: Fundamentals, Technology and Applications*. Amsterdam: Elsevier, 2016.

[92] Moritz Emons, Kotaro Obata, Thomas Binhammer, Aleksandr Ovsianikov, Boris N. Chichkov, and Uwe Morgner, "Two-photon polymerization technique with sub-50 nm resolution by sub-10 fs laser pulses," Opt. Mater. Express 2, 942-947 (2012)

[93] Kim, DeaGyu, Zhijian Hao, Jun Ueda, and Azadeh Ansari. "A 5 mg micro-bristle-bot fabricated by two-photon lithography." *Journal of Micromechanics and Microengineering* 29, no. 10 (2019): 105006.

[94] Lee, Hyun-Taek, Florent Seichepine, and Guang-Zhong Yang. "Microtentacle Actuators: Microtentacle Actuators Based on Shape Memory Alloy Smart Soft Composite (Adv. Funct. Mater. 34/2020)." *Advanced Functional Materials* 30, no. 34 (2020): 2070231.

[95] Maruo, Shoji, and Koji Ikuta."Submicron stereolithography for the production of freely movable mechanisms by using single-photon polymerization." *Sensors and Actuators A: Physical* 100, no. 1 (2002): 70-76.

[96] Kawata, Satoshi, Hong-Bo Sun, Tomokazu Tanaka, and Kenji Takada. "Finer features for functional microdevices." *Nature* 412, no. 6848 (2001): 697-698.

[97] Maruo, Shoji, and Tatsuya Saeki. "Femtosecond laser direct writing of metallic microstructures by photoreduction of silver nitrate in a polymer matrix." *Optics Express* 16, no. 2 (2008): 1174-1179.

[98] Farsari, Maria, and Boris N. Chichkov. "Two-photon fabrication." *Nature Photonics* 3, no. 8 (2009): 450-452.

[99] Cicha, Klaus, Thomas Koch, Jan Torgersen, Zhiquan Li, Robert Liska, and Jürgen Stampfl. "Young's modulus measurement of two-photon polymerized micro-cantilevers by using nanoindentation equipment." *Journal of Applied Physics* 112, no. 9 (2012): 094906.

[100] S. J. Kim, R. Dean, R. L. Jackson, and G. T. Flowers, "An investigation of the damping effects of various gas environments on a vibratory MEMS device," Tribology International, vol. 44, no. 2, pp. 125–133,2011.

[101] S. J. Kim, R. Dean, G. Flowers, and C. Chen, "Active vibration control and isolation for micromachined devices," Journal of Mechanical Design, vol. 131, no. 9, 2009.

[102] Dean, R., Flowers, G., Horvath, R., Sanders, N., Hodel, S., Hung, J., and Roppel, T., 2007, "Characterization and Experimental Verification of the Non-linear Distortion in a Technique for Measuring Relative Velocity Between Micromachined Structures in Normal Translational Motion," IEEE Sens. J.,7(4), pp. 496–501.

[103] Bottenfield, B., Bond, A., Kranz, M., Dean, R., and Adams, M.L. (2020), Damping Materials for Shock Performance of Micromachined Vibration Isolators, 2020 IMAPS Device Packaging Conference, Fountain Hills, AZ

[104] B. Bottenfield, A. G. Bond, B.A. English, R. N. Dean and M. L. Adams, "Microfibrous Mesh and Polymer Damping of Micromachined Vibration Isolators," in *IEEE Transactions on Components, Packaging and Manufacturing Technology* (Submitted September 2020)

[105] D. K. Harris, D. R. Cahela, and B. J. Tatarchuk, "Wet layup and sintering of metal-containing microfibrous composites for chemical processing opportunities," *Composites Part A: Applied Science and Manufacturing*, vol. 32, no. 8, pp. 1117–1126, 2001.

[106] Tatarchuk BJ, Rose MF, Krishnagopalan A, Zabasajja JN, Kohler D. Mixed fiber composite structures high surface area high conductivity mixtures. US Patent 5,304,330, April 19, 1994.

[107] Tatarchuk BJ. Method of optimizing composite preparation for electrical properties: maximum capacitance electrodes. US Patent 5,102,745, April 7, 1992.

[108] Tatarchuk BJ, Rose MF, Krishnagopalan A, Zabasajja JN, Kohler D. Mixed fiber composite structures. US Patent 5,096,663, March 17, 1992.

[109] Tatarchuk BJ, Rose MF, Krishnagopalan A, Zabasajja JN, Kohler D. Preparation of mixed fiber composite structures. US Patent 5,080,963, January 14, 1992.

[110] P. Soobramaney, G. T. Flowers, and R. N. Dean, "Characterization of damping in microfibrous material," *Sensors and Smart Structures Technologies for Civil, Mechanical, and Aerospace Systems* 2012, 2012.

[111] P. Soobramaney, G. Flowers, and R. Dean, "Mitigation of the Effects of High Levels of High-Frequency Noise on MEMS Gyroscopes Using Microfibrous Cloth," Volume 4: 20th Design for Manufacturing and the Life Cycle Conference; 9th International Conference on Micro- and Nanosystems, Feb. 2015.

[112] M. C. Storm, "Prediction of Sintered Fibrous Metal Liner Influence on Muffler Sound Attenuation Performance and Noise Emission for Single-Cylinder Motorcycle Engine Exhaust," ASME 2008 Noise Control and Acoustics Division Conference, Jan. 2008.

[113] J. Wang, D. Sun, S. Liu, and X. Zhang, "Damping Characteristics of Viscoelastic Damping Structure under Coupled Condition," *Mathematical and Computational Applications*, vol. 22, no. 1, p. 27, 2017.

[114] V. G. Geethamma, R. Asaletha, N. Kalarikkal, and S. Thomas, "Vibration and sound damping in polymers," *Resonance*, vol. 19, no. 9, pp. 821–833, 2014.

[115] Dow,"Sylgard^{TM} 184 Silicone Elastomer," Form No. 11-3184-01 C technical data sheet, 2017.

[116] E. Rubino and T. Ioppolo, "Young's modulus and loss tangent measurement of polydimethylsiloxane using an optical lever," *Journal of Polymer Science Part B: Polymer Physics*, vol. 54, no. 7, pp. 747–751, 2015.

[117] I. D. Johnston, D. K. Mccluskey, C. K. L. Tan, and M. C. Tracey, "Mechanical characterization of bulk Sylgard 184 for microfluidics and microengineering," *Journal of Micromechanics and Microengineering*, vol. 24, no. 3, p. 035017, 2014.

[118] R. W. R. L. Gajasinghe, S. U. Senveli, S. Rawal, A. Williams, A. Zheng, R. H. Datar, R. J. Cote, and O. Tigli, "Experimental study of PDMS bonding to various substrates for monolithic microfluidic applications," *Journal of Micromechanics and Microengineering*, vol. 24, no. 7, p. 075010, 2014.

[119] X. Ye, D. Cai, X. Ruan, and A. Cai, "Research on the selective adhesion characteristics of polydimethylsiloxane layer," *AIP Advances*, vol. 8, no. 9, p. 095004, 2018.

[120] Saentz, C. "Procedures for Bonding PDMS," Microfluidic Facility, Harvard Medical School. Updated: Dec. 16, 2015.

[121] "Dr. Hiles and The Development Of Sorbothane®." [Online]. Available: https://www.sorbothane.com/the-development-of-sorbothane.aspx. [Accessed: 23-Jul-2020].

[122] Bulsara, Y.R. and Matthew, I.R. (1998), "Forces transmitted through a laminated mouthguard material with a Sorbothane insert." *Dental Traumatology*, 14: 45-47. doi:10.1111/j.1600-9657.1998.tb00807.x

[123] Y. Zhang. "Measuring Acoustic Attenuation of Polymer Materials Using Drop Ball Test Ball Test," Master's Thesis, Embry-Riddle Aeronautical University, Daytona Beach, Florida, April 2013. Accessed on: July 24, 2020. [Online]. Available: https://commons.erau.edu/cgi/viewcontent.cgi?article=1150context=edt

[124] "Sorbothane Overview." [Online]. Available: https://www.sorbothane.com/material-properties.aspx. [Accessed: 24-Jul-2020].

[125] J. Houston and C. Gattis, "Passive Isolators for Use on the International Space Station," 42nd AIAA Aerospace Sciences Meeting and Exhibit, 2004.

[126] "Data Sheet 101: Material Properties of Sorbothane®." [Online] Available: https://www.sorbothane.com/Data/Sites/31/pdfs/data-sheets/101-sorbothane-material-properties.pdf. [Accessed: 24-Jul-2020].

[127] Singh, Rajeev Kumar, Rishi Kant, Shashank Shekhar Pandey, Mohammed Asfer, Bishakh Bhattacharya, Pradipta K. Panigrahi, and Shantanu Bhattacharya. "Passive vibration damping using polymer pads with microchannel arrays." *Journal of Microelectromechanical Systems* 22, no. 3 (2013): 695-707.

[128] "Data Sheet: PS12M12 RevF." ENDEVCO.

[129] "Technical Paper 298: ENDEVCO MODEL 12 PICOCHIP™ - Surface Mount Technology Accelerometer." [Online] Available: https://endevco.com/contentStore/mktgContent/endevco/dlmuploads/2019/02/TP298.pdf [Accessed: 01-Nov-2020].

Appendices

Appendix A

Derivation of Peak Transmissibility as Function of Damping

Starting with Equation 3.5 and substituting r for $\frac{\omega}{\omega_n}$:

$$T = \sqrt{\frac{1 + (2\zeta r)^2}{(1 - r^2)^2 + (2\zeta r)^2}} \tag{A.1}$$

Differentiating T with respect to r:

$$\frac{dT}{dr} = -\frac{2r(-1 + r^2 + 2\zeta^2 r^4)}{\sqrt{\frac{1+4r^2\zeta^2}{1+(-2+4\zeta^2)r^2+r^4}}(1 + (-2 + 4\zeta^2)r^2 + r^4)^2} \tag{A.2}$$

Setting $\frac{dT}{dr} = 0$ and solving for r yields the frequency ratio of T_{peak}, r_{peak}. Four non-zero solutions to A.2 exist with only one real, positive solution:

$$r_{peak} = \frac{1}{2}\sqrt{\frac{\sqrt{1 + 8\zeta^2} - 1}{\zeta^2}}, \zeta > 0 \tag{A.3}$$

Substituting r_{peak} for r in A.1 yields the peak transmissibility solely as a function of damping:

$$T(\zeta) = \sqrt{\frac{1 + \zeta^2(\frac{\sqrt{1+8\zeta^2}-1}{\zeta^2})}{\zeta^2(\frac{\sqrt{1+8\zeta^2}-1}{\zeta^2}) + (1 + \frac{1}{4}(\frac{\sqrt{1+8\zeta^2}-1}{\zeta^2}))^2}}, \zeta > 0 \tag{A.4}$$

Further simplification yields Equation 3.13, which holds for high damping, but not very low damping:

$$T_{peak} = \frac{2\sqrt{2}(\zeta^2)}{\sqrt{8\zeta^4 + \sqrt{1 + 8\zeta^2} - 4\zeta^2 - 1}}, \zeta > 0.01 \tag{A.5}$$

Appendix B

Design Flow for Micromachined Vibration Isolator Spring Flexures

1. **Step One** Determine the following filter parameters based upon sensor performance requirements and ambient environmental conditions: f_{iso}, T_{peak}, and stopband attenuation

2. **Step Two** Determine desired or acceptable X,Y footprint of MVI

3. **Step Three** Determine the number of spring flexures required to attenuate additional resonance modes (often rotational) beyond the primary and for trace paths for electrical readout

4. **Step Four** Determine the effective mass: sum of sensor mass and central platform mass required to house the sensor

5. **Step Five** What damping material/technique will be applied to achieve T_{peak}? Calculate the added stiffness due to the damper, k_{damp}.

6. **Step Six** Determine the natural frequency required to achieve f_{iso} using Equation 3.8

7. **Step Seven** Using Step 4 and Step 5 in conjunction with Equation 3.18 calculate the required k_{iso}

8. **Step Eight** Divide Step Seven result by Step Three result to determine the stiffness required for each spring flexure, k_{flex}

9. **Step Nine** Given dimensions of Step 2 and Step 4, is distance enough for required stiffness? If too stiff, add folds to springs to increase length or reduce width/thickness. If too low, consider increasing spring width/thickness, decreasing length

10. **Step Ten** If isolator stiffness is still too high consider addition of a counter mass. Reconsider effective mass in Step Four with added counter mass.

Appendix C

Micromachined Vibration Isolator Fabrication Process

Detailed Microfabrication Process Flow

Updated: June 8, 2020

600 um SOI (100/1.5/500 um) starting wafer

1. **Step One: Wafer Clean**

   (a) 50:1 H2O:HF @ ambient for 30 seconds for oxide removal

   (b) 5:1:1 H_2O:NH_4OH:H_2O_2 at $\approx$ 70 ^oC for 10 min

   (c) DI water rinse, blow dry

2. **Step Two: Thermal Oxidation (Wet - 1 hour), 300-400 nm SiO_2 layer**

   Oxidation Furnace Schedule:

   (a) N_2 at 1050 ^oC, 5 minutes

   (b) O_2 at 1050 ^oC, 5 minutes

   (c) H_2,O_2 at 1050 ^oC, 1 hour

   (d) O_2 at 1050 ^oC, 5 minutes

   (e) N_2 at 1050 ^oC, 5 minutes

3. **Step Three: Device Layer Metallization Lithography**

   (a) Dehydration bake @ 110 ^oC for 10 minutes

   (b) 10 min vapor phase HMDS deposit @ ambient

   (c) PR Spin: AZ 9245 (1700/500/5/2200/1000/25) (apply to both sides)

(d) Softbake PR for solvent removal

i. Handle layer (first) - 10 min in softbake oven at 95 °C

ii. Device layer (second) - 30 min in softbake oven at 95 °C

(e) 35 second UV exposure of photoresist with Karl Suss MABA6 using device layer metallization mask

(f) Develop: Clarient AZ400K, 2:1 (H_2O:Developer) for $\approx$ 45 seconds

(g) DI water rinse, blow dry

4. **Step Four: Device Layer Metallization**

Electron Beam Deposition of Device Layer Metal Stack using CHA-6

(a) 50 nm Titanium adhesion layer deposition

(b) 250 nm Copper conduction layer deposition

(c) 20 nm Gold oxidation prevention layer deposition

(d) Wafer bath in acetone for excess metal liftoff and PR removal (24 - 48 hours)

(e) Acetone, methanol, isopropanol rinse

(f) DI water rinse, dry

5. **Step Five: Handle Layer Metallization Lithography**

(a) Dehydration bake @ 110 °C for 10 minutes

(b) 10 min vapor phase HMDS deposit @ ambient

(c) PR Spin: AZ 9245 (1700/500/5/2200/1000/25) (apply to both sides)

(d) Softbake PR for solvent removal

i. Device layer (first) - 10 min in softbake oven at 95 °C

ii. Handle layer (second) - 30 min in softbake oven at 95 °C

(e) 35 second UV exposure of photoresist with Karl Suss MABA6 using handle layer metallization mask

(f) Develop: Clarient AZ400K, 2:1 (H_2O:Developer) for $\approx$ 45 seconds

(g) DI water rinse, blow dry

6. **Step Six: Handle Layer Metallization**

Electron Beam Deposition of Handle Layer Metal Stack using CHA-6

(a) 50 nm Titanium adhesion layer deposition

(b) 250 nm Copper conduction layer deposition

(c) Wafer bath in acetone for excess metal liftoff and PR removal (24 - 48 hours)

(d) Acetone, methanol, isopropanol rinse

(e) DI water rinse, dry

7. **Step Seven: Device Layer Etch Lithography**

(a) Dehydration bake @ 110 ^oC for 10 minutes

(b) 10 min vapor phase HMDS deposit @ ambient

(c) PR Spin: AZ 9245 (1700/500/5/2200/1000/25) (apply to both sides)

(d) Softbake PR for solvent removal

i. Handle layer (first) - 10 min in softbake oven at 95 ^oC

ii. Device layer (second) - 30 min in softbake oven at 95 ^oC

(e) 35 second UV exposure of photoresist with Karl Suss MABA6 using device layer etch mask

(f) Develop: Clarient AZ400K, 2:1 (H_2O:Developer) for $\approx$ 45 seconds

(g) DI water rinse, blow dry

8. **Step Eight: Device Layer Buffered Oxide Etch**

   (a) Dip wafer in BOE solution for 1 minute

   (b) Inspect oxide using microscope and/or measure using Micropack thin-film analyzer

   (c) Repeat until oxide is fully etched ($\approx$ 4 minutes)

   (d) DI water rinse, dry

9. **Step Nine: Device Layer Deep Reactive Ion Etch**

   (a) STS Si Etcher Parameters:

      i. Etch time - 13 seconds

      ii. Passivation time - 5 seconds

      iii. SF_6 flow rate - 130 sccm

      iv. C_4F_8 flow rate - 85 sccm

      v. RF Power - 600 W

   (b) Perform 20 to 25 cycle etch

   (c) Inspect and/or measure etch depth using profilometer

   (d) Repeat until device layer is fully etched through - buried oxide layer will be visible

10. **Step Ten: Photoresist Removal**

   (a) Rinse in acetone, methanol, and isopropanol

   (b) Rinse in DI water, blow dry

   (c) Dehydration bake at 110 ^{o}C for 15 minutes

11. **Step Eleven: Handle Layer Etch Lithography**

   (a) 10 min vapor phase HMDS deposit @ ambient

(b) PR Spin: AZ 9245 (1700/500/5/2200/1000/25) (apply to both sides)

(c) Softbake PR for solvent removal

i. Device layer (first) - 10 min in softbake oven at 95 °C

ii. Handle layer (second) - 30 min in softbake oven at 95 °C

(d) 35 second UV exposure of photoresist with Karl Suss MABA6 using handle layer etch mask

(e) Develop: Clarient AZ400K, 2:1 (H_2O:Developer) for $\approx$ 45 seconds

(f) DI water rinse, blow dry

12. **Step Twelve: Handle Layer Buffered Oxide Etch**

(a) Dip wafer in BOE solution for 1 minute

(b) Inspect oxide using microscope and/or micropack thin-film analyzer

(c) Repeat until oxide is fully etched

(d) DI water rinse, dry

13. **Step Thirteen: Backing Wafer Attachment**

Steps are performed on a 500 μm thick Si wafer to serve as backing wafer

(a) 10 minute dehydration bake @ 110 °C

(b) 10 minute HMDS deposit @ ambient

(c) PR Spin (one side only, PR should be thicker than PR used for UV exposure): AZ 9245 (ramp to 1000 RPM)

(d) Gently twist device wafer onto backing wafer ensuring there are no gaps between and that the edges of both wafers are aligned smoothly

(e) Softbake: Place wafer in oven for 30 minutes @ 100 °C

14. **Step Fourteen: Handle Layer Deep Reactive Ion Etch**

    (a) STS Si Etcher Parameters:

        i. Etch time - 13 seconds

        ii. Passivation time - 5 seconds

        iii. SF_6 flow rate - 130 sccm

        iv. C_4F_8 flow rate - 85 sccm

        v. RF Power - 600 W

    (b) Perform 50 cycle etch

    (c) Inspect using microscope and measure etch depth using optical profilometer

    (d) Repeat until handle layer is fully etched through - device layer spring flexures will be visible

15. **Step Fifteen: Device Release and Post-Release Clean**

    (a) Place device wafer and backing wafer combo in acetone for release (24 to 48 hours)

    (b) Extract released devices and rinse gently in DI water, allow air dry

    (c) O_2 plasma clean devices at 500 W RF power for 5 minutes to remove residual, hard-baked photoresist

    (d) Inspect device structures and separate structurally sound devices from compromised devices for testing

Appendix D

Microfibrous Mesh Solder Attachment Procedure

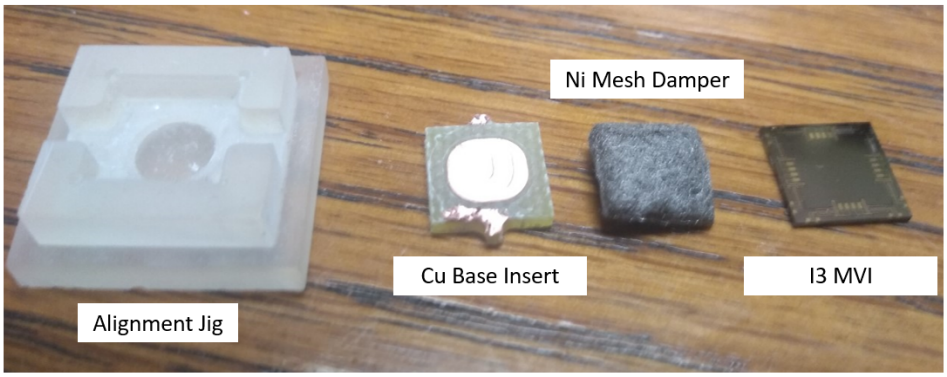

Figure D.1: Components for MFM solder attachment to MVI handle layer

1. **Step One**: Adhere mesh to Cu base insert

   (a) Apply 30-40 mg solder paste to Cu base insert

   (b) Press mesh gently onto Cu base insert. Use 3D-printed alignment jig to align mesh and Cu insert.

   (c) Reflow w/ following recipe (Recipe A):

      i. 2 min ramp to 150 °C

      ii. Hold 1 min @ 150 °C

      iii. 1 min ramp to 250 °C

      iv. Hold @ 250 °C for 30 seconds

      v. Allow cooling to room temperature

2. **Step Two**: Adhere MVI to mesh

(a) Apply 30-40 mg solder paste to the mesh

(b) Press isolator gently onto mesh. Use 3D-printed alignment jig to align mesh and isolator.

(c) Reflow w/ Recipe A

Appendix E

PDMS Damper Preparation Procedure

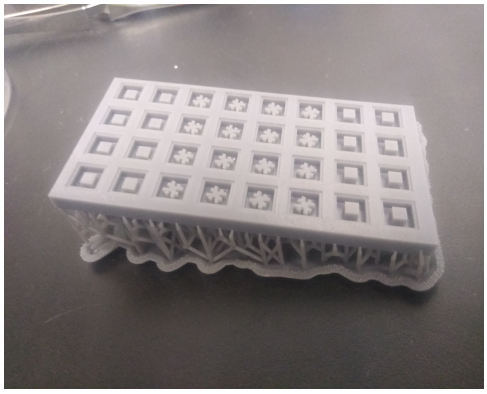

Figure E.1: SLA 3D printed mold for PDMS damper geometry definition

1. **Step One** Print PDMS mold using Formlabs Form3 SLA printer

2. **Step Two** Coat mold with Fine-L-Kote^{TM} AR acrylic conformal coating. Allow 24 hours for curing. This step prevents PDMS from sticking to the mold during PDMS cure.

3. **Step Three** Measure out 10 grams of PDMS polymer and 1 gram of catalyst. Mix vigorously for approximately 10 minutes until mixture is milky-white with bubbles.

4. **Step Four** Place PDMS mixture into dessicator and reduce pressure. Keep mixture at low pressure until bubbles have been removed (typically 30 minutes to an hour).

5. **Step Five** Using a disposal syringe with Luer tip (preferrably metal), inject the PDMS mixture into the printed mold.

6. **Step Six** Place mold into desiccator and reduce pressure to remove bubbles reintroduced into PDMS

7. **Step Seven** Place mold into curing oven. Cure at 40 °C for 24 hours. The reduced temperature prevents any warping of the mold.

Appendix F

PDMS to MVI Adhesion Procedure

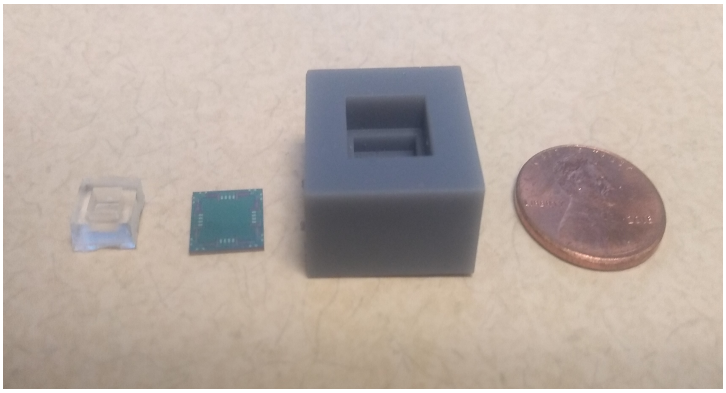

Figure F.1: 3D-printed alignment jig used for PDMS to MVI adhesion

1. **Step One** The handle layer of the MVI and the face of the PDMS damper that will contact the MVI are O_2 plasma treated using (get the name of equipment) with the following parameters:

   (a) Time: 12 seconds

   (b) Pressure: 0.1 to 0.35 Torr

   (c) RF Power: $\approx$ 100 Watts

2. **Step Two** After plasma treatment the damper is placed into the alignment jig so that it sits snugly in the bottom level of the jig. The MVI is then placed into the jig such that it sits evenly on top of the damper.

3. **Step Three** Flip the alignment jig over onto a Si wafer and gently push out the damper/MVI combination. When free of the alignment jig, gently tamp down the

damper onto the MVI. At this point bonding should be apparent as the damper and MVI should be firmly adhered to one another.

4. **Step Four** Place the combo into a curing oven and cure at 60 °C for 20 minutes. This step helps to promote further bonding of the surfaces.